

Host Galaxy Properties of Gamma-ray Bursts Involving Neutron Star Binary Mergers and Its Impact on Kilonovae Rates

MANKEUN JEONG¹ AND MYUNGSHIN IM¹

¹*SNU Astronomy Research Center, Astronomy Program, Department of Physics and Astronomy,
Seoul National University, Gwanak-gu, Seoul 151-742, Korea*

ABSTRACT

In the upcoming gravitational wave (GW) observing runs, identifying host galaxies is crucial as it provides essential redshift information and enables the use of GW events as standard sirens. However, pinpointing host galaxies remains challenging due to the large localization uncertainties and the rapidly fading nature of their optical counterparts. Analyzing the host galaxies of short gamma-ray bursts (sGRBs) offers an alternative approach to deepen our understanding of the environments where binary neutron stars (BNS) primarily merge. This study compiles archival photometric data for the host galaxies of 76 sGRBs and 4 hybrid GRBs that are long GRBs accompanied by kilonova-like signals. We use this data to evaluate their physical properties through spectral energy distribution (SED) fitting. To assess the characteristics of the host galaxies, we utilized a volume-limited sample ($z < 0.5$) from the COSMOS field as a control group. Contrary to expectations that the BNS merger rate is proportional to host stellar mass, the short and hybrid GRB population appears less massive than the mass-weighted distribution of the control sample. Instead, we propose a formulation for the expected BNS merger rate from a galaxy as $\log(n_{\text{BNS}}/\text{Gyr}) = 0.86 \times \log(M_*/M_\odot) + 0.44 \times \log(\text{sSFR}/\text{yr}) + 0.857$, which optimally explains the deviation between the stellar mass distributions of the GRB host galaxies and the control sample. These insights provide a strategic framework for targeted GW follow-ups and enhance our ability to identify potential host galaxies for future GW events.

Keywords: gamma-ray burst: general, transients: neutron star mergers

1. INTRODUCTION

During the first three gravitational wave (GW) observing runs, and now into the fourth, the Advanced Laser Interferometer Gravitational-Wave Observatory (aLIGO; [LIGO Scientific Collaboration et al. 2015](#)), the Advanced Virgo (aVirgo; [Acernese et al. 2015](#)), and the Kamioka Gravitational Wave Detector (KAGRA; [Akutsu et al. 2021](#)) collaborations have successfully measured the masses and distances of compact binary objects ([Abbott et al. 2016, 2017a, 2021b](#)). In particular, the first binary neutron star (BNS) merger event, GW170817, confirmed the simultaneous emission of both GW and electromagnetic (EM) signals, evidenced by an accompanying kilonova and a short gamma-ray burst (sGRB) (e.g., [Abbott et al. 2017b](#);

[Troja et al. 2017](#); [Chornock et al. 2017](#); [Evans et al. 2017](#); [Pian et al. 2017](#); [Smartt et al. 2017](#)). Such multi-messenger astronomy (MMA) events allow for the identification of the host galaxy ([Blanchard et al. 2017](#); [Hjorth et al. 2017](#); [Levan et al. 2017](#); [Im et al. 2017](#); [Pan et al. 2017](#); [Fong et al. 2017](#)), from which we can measure the redshift and utilize the GW event as standard sirens ([Abbott et al. 2017c](#); [Kasen et al. 2017](#); [Abbott et al. 2021a](#); [Palmese et al. 2021](#)). Therefore, in upcoming GW observing runs, the discovery of optical counterparts and host galaxies for GW events will be as crucial as ever.

Identifying the host galaxy and EM counterpart of GW can be challenging due to the substantial localization uncertainty and rapidly fading nature of kilonova (e.g., [Arcavi et al. 2017](#); [Kasen & Barnes 2019](#); [Abbott et al. 2020a](#)). A notable example is GW190425, a probable BNS merger detected during the LIGO/Virgo O3 run. This event had an exceptionally large 90% credible localization area, spanning 7461 square degrees ([Abbott](#)

Corresponding author: Myungshin Im
myungshin.im@gmail.com

et al. 2020b). Despite extensive efforts, no EM counterpart has been identified (Coughlin et al. 2019, 2020; Paek et al. 2024).

In the ongoing GW O4 observing run, it has been anticipated that improvements in detector sensitivity would reduce the localization uncertainty of BNS merger events to tens of square degrees (Abbott et al. 2020a). However, due to delays in integrating Advanced Virgo into the GW network, the expected enhancements in performance have not been realized. Consequently, the localization uncertainty for BNS merger events has escalated to thousands of square degrees, as predicted under less optimal operational scenarios (Singer et al. 2014; Berry et al. 2015).

These challenges underscore the essential role of understanding host galaxy environments for prioritizing and planning effective GW follow-up observations (Singer et al. 2016; Coulter et al. 2017; Dálya et al. 2018, 2021). GW alert brokers will streamline GW follow-up efforts by optimizing observation strategies, including tiling or targeting observations, to efficiently cover localized areas (Song et al. 2022; Liu et al. 2023). In this context, integrating galaxy-oriented observations from ground-based telescopes into these strategies can enhance the ability to formulate effective approaches, underlining a thorough understanding of the host galaxy environment (Rinaldi & Del Pozzo 2022; Singer et al. 2022).

Simulation studies utilizing binary evolutionary models and galactic hydrodynamics have suggested that stellar mass should be a crucial predictor of GW event rates in local galaxies (Mapelli et al. 2018, 2019; Artale et al. 2020; Chu et al. 2022). This insight is based on the premise that, over the extended delay time during which a binary system merges, the host galaxy itself undergoes evolution from galaxy mergers. This concept has been incorporated into resources like the Extended Galaxy List for the Advanced Detector Era (GLADE+), which serves as a reference catalog for identifying host galaxies (Dálya et al. 2021).

The host galaxies of sGRBs are useful to validate predictions about the BNS merger environment, as they are one of the MMA signals generated by the collision of either BNS or neutron star-black hole (NSBH) binaries (Ruffert & Janka 1999; Rosswog et al. 2003; Faber et al. 2006; Shibata & Taniguchi 2011). Earlier analyses of sGRB host galaxies revealed a mixed population of early-type and star-forming galaxies, which were reported to predominantly follow an older stellar population compared to long GRB host galaxies (Leibler & Berger 2010; Berger 2014).

Recent deep optical/NIR survey observations have revealed additional faint and high redshift host galaxies, prompting a reevaluation of the sGRB host population (O’Connor et al. 2022a; Fong et al. 2022). Following this, a comprehensive statistical analysis of 67 sGRB host galaxies by Nugent et al. (2022) demonstrated that their mass, metallicity, and star formation rate (SFR) are consistent with the star-forming main sequence. Intriguingly, high redshift sGRBs indicate a steeper delay-time distribution (DTD) than previously anticipated by binary evolution models (Zevin et al. 2022). This evidence challenges established theoretical perspectives on BNS mergers, identifying the host galaxy NGC 4993 of the BNS merger as an atypical example.

In response to the discrepancies between sGRB host statistics and simulation predictions, our study aims to quantitatively evaluate the global properties of local sGRB host galaxies. Additionally, to address uncertainties surrounding sGRB classifications, we will examine cases where kilonova-like signals were detected alongside GRBs with long prompt emissions or extended emission features. These hybrid GRBs are believed to originate from compact binary mergers involving neutron stars (Troja et al. 2022; Yang et al. 2024). We will analyze the stellar mass and SFR distributions of these host galaxies using spectral energy distribution (SED) fitting. This analysis will enable us to assess how these distributions deviate from those of typical galaxies in the local universe. The extent of these deviations may be indicative of the contribution of BNS mergers to the overall merger rate. The BNS merger rate derived from this analysis will help prioritize galaxies within probable volumes for future GW events and assist in assessing their redshift probability distributions.

The structure of this paper is as follows. In Sections 2 and 3, the processes of collecting sGRB samples and photometry data are presented. Section 4 describes the SED fitting procedure and the control sample definition. And, Section 5 presents the distributions of sGRB host galaxies properties and derivation of the BNS merger rate expectation. In Section 6, we will discuss the meaning of the BNS merger rate, potential sample biases and some limitations in our study. Finally, in Section 7, a summary and conclusion are presented. Throughout the paper, magnitudes are in ABmag with the extinction correction of Schlafly & Finkbeiner (2011), and all the errors correspond to 1σ . The cosmological parameters are adopted as $H_0 = 70 \text{ km s}^{-1} \text{ Mpc}^{-1}$, $\Omega_\Lambda = 0.73$, and $\Omega_M = 0.27$.

2. SAMPLE

2.1. sGRB Host Galaxy Sample

To compile a comprehensive dataset of sGRB host galaxies, we combined target lists from various sources. The majority of the host galaxies are associated with sGRBs detected by the *Swift* Burst Alert Telescope (BAT; Barthelmy et al. 2005), in conjunction with the X-ray Telescope (XRT) and Ultra-violet Telescope (UVOT) (Roming et al. 2005; Burrows et al. 2005). This is primarily due to the fact that while the localization region for a GRB itself is rather uncertain for precisely identifying the host galaxy, the positional uncertainties are significantly reduced to subarcsecond or a few arcseconds when an optical or X-ray counterpart is discovered by *Swift*.

Due to the absence of definitive redshift data, the identification of a host galaxy requires deep observations and careful investigation of field galaxies around the burst location (Bloom et al. 2002; Berger 2010; Tunnicliffe et al. 2014). Recent host population studies, like O’Connor et al. (2022a) and Fong et al. (2022), have conducted imaging observations reaching a deep limit (down to $r \gtrsim 26$ ABmag). Such efforts have enhanced the completeness of the host galaxy dataset, setting a robust background for subsequent statistical analyses.

The Broadband Repository for Investigating Gamma-ray burst Host Traits (BRIGHT¹) serves as an archive for the photometric data of most sGRB host galaxies identified between 2005 and 2021 (Fong et al. 2022). Among the host galaxies cataloged there, 69 are conclusively associated with sGRBs and possess sufficient photometric data to conduct SED analysis (Nugent et al. 2022).

To enlarge the sGRB host galaxy sample, we examined recent Gamma-ray Coordinates Network (GCN) reports. Notably, there are dedicated web-based repositories, such as GRBweb² and GRBOX³. These sites archive observational logs and discussions about post-burst detection, primarily from instruments like the *Swift* BAT and the *Fermi* Gamma-ray Burst Monitor (GBM; Meegan et al. 2009). By evaluating the burst duration and its association with potential host galaxies, we identified additional host candidates.

With the help of published papers or reports dealing with an individual sGRB and its host galaxy, dozens of host galaxies were added. These cases are GRB 050906, GRB 070810B, GRB 080121, GRB 100216A (Dichiara et al. 2020), GRB 060502B (Bloom et al. 2007), GRB 060505 (Ofek et al. 2007), GRB 100816A (Tanvir et al.

2010), GRB 110402A, GRB 120630A, GRB 160525B (O’Connor et al. 2022a), GRB 210510A (Anand et al. 2021), GRB211227A (Lü et al. 2022), GRB 221120A (O’Connor et al. 2022b). Consequently, our dataset includes 80 short and hybrid GRB host galaxies whose r -band magnitude distribution according to their redshift is presented in Figure 1.

2.2. Ambiguous or Excluded sGRB Host Samples

Measuring the redshift directly from the faint afterglow of sGRBs is challenging, leading to inherent ambiguities in the identification of their host galaxies. Therefore, if there is no galaxy clearly overlapping in the burst region, we cannot definitively determine whether the host galaxy of such sGRB is a local bright galaxy with a large offset or an undetected faint galaxy at a high redshift.

There are cases where no prominent galaxy can be identified despite the burst locations being accurately determined from optical afterglows. It is worth noting that up to 20% of sGRBs might occur away from host galaxies with progenitors possibly attaining high velocities of 50-200 km/h due to supernova kicks (Bloom et al. 1999; Belczynski et al. 2006). Thus, in cases where no neighboring galaxy is detected in the vicinity (often referred to as “hostless”), discerning between a high redshift origin and a lower redshift host with significant physical offset becomes particularly complicated (Berger 2010; Tunnicliffe et al. 2014).

While recent deep and systematic observations have resolved some of these ambiguities, some samples ($\sim 13\%$ of the total samples) remains ambiguous in host identification with the probability of chance coincidence (P_{CC}) over 10%: GRB 050813, GRB 050906, GRB 080121, GRB 080123, GRB 100816A, GRB 110402A, GRB 140622A, GRB 160408A, GRB 200411A, GRB 201221D and GRB 210919A. Note that this probability is obtained from the comparison between the offset with the host and the average number density of galaxies (Bloom et al. 2002). These samples could pose a risk of bias, but reports indicate that including such GRB host galaxies does not significantly alter statistical properties (Nugent et al. 2022). These samples are still included in our study, and the effects of this will be discussed later.

More such ambiguities arise for events such as GRB 050906, GRB 070810B, GRB 080121, and GRB 100216A, where no afterglow detection exists. While host galaxies are typically not designated without afterglow detection, the γ -ray error circles for these events overlap with bright galaxies at < 200 Mpc (Dichiara et al. 2020). Such rare coincidences with local bright galaxy fields elevate their significance as host galaxy

¹ <https://bright.ciera.northwestern.edu/>

² <https://sites.astro.caltech.edu/grbox/grbox.php>

³ <https://user-web.iccube.wisc.edu>

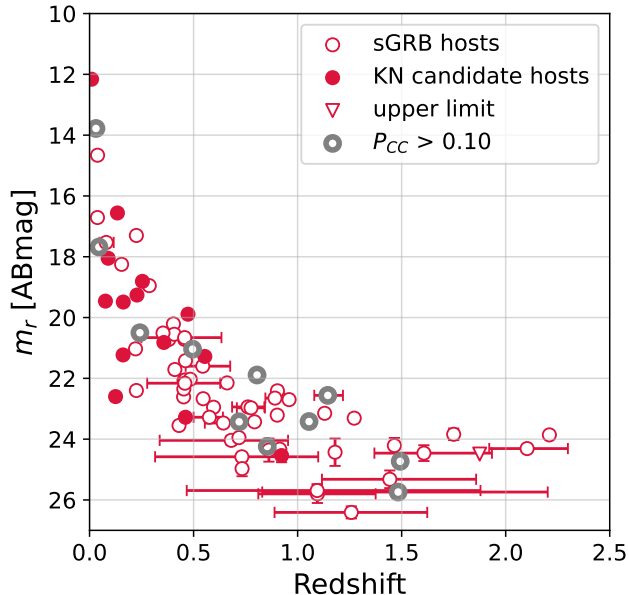


Figure 1. The r -band apparent magnitudes versus redshift for the 80 short and hybrid GRB host galaxies listed in Table 1. The 14 filled circles represent samples with probable kilonova detection in the light curve, while the other empty circles refer to normal short or hybrid GRB host galaxies. 11 Points overlapping with the thick gray circles are samples with a probability of chance coincidence (P_{CC}) measured to be greater than 0.1. The sample marked as an upper limit corresponds to GRB 151229A, whose host galaxy has been measured to have an i -band magnitude of 24.924 ± 0.134 with P_{CC} of 0.04 (Fong et al. 2022).

candidates, though physical associations remain undetermined. In instances of gravitational wave detection, these kinds of galaxies would serve as primary observing targets. We will assess the variance in the GRB host galaxy characteristics with the inclusion or exclusion of these samples to evaluate such prioritization.

Due to insufficient photometric data for the SED modeling, we excluded 5 sGRBs from our sample set: GRB 051210A, GRB 061217, GRB 080905A, GRB 180727A and GRB200907B. We note that our SED modeling necessitates a minimum of five broad-band photometric data points to ensure a robust analysis. Specifically, for GRB 080905A, photometry was compromised by the proximity to bright stars (Fong et al. 2013; Guelbenzu et al. 2021). These exclusions also can impose a bias on our sample. However, since most are presumed to be at high redshifts, this has a negligible impact on our objective of analyzing the characteristics of nearby GW host galaxies.

2.3. Afterglow Emission Features and Kilonovae Candidates

GRBs are classified based on the duration of the prompt emission, i.e., those shorter than 2 seconds are termed sGRBs, while those longer are called long GRBs (Kouveliotou et al. 1993). The criterion of T_{90} less than 2 seconds has been believed to select compact binary coalescence (CBC) among GRBs (Narayan et al. 1992). However, recent studies revealed that collapsars and CBCs significantly overlap in their T_{90} distributions (Bromberg et al. 2013; Jespersen et al. 2020). Given this background, defining a sample based solely on prompt emission might leave contaminants. Therefore, in ambiguous cases, there is a need to investigate the features of the light curve both in prompt and afterglow emissions for further classification.

Among the reported cases, we excluded instances whose T_{90} was shorter than 2 seconds but discovered alongside a supernova, leading to suspicions of being collapsars. GRB 090426 and GRB 200826A are examples of this, and their afterglow brightnesses were consistent with that of typical LGRBs (Antonelli et al. 2009; Rossi et al. 2022). Due to their short delay times, the host galaxies of such collapsars are skewed towards younger stellar age and lower metallicity than regular sGRB host galaxies (Berger 2014).

Conversely, certain cases warrant classification as CBCs despite having T_{90} duration exceeding 2 seconds. This group notably includes instances of extended emissions (EE), which is characterized by a short, initial peak similar to typical short GRBs, followed by a prolonged tail (Norris & Bonnell 2006). Although the exact physical origin of EE remains uncertain, evidence suggests that their environments, such as offsets and host galaxy luminosities, appear similar to those of regular sGRBs (Fong et al. 2022). Moreover, the T_{90} duration itself is not conclusive as it is subject to instrumental selection effects (Dichiara et al. 2021). Consequently, sGRBs exhibiting EE characteristics were included in our sample, regardless of their extended T_{90} duration. The sGRB samples reported to have EE features are indicated in Table 1.

Another important aspect is the observation of kilonova (KN) emission features in GRB afterglows. An excess in infrared brightness days after the burst, consistent with the radioactive decay of r-process elements, suggests a significant release of r-process heavy elements. This is indicative of a CBC involving a neutron star. Ascenzi et al. (2019) identified nine KN candidates through afterglow light curve fitting of historical sGRBs. Gao et al. (2017) classified GRB 050724, GRB 061006, and GRB 070714B as KN candidates based on a magnetar-powered merger-nova model. Additionally, Rossi et al. (2020) observed signs of shallow decay in the afterglows

of six sGRBs (GRB 050709, GRB 050724, GRB 060614, GRB 090515, GRB 150424A, and GRB 160821B) when compared to the light curve of AT2017gfo. Such shallow decays challenge the traditional fireball model, pointing instead towards the presence of an additional emitting source, possibly a kilonova.

Additionally, unique cases have been identified where kilonovae follow typical long GRBs with $T_{90} > 2\text{sec}$. These events are often referred to as “hybrid GRBs.” Notable examples include GRB 060614 (Yang et al. 2015), as well as more recent analyses of GRB 060505

(Jin et al. 2021), GRB 211211A (Rastinejad et al. 2022; Yang et al. 2022), GRB 211227A (Zhu et al. 2022; Lü et al. 2022), and GRB 230307A (Gottlieb et al. 2023; Yang et al. 2024). The origins of these hybrid GRBs are subject to various interpretations, with some suggesting they might originate from BNS mergers, NSBH mergers, or neutron star-white dwarf mergers (Kang et al. 2023). In our study, we include a total of 11 KN candidates and 4 hybrid ones. By analyzing the distribution of KN host galaxies in relation to sGRB host galaxies, we aim to refine our understanding of the environments associated with neutron star mergers.

Table 1. List of the Short and Hybrid GRB Host Galaxies.

GRB	redshift	T_{90} [sec]	AG detection ^a	LC Feature ^b	m_r [ABmag]	Offset [arcsec]	P_{CC}
GRB050509B	0.225	0.024	X-ray	-	17.30±0.07	15.10	5.00E-03
GRB050709	0.161	0.070	Optical	KN ^{1,2}	21.23±0.07	1.35	3.00E-03
GRB050724	0.254	98.0	Optical	KN ^{1,2,3} , EE	18.81±0.05	0.68	2.00E-05
GRB050813	0.719	0.380	X-ray	-	23.43±0.07	5.96	0.2
GRB050906	0.0308	0.128	None	-	13.78±0.03	162.63	0.144
GRB051210	0.681 ^{+0.27} _{-0.34}	1.30	X-ray	-	24.04±0.15	3.56	0.04
GRB051221A	0.546	1.40	Optical	-	22.67±0.09	0.32	5.00E-05
GRB060502B	0.287	0.131	X-ray	-	18.95±0.04	15.91	0.076
GRB060505	0.0894	4.00	Optical	KN ⁴ , EE	18.05±0.04	3.60	2.03E-03
GRB060614	0.125	109	Optical	KN ^{1,2,5} , EE	22.60±0.05	0.31	3.00E-04
GRB060801	1.13	0.490	Optical	-	23.15±0.11	1.23	0.02
GRB061006	0.461	130	Optical	KN ³ , EE	23.28±0.09	0.24	4.00E-04
GRB061210	0.41	85.3	X-ray	EE	21.71±0.13	2.82	0.02
GRB070429B	0.902	0.470	Optical	-	23.21±0.04	0.76	3.00E-03
GRB070714B	0.923	64.0	Optical	KN ³ , EE	24.54±0.22	1.55	5.00E-03
GRB070724	0.457	0.400	Optical	-	20.72±0.05	0.94	8.00E-04
GRB070729	0.761 ^{+0.08} _{-0.08}	0.900	X-ray	-	22.94±0.09	3.13	0.036
GRB070809	0.473	1.30	Optical	KN ⁶	19.89±0.02	5.70	6.00E-03
GRB070810B	0.0385	0.072	None	-	14.66±0.01	81.04	0.073
GRB071227	0.381	143	Optical	EE	20.72±0.03	2.80	0.01
GRB080121	0.045	0.320	None	-	17.68±0.05	66.96	0.41
GRB080123	0.495	115	X-ray	EE	21.04±0.04	8.74	0.11
GRB090510	0.903	5.66	Optical	EE	22.41±0.14	1.33	8.00E-03
GRB090515	0.403	0.036	X-ray	EE	20.21±0.05	13.98	0.05
GRB100117	0.914	0.300	Optical	EE	24.33±0.10	0.17	7.00E-05
GRB100206A	0.407	0.120	X-ray	-	20.55±0.09	4.59	0.02
GRB100216A	0.038	0.208	None	-	16.71±0.07	34.66	0.065
GRB100625A	0.452	0.330	X-ray	-	22.61±0.05	0.45	0.04
GRB100816A	0.805	2.05	Optical	-	21.89±0.06	6.39	0.115
GRB101219A	0.718	0.830	X-ray	-	23.95±0.05	0.75	0.06
GRB101224A	0.454	0.200	X-ray	-	22.07±0.05	2.18	0.015
GRB110402A	0.854	56.0	Optical	EE	24.24±0.20	3.39	0.19

Continued on next page

Table 1 – continued from previous page

GRB	redshift	T_{90} [sec]	AG detection ^a	LC Feature ^b	m_r [ABmag]	Offset [arcsec]	P_{CC}
GRB111117A	2.21	0.470	X-ray	-	23.86±0.08	1.25	0.024
GRB120305A	0.225	0.100	X-ray	-	22.40±0.05	4.97	0.053
GRB120630A	0.544 ^{+0.13} _{-0.08}	0.600	Optical	-	21.60±0.06	3.39	0.027
GRB120804A	1.258 ^{+0.36} _{-0.37}	0.810	Optical	-	26.41±0.20	0.27	0.02
GRB121226A	2.103 ^{+0.20} _{-0.18}	1.00	X-ray	-	24.31±0.06	0.27	0.019
GRB130515A	0.891 ^{+0.05} _{-0.05}	0.290	X-ray	-	22.65±0.04	8.05	0.081
GRB130603B	0.357	0.180	Optical	KN ^{1,7}	20.82±0.01	1.07	2.00E-03
GRB130822A	0.154	0.040	X-ray	-	18.25±0.06	22.32	0.086
GRB140129B	0.43	1.36	Optical	-	23.55±0.07	0.31	8.70E-04
GRB140622A	0.959	0.130	X-ray	-	22.70±0.04	4.10	0.1
GRB140903A	0.353	0.300	Optical	-	20.51±0.09	0.18	6.20E-05
GRB140930B	1.465	0.840	Optical	-	24.21±0.25	1.12	0.021
GRB141212A	0.596	0.300	X-ray	-	22.95±0.06	2.78	2.90E-04
GRB150101B	0.134	0.018	Optical	KN ^{1,8}	16.56±0.04	3.07	4.80E-04
GRB150120A	0.46	1.20	X-ray	EE	22.05±0.06	0.81	1.90E-03
GRB150728A	0.461	0.830	X-ray	-	21.42±0.05	1.28	0.018
GRB150831A	1.18	0.920	X-ray	-	24.43±0.45	1.48	0.037
GRB151229A	1.879 ^{+0.80} _{-0.80}	1.44	X-ray	-	≥24.49	1.18	0.04
GRB160303A	1.095 ^{+0.28} _{-0.28}	5.00	Optical	-	25.80±0.30	1.88	0.096
GRB160408A	1.483 ^{+0.72} _{-0.65}	0.320	Optical	-	25.74±0.16	1.65	0.14
GRB160411A	0.732 ^{+0.37} _{-0.42}	0.360	X-ray	-	24.58±0.13	0.18	7.20E-04
GRB160525B	0.576 ^{+0.07} _{-0.08}	0.290	X-ray	-	23.28±0.09	0.79	1.00E-03
GRB160624A	0.484	0.200	X-ray	EE	22.03±0.02	1.59	0.037
GRB160821B	0.162	0.480	Optical	KN ^{1,2,9} , EE	19.49±0.07	5.61	0.044
GRB161001A	0.776 ^{+0.07} _{-0.07}	2.60	X-ray	-	22.97±0.05	2.61	0.045
GRB161104A	0.793	0.100	X-ray	-	23.43±0.10	0.22	0.06
GRB170127B	1.443 ^{+0.42} _{-0.33}	0.510	X-ray	-	25.32±0.29	1.24	0.098
GRB170428A	0.453	0.200	Optical	-	22.35±0.10	1.32	6.70E-03
GRB170728A	1.493	1.25	X-ray	-	24.73±0.14	3.75	0.22
GRB170728B	1.272	47.7	Optical	-	23.31±0.10	0.99	8.30E-03
GRB170817	0.00979	2.64	Optical	KN ^{1,10,11}	12.16±0.01	10.31	4.90E-04
GRB180418A	1.094 ^{+0.78} _{-0.63}	2.29	Optical	EE	25.69±0.21	0.16	1.50E-03
GRB180618A	0.643 ^{+0.09} _{-0.09}	47.4	Optical	EE	23.47±0.13	1.54	8.20E-03
GRB180805B	0.661	123	X-ray	EE	22.15±0.06	3.44	0.042
GRB181123B	1.75	0.260	Optical	-	23.84±0.19	0.59	4.40E-03
GRB191031D	1.607 ^{+0.33} _{-0.24}	0.290	X-ray	-	24.46±0.26	1.53	0.043
GRB200219A	0.457 ^{+0.18} _{-0.21}	288	X-ray	EE	20.66±0.05	1.38	2.20E-03
GRB200411A	1.145 ^{+0.07} _{-0.06}	0.220	X-ray	-	22.56±0.04	4.91	0.11
GRB200522A	0.554	0.620	Optical	KN ¹²	21.28±0.05	0.14	3.50E-05
GRB201221D	1.055	0.160	Optical	-	23.42±0.08	3.57	0.12
GRB210323A	0.733	1.12	Optical	-	24.97±0.25	0.80	0.013
GRB210510A	0.221	1.34	Optical	-	21.03±0.09	1.34	2.79E-03
GRB210726A	0.458 ^{+0.17} _{-0.18}	0.390	X-ray	-	22.16±0.09	0.04	7.30E-05
GRB210919A	0.242	0.160	X-ray	-	20.50±0.05	13.28	0.13
GRB211023B	0.862	1.30	Optical	-	24.36±0.38	0.49	4.70E-03

Continued on next page

Table 1 – continued from previous page

GRB	redshift	T_{90} [sec]	AG detection ^a	LC Feature ^b	m_r [ABmag]	Offset [arcsec]	P_{CC}
GRB211211A	0.0763	51.4	Optical	KN ^{13,14}	19.46±0.04	5.44	0.013
GRB211227A	0.228	83.8	X-ray	KN ^{15,16}	19.26±0.05	0.38	5.76E-05
GRB221120A	0.08 ^{+0.04} _{-0.03}	0.640	Optical	-	17.53±0.05	15.66	0.025

Notes:

^a Afterglow detection methods. ‘Optical’ and ‘X-ray’ indicate afterglows detected by *Swift* UVOT and XRT, respectively. ‘None’ represents samples only detected by γ -ray, but coincide with local bright galaxies.

^b Light curve emission features. ‘KN’ indicates possible kilonova emission included in the light curve, and ‘EE’ represents the extended emission feature in the prompt emission. **Reference** ¹Ascenzi et al. (2019), ²Rossi et al. (2020), ³Gao et al. (2017), ⁴Jin et al. (2021), ⁵Yang et al. (2015), ⁶Jin et al. (2020), ⁷Tanvir et al. (2013), ⁸Troja et al. (2018), ⁹Troja et al. (2019), ¹⁰Cowperthwaite et al. (2017), ¹¹Tanvir et al. (2017), ¹²Fong et al. (2021), ¹³Rastinejad et al. (2022), ¹⁴Yang et al. (2022), ¹⁵Zhu et al. (2022), ¹⁶Lü et al. (2022).

3. PHOTOMETRIC DATA COLLECTION

All the data used in this study are derived either from archival image data or from publicly available observational studies. For each host galaxy, direct photometry was performed wherever images were available, while for others, published photometry information was utilized. We ensured consistent magnitude extraction from these varied sources by carefully adjusting the photometric apertures. Additionally, we gathered filter curves corresponding to each instrument and conducted extinction corrections uniformly. This photometric data, in conjunction with redshift information, are instrumental for the SED fitting discussed in the following section.

3.1. Imaging Survey Data

Large-area survey data enable the collection of photometric information for host galaxies at arbitrary coordinates. This approach allows for the utilization of accurately calibrated multi-wavelength photometric data. Additionally, survey image data are free from contamination by transients, providing reliable magnitudes. Despite limitations in depth, we endeavored to collect extensive photometric information from brighter galaxies.

For optical data, we queried images from the Pan-STARRS (PS1) DR2 (Tonry et al. 2012; Chambers et al. 2016) and the Sloan Digital Sky Survey (SDSS) DR12 (Alam et al. 2015). For targets in the southern hemisphere, images from the Dark Energy Survey (DES) DR2 (Abbott et al. 2021c) and the Dark Energy Camera Legacy Survey (DECaLS) DR8 (Dey et al. 2019) were used.

UV and NIR survey data were also incorporated. The Galactic Evolution Explorer (GALEX) provided *NUV*-band data (Martin et al. 2005), while the Wide-field Infrared Survey Explorer (WISE) (Wright et al. 2010), UKIRT Hemisphere Survey (UHS) (Dye et al.

2018), and UKIRT Infrared Deep Sky Survey (UKIDSS) (Lawrence et al. 2007, 2012) supplied NIR magnitudes. These values were directly referenced from their respective source catalogs. Additional data were accessed through the Gemini Observatory Archive and the Mikulski Archive for Space Telescopes (MAST), with detailed sources recorded in Table A1.

In photometry, **Source Extractor** was used, adopting **AUTO** apertures to estimate total magnitudes for extended sources (Bertin & Arnouts 1996). We utilized **MAG_AUTO** for each band image as the photometric value, instead of unifying all aperture sizes with dual-mode photometry. Regarding the magnitude zero-point calibration of PS1 images, field stars in the PS1 catalog were used as secondary standard stars. For DES and DECaLS data, standardized zero-points of 30.0 ABmag and 22.5 ABmag were adopted, respectively.

Finally, galactic extinction correction was performed using $E(B-V)$ estimates from Schlafly & Finkbeiner 2011 (SF11), a recalibration of the dust map by Schlegel et al. 1998 (SFD98). Extinction values were converted using the curve from Fitzpatrick (1999), adopting $R_V=3.1$.

3.2. Data in Literature

We collected magnitudes of host galaxies published in previous studies to supplement our photometric data. Notably, several population studies have targeted sGRB host galaxies. Leibler & Berger (2010) compiled optical/NIR photometric data for 19 host galaxies. Additionally, Fong et al. (2013) provided in-depth photometric information for 10 sGRB host galaxies using the Hubble Space Telescope (HST). A detailed review of 39 known sGRB host galaxies was conducted by Berger (2014).

Recent deep survey observations have significantly expanded the catalog of known sGRB host galaxies.

O'Connor et al. (2022a) used the 4.3m Lowell Discovery Telescope for deep observations (to $r \gtrsim 25$ ABmag) in fields of X-ray or optical sGRB afterglows, where the host galaxies were previously unknown. In cases with unclear coincident host galaxies, further in-depth observations ($r \gtrsim 26$ -28 ABmag) were carried out using the Gemini and Keck-I telescopes. Systematic observations ($r \simeq 24$ -26 ABmag) of all 90 sGRBs with afterglows discovered by *Swift* from 2005 to 2021 were performed by Fong et al. (2022), providing multi-band photometry for 84 of them and spectral data for 25 bright galaxies. For the rest of 6 sGRBs, no definitive host galaxy was identified despite optical/NIR observations reaching depths of 26-28 ABmag.

The comprehensive and systematic efforts of these studies have yielded extensive optical and NIR band photometric data. Some corrections, however, were necessary in specific cases. For instance, the host galaxy of GRB 161104A, situated in a cluster, was studied by Nugent et al. (2020) using a smaller aperture to mitigate nearby galaxy effects. This approach may underestimate the galaxy's stellar mass compared to others in the SED modeling. Thus, we re-analyzed the r -band image from the Gemini Observatory Archive and calculated MAG_AUTO. We obtained the brightness difference of 0.38 ABmag compared to Nugent et al. (2020), which was considered as an aperture correction factor and was applied to other bands.

Another case warranting careful examination involved the host of GRB 051210, for which the r and i band fluxes demonstrated inadequate fits in their SED, as documented in (Leibler & Berger 2010). An analysis of the DES data indicated that the i -band magnitude should be adjusted to be approximately 0.5 mag brighter. Furthermore, the $F675W = 21.14 \pm 0.05$ reported in (Fong et al. 2010) was deemed potentially inaccurate due to its higher brightness in comparison to the r -band magnitude. Instead, $F675W = 23.7$, derived through GALFIT modeling in the same study, was adopted. By revising the magnitudes for the fitting process, we considered this galaxy to be a comparatively less massive galaxy at $z \sim 0.6$, as opposed to being a higher-redshift galaxy as initially conjectured. Due to the absence of spectroscopic redshift data, the estimated properties of this host galaxy remain relatively uncertain. The data referenced herein and findings from previous surveys are listed in Table A1 in the appendix.

3.3. Galactic Extinction Correction

One of the conscious tasks of unifying photometric data from various references is the galactic extinction correction. To determine the amount of dust, the SFD98

dust map used IRAS and COBE all-sky observation data, while recent studies have often used SF11, which conducted additional calibration to the SFD98 work.

The correction values of SF11 are approximately 14% lower than those of SFD98. To maintain consistency, we recalibrated the magnitudes from referenced papers that used SFD as the basis for extinction correction. We queried the values of E(B-V) at the locations of each host galaxy from the extinction calculator provided by the NASA Extragalactic Database (NED). This allowed us to accurately correct for E(B-V) because extinction values for the Landolt B and V filters are given according to the methods of SFD98 and SF11. While some studies have referred Cardelli et al. (1989) for the extinction law, we regarded the uncertainty arising from this difference as negligible.

3.4. Filter Transmission Curves

We are utilizing photometric values collected from various surveys and independent papers, so it is necessary to reflect the filter transmission curves suitable for each instrument to accurately measure the flux density at each wavelength. The Spanish Virtual Observatory (SVO) filter profile service provides filter curves for various instruments, making it convenient to utilize the filter information used in this study (Rodrigo & Solano 2020). For the filter profiles that are not available in the SVO service, we adopted the profiles provided by each respective observatory. Details of the instruments, filter, and corresponding central wavelengths can be found in the Table A1 in the appendix.

4. HOST GALAXY PROPERTIES

In this section, we outline the method of estimating the properties of host galaxies. Utilizing the photometric data and spectroscopic redshift, the best-fit stellar population model was determined, providing information on galaxies' various properties. Additionally, we applied a similar approach to the control sample galaxies for comparative analysis.

4.1. Photometric Redshift Estimation

Before conducting SED fitting, it was necessary to estimate photometric redshifts (photo-z) for targets lacking spectroscopic data. Among the 80 samples, 20 galaxies required photo-z measurements, each with more than five broad-band photometry data points. We used the software Easy and Accurate Redshifts from Yale (EAZY; Brammer et al. 2008) for this task

The magnitudes and filter information were input into EAZY, and the data points were compared to synthetic models from Bruzual & Charlot (2003) to determine the

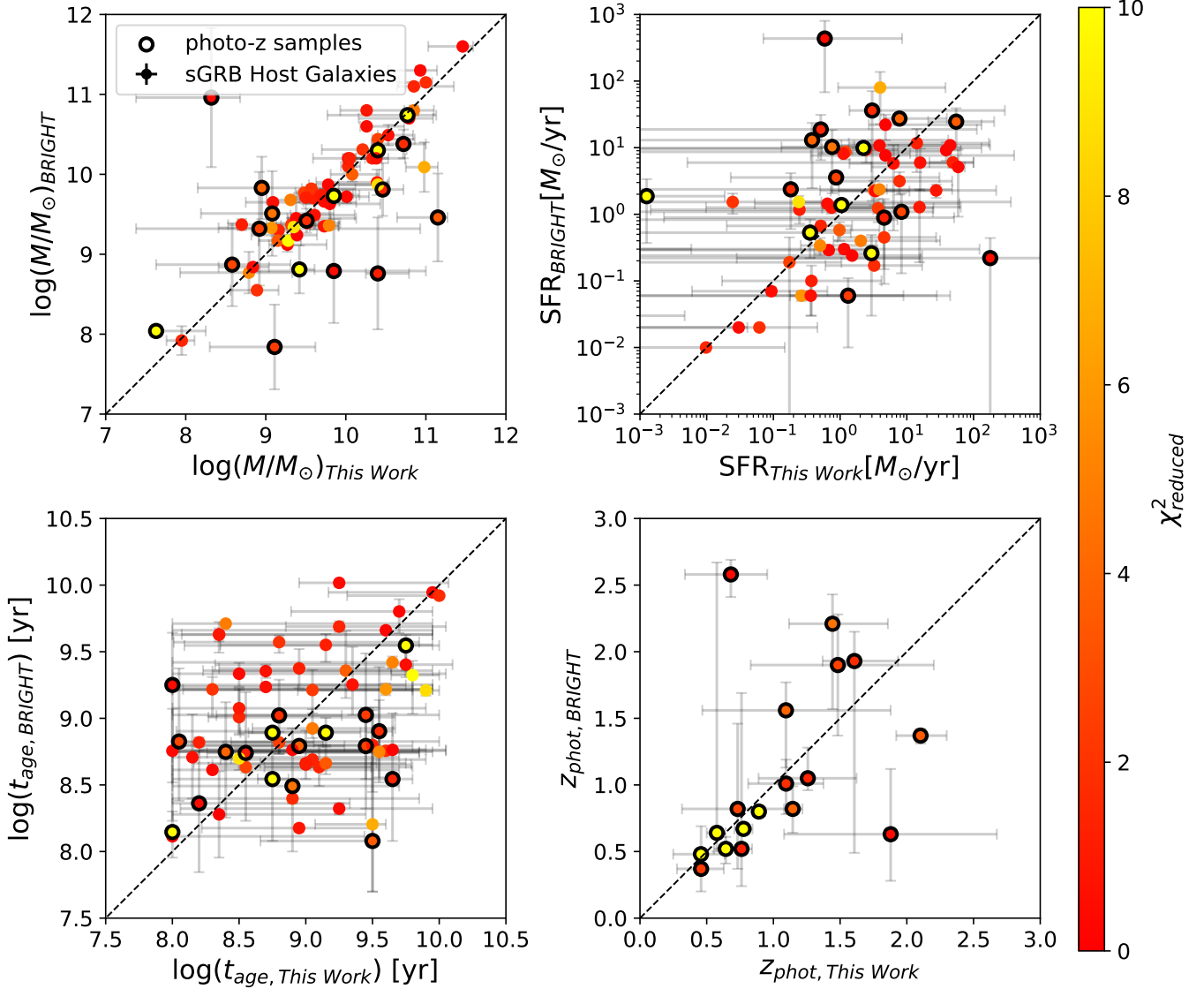


Figure 2. A comparison of host galaxy properties derived from our SED fitting and photometric redshifts with those from Nugent et al. (2022). The comparison is made for 67 galaxies that are cataloged in both studies. The properties compared are the stellar mass (**top-left**), the star formation rate (**top-right**), the stellar population age (**bottom-left**), and the photometric redshift (**bottom-right**). The data points with black outlines indicate the host galaxy samples lacking spectroscopic redshift data. In each panel, the x-axis represents values reported in this work, while the y-axis corresponds to those reported by Nugent et al. (2022). The colored scale reflects the reduced chi-squared values from the SED fitting.

best-fit model via χ^2 minimization. The redshift range for fitting extended from 0 to 3, with each step size set at $0.01 \times (1+z)$.

It is important to note that photo-z estimates can sometimes exhibit color degeneracy across different redshift ranges. Following the methodology of Brammer et al. (2008), we used the r -band apparent magnitude as a prior, allowing for more reasonable photo-z estimates by considering luminosity function in a cosmic volume.

In alignment with our objective to study BNS mergers in the nearby universe, our analysis was limited to

host galaxies at $z < 0.5$. We determined the representative photo-z as the z_{m2} parameter of EAzy output. The z_{m2} represent the redshift marginalized over the posterior distribution, which is generally considered the best photo-z estimate. Within this range, we identified three host galaxies with photo-z are suitable for inclusion to the $z < 0.5$ sample: GRB 200219A ($z_{\text{phot}} = 0.457^{+0.177}_{-0.208}$), GRB 210726A ($z_{\text{phot}} = 0.458^{+0.170}_{-0.181}$), and GRB 221120A ($z_{\text{phot}} = 0.08^{+0.036}_{-0.032}$). When comparing our photo-z estimates to those derived in Nugent et al. (2022), we find a generally reasonable agreement within

measurement errors (Figure 2). Notably, there are no instances where the photo- z of a host galaxy was estimated to be less than 0.5 in other studies but excluded from our criteria.

GRB 051210 ($z_{phot} = 0.681_{-0.344}^{+0.273}$) and GRB 151229A ($z_{phot} = 1.879_{-0.799}^{+0.796}$) show significant discrepancies compared to the literature values. For GRB 051210, this difference arises from updates to the photometric data. We found that the SED model presented by [Leibler & Berger \(2010\)](#) did not adequately explain the observations in the r and i bands. To improve the model, we incorporated i -band data from DES and $F675W$ magnitude from [Fong et al. \(2010\)](#). This resulted in a more reasonable SED model and a lower photo- z estimate. In contrast, for GRB 151229A, the absence of detections in the g and r bands makes photo- z measurements highly uncertain for both our estimates and those in the literature.

We also note that the posterior distribution of GRB 200219A is bimodal with the redshift peaks at $z = 0.28$ and 0.6. We classified this sample as $z < 0.5$ based on the estimate of $z_{m2} = 0.458$, but the exclusion of this object from the $z < 0.5$ sample or adaption of the $z = 0.28$ value for the redshift should not significantly affect our analysis results.

4.2. SED Modelling

Estimating the spectral energy distribution (SED) using multi-wavelength data of galaxies is an effective approach to inferring their global properties. Although SED fitting results are available for most of our sGRB host galaxies, they are collected from various sources that used different SED fitting methods which could create a bias in subsequent analysis results. Hence, we decided to perform the SED fitting for all of our sample host galaxies adopting a single, consistent method. We employed the Fitting and Assessment of Synthetic Templates (FAST; [Kriek et al. 2009](#)) program, which interworks with the photo- z outputs from EAzy.

We adopted the stellar population library from [Bruzual & Charlot 2003](#) (BC03) and assumed the initial mass function of [Chabrier \(2003\)](#). The dust attenuation law was based on [Calzetti et al. \(2000\)](#). We assumed a delayed exponential form for the star formation history (SFH), represented as $SFR \propto t \times \exp(-t/\tau)$, where τ is the e-folding time scale of SFR.

The output parameter space was established as a grid. Specifically, we varied $\log(\tau/\text{yr})$ in 0.1 steps within the range [7.6, 10.0]. We also varied $\log(t_{age}/\text{yr})$, the mean stellar population age, in 0.1 steps within the range [8.0, 10.1]. To ensure that the stellar population age does not exceed the age of the Universe at each redshift of the host galaxy, we set the maximum age limit to be the age of the Universe at that specific redshift. A_V was varied in units of 0.1mag within the range of [0, 4.7], and three values were adopted for the metallicity parameter Z/Z_\odot as subsolar (0.004, 0.008), solar (0.02) and supersolar (0.05).

We determined the best-fit model for the given flux and redshift through the aforementioned process. Each fitting process involved 100 Monte Carlo simulations within the error range of the input flux, from which the best-fit parameters and their 1σ errors were estimated. The results are tabulated in Table 2, with each column representing the redshift, the stellar mass, the star formation rate, the stellar age, the metallicity, the attenuation, and the reduced χ^2 , respectively.

In Figure 2, we compared the stellar mass, the star formation rate, and the mean stellar population age values from our SED fitting with the results from previous studies ([Nugent et al. 2022](#)). While we used the same initial mass function ([Chabrier 2003](#)) and the star formation history (SFH) model, [Nugent et al. \(2022\)](#) adopted the Flexible Stellar Population Synthesis (FSPS) as the stellar population model and the Milky Way extinction law for the host internal extinction ([Conroy et al. 2009](#); [Cardelli et al. 1989](#)).

The stellar mass values from the two studies are almost consistent within the error range, except for a few galaxies with inaccurate photo- z estimates. For example, the i -band magnitude of the GRB 051210 host galaxy, as explained in Section 3, was updated by us, lowering the estimated stellar mass value by about two orders of magnitude compared to the value from [Nugent et al. \(2022\)](#). SFR estimates from the two studies are generally in agreement with each other within errors but with relatively large errors compared to the stellar masses. The large errors in mean stellar age comparisons highlighted the challenges in precise age determination due to the color and metallicity degeneracy.

Table 2. The Best-fit Parameters of the GRB Host Galaxies

GRB	redshift	$\log(M_*)$ [M_\odot]	$\log(\text{SFR})$ [M_\odot/yr]	$\log(\text{sSFR})$ [yr^{-1}]	Type ^a	t_{age} [Gyr]	Z [Z_\odot]	A_V [mag]	χ^2_{reduced}
GRB050509B	0.225	$11.46^{+0.11}_{-0.39}$	$0.42^{+0.13}_{-0.00}$	$-11.04^{+0.20}_{-0.00}$	Q	$8.91^{+1.09}_{-7.33}$	$0.004^{+0.02}_{-0.00}$	$0.4^{+0.55}_{-0.40}$	0.24
GRB050709	0.161	$8.89^{+0.27}_{-0.33}$	$-1.21^{+0.87}_{-0.97}$	$-10.1^{+1.05}_{-0.97}$	SF	$3.98^{+7.24}_{-3.71}$	$0.004^{+0.03}_{-0.00}$	$0.2^{+1.03}_{-0.20}$	1.76
GRB050724	0.254	$11.0^{+0.14}_{-0.87}$	$0.51^{+2.08}_{-0.54}$	$-10.48^{+2.86}_{-0.55}$	SF	$10.0^{+0.00}_{-9.90}$	$0.05^{+0.00}_{-0.05}$	$0.2^{+2.58}_{-0.20}$	1.67
GRB050813	0.719	$10.21^{+0.59}_{-0.51}$	$-0.65^{+3.36}_{-0.00}$	$-10.86^{+2.93}_{-0.00}$	Q	$0.63^{+6.45}_{-0.53}$	$0.008^{+0.04}_{-0.00}$	$1.4^{+2.65}_{-1.40}$	1.97
GRB050906	0.0308	$10.23^{+0.33}_{-0.45}$	$-0.9^{+2.71}_{-0.00}$	$-11.13^{+3.16}_{-0.00}$	Q	$0.71^{+11.88}_{-0.58}$	$0.02^{+0.02}_{-0.02}$	$0.4^{+0.98}_{-0.40}$	0.63
GRB051210	$0.681^{+0.27}_{-0.34}$	$8.32^{+0.39}_{-0.98}$	$-0.23^{+1.18}_{-1.14}$	$-8.55^{+0.94}_{-0.58}$	SF	$0.16^{+2.24}_{-0.06}$	$0.05^{+0.00}_{-0.05}$	$0.0^{+1.14}_{-0.00}$	0.41
GRB051221A	0.546	$9.16^{+0.23}_{-0.19}$	$-0.29^{+0.42}_{-1.07}$	$-9.45^{+0.50}_{-0.96}$	SF	$1.12^{+6.29}_{-0.88}$	$0.004^{+0.01}_{-0.00}$	$0.0^{+0.44}_{-0.00}$	1.36
GRB060502B	0.287	$11.08^{+0.12}_{-0.56}$	$0.06^{+0.58}_{-0.00}$	$-11.02^{+0.70}_{-0.00}$	Q	$10.0^{+0.00}_{-9.15}$	$0.008^{+0.04}_{-0.00}$	$0.1^{+1.33}_{-0.10}$	0.39
GRB060505	0.0894	$9.33^{+0.38}_{-0.41}$	$0.4^{+0.97}_{-0.70}$	$-8.93^{+1.31}_{-0.96}$	SF	$1.78^{+10.81}_{-1.68}$	$0.004^{+0.05}_{-0.00}$	$0.6^{+0.90}_{-0.60}$	1.17
GRB060614	0.125	$7.95^{+0.13}_{-0.19}$	$-2.01^{+1.14}_{-1.12}$	$-9.96^{+1.19}_{-1.12}$	SF	$0.32^{+3.31}_{-0.13}$	$0.05^{+0.00}_{-0.05}$	$0.8^{+0.64}_{-0.80}$	1.44
GRB060801	1.13	$9.27^{+0.39}_{-0.21}$	$1.59^{+0.22}_{-1.07}$	$-7.68^{+0.07}_{-1.13}$	SF	$0.1^{+1.56}_{-0.00}$	$0.05^{+0.00}_{-0.05}$	$1.0^{+0.34}_{-1.00}$	0.14
GRB061006	0.461	$8.7^{+0.47}_{-0.17}$	$-0.43^{+1.07}_{-1.34}$	$-9.13^{+1.14}_{-1.19}$	SF	$0.22^{+8.69}_{-0.11}$	$0.008^{+0.04}_{-0.00}$	$0.7^{+0.71}_{-0.70}$	1.15
GRB061210	0.41	$9.48^{+0.11}_{-0.11}$	$-0.76^{+0.90}_{-0.73}$	$-10.24^{+0.87}_{-0.73}$	SF	$0.63^{+0.85}_{-0.36}$	$0.05^{+0.00}_{-0.03}$	$0.3^{+0.81}_{-0.30}$	2.45
GRB070429B	0.902	$10.4^{+0.42}_{-0.07}$	$0.08^{+1.45}_{-0.48}$	$-10.32^{+1.42}_{-0.48}$	SF	$0.35^{+5.96}_{-0.15}$	$0.004^{+0.04}_{-0.00}$	$1.4^{+0.65}_{-1.18}$	2.59
GRB070714B	0.923	$9.32^{+0.34}_{-0.31}$	$0.57^{+0.83}_{-0.84}$	$-8.75^{+1.13}_{-1.12}$	SF	$1.12^{+5.19}_{-1.02}$	$0.004^{+0.02}_{-0.00}$	$0.9^{+0.80}_{-0.90}$	2.19
GRB070724	0.457	$10.01^{+0.28}_{-0.41}$	$0.59^{+1.07}_{-0.38}$	$-9.42^{+1.47}_{-0.55}$	SF	$1.78^{+7.13}_{-1.67}$	$0.02^{+0.03}_{-0.02}$	$0.3^{+1.13}_{-0.30}$	0.36
GRB070729	$0.761^{+0.08}_{-0.08}$	$10.4^{+0.27}_{-0.13}$	$0.66^{+1.00}_{-1.11}$	$-9.74^{+0.93}_{-1.11}$	SF	$0.35^{+3.54}_{-0.16}$	$0.05^{+0.00}_{-0.05}$	$1.6^{+0.90}_{-1.36}$	1.20
GRB070809	0.473	$10.85^{+0.48}_{-0.12}$	$-0.1^{+0.96}_{-0.00}$	$-10.95^{+0.93}_{-0.00}$	Q	$1.12^{+7.79}_{-0.73}$	$0.02^{+0.03}_{-0.02}$	$0.7^{+1.12}_{-0.70}$	4.69
GRB070810B	0.0385	$10.73^{+0.03}_{-0.25}$	$-0.39^{+0.00}_{-0.00}$	$-11.12^{+0.00}_{-0.00}$	Q	$12.59^{+0.00}_{-7.09}$	$0.004^{+0.00}_{-0.00}$	$0.4^{+0.21}_{-0.11}$	3.80
GRB071227	0.381	$10.53^{+0.31}_{-0.13}$	$0.8^{+0.91}_{-0.66}$	$-9.73^{+1.02}_{-0.88}$	SF	$2.24^{+6.67}_{-1.77}$	$0.05^{+0.00}_{-0.04}$	$1.2^{+1.25}_{-1.00}$	0.63
GRB080121	0.045	$8.97^{+0.48}_{-0.26}$	$-0.58^{+0.79}_{-1.03}$	$-9.55^{+0.91}_{-0.77}$	SF	$1.41^{+11.18}_{-1.22}$	$0.004^{+0.02}_{-0.00}$	$0.2^{+0.81}_{-0.20}$	1.53
GRB080123	0.495	$10.03^{+0.15}_{-0.09}$	$0.39^{+0.48}_{-0.21}$	$-9.65^{+0.55}_{-0.21}$	SF	$1.26^{+1.83}_{-0.77}$	$0.05^{+0.00}_{-0.03}$	$0.2^{+0.67}_{-0.20}$	1.33
GRB090510	0.903	$9.79^{+0.23}_{-0.19}$	$-0.13^{+0.94}_{-0.88}$	$-9.92^{+0.97}_{-0.88}$	SF	$1.0^{+3.47}_{-0.79}$	$0.004^{+0.05}_{-0.00}$	$0.0^{+0.93}_{-0.00}$	0.78
GRB090515	0.403	$10.93^{+0.21}_{-0.40}$	$-0.04^{+0.17}_{-0.00}$	$-10.97^{+0.09}_{-0.00}$	Q	$5.01^{+3.90}_{-4.16}$	$0.02^{+0.03}_{-0.02}$	$0.0^{+1.54}_{-0.00}$	0.30
GRB100117	0.914	$10.33^{+0.12}_{-0.20}$	$-0.47^{+0.20}_{-0.00}$	$-10.8^{+0.19}_{-0.00}$	Q	$1.0^{+2.09}_{-0.53}$	$0.008^{+0.04}_{-0.00}$	$1.0^{+0.63}_{-0.69}$	1.06
GRB100206A	0.407	$10.79^{+0.28}_{-0.63}$	$0.68^{+1.93}_{-0.86}$	$-10.11^{+2.49}_{-0.86}$	SF	$3.98^{+4.93}_{-3.88}$	$0.05^{+0.00}_{-0.05}$	$1.0^{+2.33}_{-0.84}$	0.14
GRB100216A	0.038	$8.87^{+0.12}_{-0.20}$	$-0.89^{+0.41}_{-1.36}$	$-9.77^{+0.41}_{-1.35}$	SF	$1.12^{+1.76}_{-0.85}$	$0.004^{+0.01}_{-0.00}$	$0.1^{+0.43}_{-0.10}$	1.08
GRB100625A	0.452	$9.6^{+0.42}_{-0.18}$	$-0.69^{+1.26}_{-0.66}$	$-10.29^{+1.28}_{-0.66}$	SF	$1.41^{+7.50}_{-1.18}$	$0.05^{+0.00}_{-0.05}$	$0.4^{+1.55}_{-0.40}$	1.15
GRB100816A	0.805	$10.37^{+0.43}_{-0.11}$	$1.0^{+0.97}_{-1.01}$	$-9.37^{+1.01}_{-1.19}$	SF	$0.25^{+6.06}_{-0.12}$	$0.008^{+0.04}_{-0.00}$	$1.4^{+0.65}_{-1.40}$	4.57
GRB101219A	0.718	$9.52^{+0.41}_{-0.43}$	$0.89^{+0.79}_{-0.82}$	$-8.63^{+1.02}_{-1.08}$	SF	$0.79^{+6.29}_{-0.69}$	$0.05^{+0.00}_{-0.05}$	$1.5^{+0.92}_{-1.15}$	1.70
GRB101224A	0.454	$9.15^{+0.15}_{-0.24}$	$-0.01^{+0.61}_{-0.42}$	$-9.16^{+0.75}_{-0.30}$	SF	$1.41^{+4.21}_{-1.27}$	$0.008^{+0.04}_{-0.00}$	$0.0^{+0.76}_{-0.00}$	3.41
GRB110402A	0.854	$9.44^{+0.64}_{-0.59}$	$0.02^{+1.30}_{-0.73}$	$-9.42^{+1.68}_{-0.61}$	SF	$1.78^{+4.53}_{-1.68}$	$0.02^{+0.03}_{-0.02}$	$0.0^{+1.47}_{-0.00}$	0.86
GRB111117A	2.21	$9.8^{+0.64}_{-0.31}$	$0.68^{+1.44}_{-0.25}$	$-9.13^{+1.51}_{-0.33}$	SF	$0.22^{+2.60}_{-0.12}$	$0.008^{+0.04}_{-0.00}$	$0.1^{+1.01}_{-0.10}$	0.10
GRB120305A	0.225	$9.28^{+0.16}_{-0.09}$	$-1.76^{+0.00}_{-0.00}$	$-11.04^{+0.00}_{-0.00}$	Q	$6.31^{+3.69}_{-1.94}$	$0.004^{+0.00}_{-0.00}$	$0.0^{+0.09}_{-0.00}$	20.20
GRB120630A	$0.544^{+0.13}_{-0.08}$	$9.83^{+0.40}_{-0.40}$	$1.34^{+0.66}_{-0.81}$	$-8.49^{+0.88}_{-1.09}$	SF	$0.18^{+8.73}_{-0.08}$	$0.05^{+0.00}_{-0.03}$	$1.5^{+0.62}_{-1.10}$	0.28
GRB120804A	$1.258^{+0.36}_{-0.37}$	$10.46^{+0.26}_{-0.93}$	$-0.24^{+2.29}_{-0.00}$	$-10.7^{+3.08}_{-0.00}$	Q	$4.47^{+1.84}_{-4.37}$	$0.004^{+0.05}_{-0.00}$	$0.9^{+2.94}_{-0.90}$	1.46
GRB121226A	$2.103^{+0.20}_{-0.18}$	$11.15^{+0.12}_{-0.47}$	$1.74^{+0.49}_{-0.43}$	$-9.42^{+0.94}_{-0.33}$	SF	$3.16^{+0.00}_{-2.48}$	$0.05^{+0.00}_{-0.05}$	$1.1^{+0.54}_{-0.44}$	5.26
GRB130515A	$0.891^{+0.05}_{-0.05}$	$10.4^{+0.03}_{-0.08}$	$0.47^{+0.11}_{-0.88}$	$-9.93^{+0.09}_{-0.88}$	SF	$0.56^{+0.07}_{-0.21}$	$0.02^{+0.02}_{-0.01}$	$0.5^{+0.13}_{-0.27}$	29.70
GRB130603B	0.357	$9.57^{+0.54}_{-0.11}$	$0.66^{+0.76}_{-0.67}$	$-8.91^{+0.84}_{-1.16}$	SF	$0.2^{+8.71}_{-0.07}$	$0.004^{+0.05}_{-0.00}$	$1.4^{+0.33}_{-1.40}$	1.99
GRB130822A	0.154	$10.03^{+0.50}_{-0.44}$	$0.06^{+2.03}_{-1.10}$	$-9.97^{+2.35}_{-1.10}$	SF	$0.32^{+10.90}_{-0.22}$	$0.008^{+0.04}_{-0.00}$	$1.5^{+0.81}_{-1.50}$	0.38
GRB140129B	0.43	$9.07^{+0.24}_{-0.09}$	$-0.58^{+1.53}_{-0.17}$	$-9.65^{+2.03}_{-0.32}$	SF	$3.98^{+4.93}_{-3.88}$	$0.05^{+0.00}_{-0.05}$	$0.0^{+1.93}_{-0.00}$	5.87
GRB140622A	0.959	$10.05^{+0.21}_{-0.09}$	$1.69^{+0.32}_{-0.35}$	$-8.35^{+0.37}_{-0.36}$	SF	$0.16^{+1.04}_{-0.06}$	$0.05^{+0.00}_{-0.02}$	$1.5^{+0.24}_{-0.32}$	1.22
GRB140903A	0.353	$10.26^{+0.55}_{-0.33}$	$1.44^{+0.90}_{-1.46}$	$-8.81^{+1.19}_{-1.80}$	SF	$0.22^{+8.69}_{-0.12}$	$0.008^{+0.04}_{-0.00}$	$2.5^{+0.47}_{-2.38}$	0.89
GRB140930B	1.465	$9.38^{+0.75}_{-0.10}$	$1.77^{+0.10}_{-1.29}$	$-7.61^{+0.00}_{-2.01}$	SF	$0.1^{+4.37}_{-0.00}$	$0.02^{+0.03}_{-0.02}$	$1.4^{+0.26}_{-1.40}$	0.32

Continued on next page

GRB	redshift	$\log(M_*)$ [M_\odot]	$\log(\text{SFR})$ [M_\odot/yr]	$\log(\text{sSFR})$ [yr^{-1}]	Type ^a	t_{age} [Gyr]	Z [Z_\odot]	A_V [mag]	χ^2_{reduced}
GRB141212A	0.596	$9.5^{+0.20}_{-0.15}$	$-0.61^{+1.11}_{-0.79}$	$-10.11^{+1.02}_{-0.79}$	SF	$0.89^{+3.00}_{-0.66}$	$0.05^{+0.00}_{-0.05}$	$0.0^{+1.39}_{-0.00}$	1.11
GRB150101B	0.134	$10.85^{+0.50}_{-0.21}$	$-0.23^{+1.38}_{-0.00}$	$-11.08^{+1.26}_{-0.00}$	Q	$1.78^{+9.44}_{-1.07}$	$0.008^{+0.04}_{-0.00}$	$0.7^{+0.88}_{-0.70}$	1.40
GRB150120A	0.46	$10.08^{+0.34}_{-0.27}$	$0.51^{+0.84}_{-0.74}$	$-9.57^{+1.01}_{-1.03}$	SF	$2.0^{+6.91}_{-1.82}$	$0.008^{+0.03}_{-0.00}$	$1.3^{+0.94}_{-0.95}$	3.67
GRB150728A	0.461	$9.73^{+0.25}_{-0.19}$	$0.05^{+1.04}_{-0.38}$	$-9.68^{+1.10}_{-0.34}$	SF	$0.89^{+3.09}_{-0.73}$	$0.05^{+0.00}_{-0.05}$	$0.1^{+1.28}_{-0.10}$	0.72
GRB150831A	1.18	$9.61^{+0.50}_{-0.30}$	$1.2^{+0.80}_{-2.31}$	$-8.41^{+0.80}_{-2.31}$	SF	$0.14^{+4.87}_{-0.04}$	$0.008^{+0.04}_{-0.00}$	$1.9^{+0.77}_{-1.90}$	0.60
GRB151229A	$1.879^{+0.80}_{-0.80}$	$9.85^{+1.12}_{-1.08}$	$2.25^{+0.75}_{-2.95}$	$-7.61^{+0.00}_{-2.94}$	SF	$0.1^{+5.52}_{-0.00}$	$0.05^{+0.00}_{-0.05}$	$2.2^{+0.47}_{-2.20}$	0.67
GRB160303A	$1.095^{+0.28}_{-0.28}$	$9.51^{+0.37}_{-0.25}$	$-0.73^{+1.68}_{-0.50}$	$-10.24^{+1.50}_{-0.50}$	SF	$0.63^{+4.50}_{-0.45}$	$0.05^{+0.00}_{-0.05}$	$0.5^{+1.55}_{-0.50}$	3.50
GRB160408A	$1.483^{+0.72}_{-0.65}$	$8.92^{+1.94}_{-1.54}$	$-0.06^{+1.51}_{-1.66}$	$-8.98^{+1.37}_{-1.66}$	SF	$2.82^{+3.49}_{-2.72}$	$0.004^{+0.05}_{-0.00}$	$0.0^{+1.43}_{-0.00}$	2.56
GRB160411A	$0.732^{+0.37}_{-0.42}$	$8.62^{+0.65}_{-0.96}$	$0.95^{+0.22}_{-3.19}$	$-7.67^{+0.06}_{-3.19}$	SF	$0.11^{+9.89}_{-0.01}$	$0.004^{+0.05}_{-0.00}$	$1.6^{+0.75}_{-1.60}$	4.53
GRB160525B	$0.576^{+0.07}_{-0.08}$	$8.25^{+0.17}_{-0.51}$	$-0.08^{+0.42}_{-0.25}$	$-8.32^{+0.70}_{-0.26}$	SF	$0.18^{+0.73}_{-0.08}$	$0.05^{+0.00}_{-0.05}$	$0.0^{+0.31}_{-0.00}$	13.00
GRB160624A	0.484	$9.69^{+0.48}_{-0.58}$	$1.19^{+0.62}_{-1.36}$	$-8.5^{+0.88}_{-1.70}$	SF	$0.32^{+7.62}_{-0.22}$	$0.008^{+0.04}_{-0.00}$	$1.8^{+0.45}_{-1.80}$	0.94
GRB160821B	0.162	$9.39^{+0.25}_{-0.58}$	$0.18^{+1.05}_{-1.86}$	$-9.21^{+1.59}_{-1.86}$	SF	$4.47^{+6.75}_{-4.37}$	$0.004^{+0.05}_{-0.00}$	$0.2^{+0.93}_{-0.20}$	0.06
GRB161001A	$0.776^{+0.07}_{-0.07}$	$10.1^{+0.22}_{-0.27}$	$-0.46^{+0.52}_{-0.28}$	$-10.56^{+0.64}_{-0.28}$	SF	$2.82^{+4.26}_{-2.10}$	$0.004^{+0.02}_{-0.00}$	$0.0^{+0.70}_{-0.00}$	18.25
GRB161104A	0.793	$10.38^{+0.32}_{-0.25}$	$-0.44^{+1.97}_{-0.02}$	$-10.83^{+1.83}_{-0.01}$	SF	$0.5^{+5.81}_{-0.29}$	$0.004^{+0.05}_{-0.00}$	$1.8^{+0.93}_{-1.80}$	0.59
GRB170127B	$1.443^{+0.42}_{-0.33}$	$9.08^{+0.92}_{-0.93}$	$-0.12^{+0.87}_{-0.78}$	$-9.19^{+1.51}_{-0.82}$	SF	$0.79^{+4.22}_{-0.69}$	$0.004^{+0.05}_{-0.00}$	$0.0^{+0.92}_{-0.00}$	4.53
GRB170428A	0.453	$9.31^{+0.44}_{-0.30}$	$0.31^{+1.19}_{-0.41}$	$-9.0^{+1.38}_{-0.79}$	SF	$0.25^{+8.66}_{-0.15}$	$0.05^{+0.00}_{-0.05}$	$1.4^{+1.04}_{-1.01}$	4.85
GRB170728A	1.493	$10.98^{+0.17}_{-0.25}$	$0.6^{+1.01}_{-0.26}$	$-10.38^{+1.03}_{-0.26}$	SF	$3.16^{+0.82}_{-2.04}$	$0.05^{+0.00}_{-0.04}$	$0.6^{+1.27}_{-0.60}$	6.74
GRB170728B	1.272	$9.78^{+0.66}_{-0.25}$	$1.65^{+0.60}_{-1.86}$	$-8.14^{+0.53}_{-1.83}$	SF	$0.2^{+4.81}_{-0.10}$	$0.004^{+0.05}_{-0.00}$	$1.1^{+0.71}_{-1.10}$	0.22
GRB170817	0.00979	$10.26^{+0.44}_{-0.07}$	$-0.87^{+0.00}_{-0.00}$	$-11.13^{+0.00}_{-0.00}$	Q	$1.78^{+9.70}_{-0.87}$	$0.05^{+0.00}_{-0.04}$	$0.4^{+0.90}_{-0.40}$	0.41
GRB180418A	$1.094^{+0.78}_{-0.63}$	$9.13^{+1.61}_{-0.93}$	$1.51^{+1.27}_{-3.12}$	$-7.62^{+0.01}_{-3.12}$	SF	$0.1^{+8.81}_{-0.00}$	$0.004^{+0.05}_{-0.00}$	$2.2^{+1.34}_{-2.20}$	7.56
GRB180618A	$0.643^{+0.09}_{-0.09}$	$9.42^{+0.19}_{-0.00}$	$-1.47^{+0.00}_{-0.00}$	$-10.89^{+0.00}_{-0.00}$	Q	$0.56^{+0.18}_{-0.12}$	$0.05^{+0.00}_{-0.03}$	$0.0^{+0.18}_{-0.00}$	24.33
GRB180805B	0.661	$9.35^{+0.06}_{-0.03}$	$-0.62^{+0.39}_{-0.36}$	$-9.96^{+0.32}_{-0.37}$	SF	$0.32^{+0.07}_{-0.06}$	$0.05^{+0.00}_{-0.03}$	$0.0^{+0.34}_{-0.00}$	8.92
GRB181123B	1.75	$10.39^{+0.15}_{-0.78}$	$1.15^{+1.08}_{-1.02}$	$-9.24^{+1.63}_{-0.51}$	SF	$3.16^{+0.39}_{-3.06}$	$0.05^{+0.00}_{-0.05}$	$0.4^{+1.25}_{-0.40}$	1.16
GRB191031D	$1.607^{+0.33}_{-0.24}$	$10.78^{+0.23}_{-0.46}$	$0.67^{+1.78}_{-0.53}$	$-10.11^{+2.12}_{-0.46}$	SF	$3.98^{+0.49}_{-3.87}$	$0.05^{+0.00}_{-0.05}$	$0.4^{+1.99}_{-0.63}$	2.08
GRB200219A	$0.457^{+0.18}_{-0.21}$	$10.77^{+0.36}_{-0.99}$	$0.35^{+1.77}_{-0.53}$	$-10.42^{+2.25}_{-0.53}$	SF	$5.62^{+4.38}_{-5.49}$	$0.05^{+0.00}_{-0.05}$	$0.2^{+2.85}_{-0.20}$	27.86
GRB200411A	$1.145^{+0.07}_{-0.06}$	$10.57^{+0.21}_{-0.13}$	$0.89^{+0.71}_{-0.24}$	$-9.68^{+0.58}_{-0.19}$	SF	$0.89^{+1.06}_{-0.65}$	$0.05^{+0.00}_{-0.05}$	$0.1^{+0.90}_{-0.10}$	3.90
GRB200522A	0.554	$9.73^{+0.19}_{-0.24}$	$0.53^{+0.51}_{-0.67}$	$-9.2^{+0.65}_{-0.54}$	SF	$0.79^{+7.15}_{-0.63}$	$0.02^{+0.03}_{-0.02}$	$0.2^{+0.70}_{-0.20}$	0.38
GRB201221D	1.055	$9.79^{+0.14}_{-0.63}$	$0.59^{+1.14}_{-0.10}$	$-9.19^{+1.58}_{-0.25}$	SF	$4.47^{+1.15}_{-4.37}$	$0.05^{+0.00}_{-0.05}$	$0.0^{+1.42}_{-0.00}$	5.09
GRB210323A	0.733	$8.79^{+0.54}_{-0.86}$	$-0.3^{+0.84}_{-0.29}$	$-9.09^{+1.47}_{-0.60}$	SF	$3.55^{+3.53}_{-3.45}$	$0.05^{+0.00}_{-0.05}$	$0.0^{+0.93}_{-0.00}$	5.29
GRB210510A	0.221	$9.43^{+0.31}_{-0.34}$	$1.29^{+0.42}_{-0.51}$	$-8.14^{+0.53}_{-0.67}$	SF	$0.11^{+1.89}_{-0.01}$	$0.05^{+0.00}_{-0.04}$	$2.4^{+0.43}_{-0.63}$	1.73
GRB210726A	$0.458^{+0.17}_{-0.18}$	$9.11^{+0.50}_{-0.75}$	$0.12^{+1.33}_{-1.96}$	$-8.99^{+1.37}_{-1.96}$	SF	$2.82^{+6.73}_{-2.72}$	$0.02^{+0.03}_{-0.02}$	$0.0^{+1.28}_{-0.00}$	2.32
GRB210919A	0.242	$10.4^{+0.12}_{-0.49}$	$-0.64^{+0.00}_{-0.00}$	$-11.04^{+0.00}_{-0.00}$	Q	$7.94^{+2.06}_{-7.11}$	$0.02^{+0.03}_{-0.02}$	$0.0^{+1.36}_{-0.00}$	8.66
GRB211023B	0.862	$9.09^{+0.99}_{-0.34}$	$-0.19^{+1.98}_{-1.09}$	$-9.28^{+1.67}_{-1.04}$	SF	$0.5^{+5.81}_{-0.40}$	$0.02^{+0.03}_{-0.02}$	$0.0^{+2.20}_{-0.00}$	0.54
GRB211211A	0.0763	$8.84^{+0.17}_{-0.43}$	$-1.03^{+0.81}_{-0.80}$	$-9.87^{+1.13}_{-0.60}$	SF	$5.62^{+6.97}_{-5.40}$	$0.004^{+0.02}_{-0.00}$	$0.1^{+0.88}_{-0.10}$	0.46
GRB211227A	0.228	$10.23^{+0.13}_{-0.10}$	$-0.5^{+1.36}_{-0.31}$	$-10.73^{+1.27}_{-0.31}$	SF	$0.4^{+0.89}_{-0.15}$	$0.05^{+0.00}_{-0.05}$	$1.3^{+0.70}_{-0.60}$	4.66
GRB221120A	$0.08^{+0.04}_{-0.03}$	$10.06^{+0.46}_{-0.75}$	$0.92^{+1.10}_{-0.92}$	$-9.14^{+1.53}_{-0.73}$	SF	$3.98^{+8.61}_{-3.88}$	$0.05^{+0.00}_{-0.02}$	$1.2^{+0.96}_{-0.62}$	5.65

Notes:

^a Galaxy types according to specific star formation rate. ‘Q’ denotes quiescent galaxies, while ‘SF’ denotes star-forming galaxies.

4.3. Control Sample Galaxies Definition

4.3.1. Galaxies in the COSMOS Field

To quantitatively assess the characteristics of short and hybrid GRB host galaxies, we set a control sample of non-host galaxies. Here, we utilize photometric and spectroscopic catalogs for galaxies in the COSMOS field. The COSMOS field is suitable for establishing a

well-defined control group as it offers photometric information with a wide wavelength range from the UV to MIR, as well as some spectral analysis data.

COSMOS2020 is one of the deepest photometric catalogs available, with an *i*-band 3σ sensitivity limit of 27.0 mag across an effective survey area of 1.27 deg² (Weaver et al. 2022). The COSMOS2020 data cover a

moderately wide area and contain accurate photometric redshifts ($|\Delta z| < 0.025(1+z)$ at $i < 25\text{AB}$), making it suitable for constructing the control sample.

The catalog contains approximately one million sources. To minimize contamination in photometry values (e.g., bright stars affecting galaxy photometry), we selected those with `FCOMBINED` values of 0 (Weaver et al. 2023). Furthermore, we chose sources with `ACSMuClass` values of 1 to ensure a collection of purely extended sources. These constraints return a refined sample of 524,901 galaxies.

The catalog offers information such as photometric redshifts, stellar masses, SFRs, and rest-frame absolute magnitudes from SED fitting. The method of estimating galaxy properties in the existing COSMOS2020 catalog, however, differs from that used for our sGRB host galaxies. Therefore, we performed a new SED fitting for the refined sample of COSMOS2020 galaxies following the same method we used for the sGRB host galaxy sample.

The COSMOS2020 photometric data are collected from various telescopes, including *u*-band from Canada-France-Hawaii Telescope (CFHT), *grizy* from Subaru / HyperSuprime-Cam (HSC), *YJHK_s* from ULTRAVISTA, *FUV* and *NUV* from GALEX, and *F814W* from HST/ACS, which were listed in the THE FARMER version catalog. Additionally, we incorporated spectroscopic redshifts provided by the zCOSMOS (Lilly et al. 2007, 2009) and hCOSMOS (Damjanov et al. 2018) for 8,673 galaxies matched with the photometric catalog within 1 arcsec. For duplicate targets, we referred the hCOSMOS which has higher accuracy.

We fixed the collected photometric and spectroscopic redshift and conducted SED fitting using FAST. The overall processes were similar to the sGRB host analyses in Section 4, but without Monte-Carlo repetitions. When we exclude about 0.7 % of poorly fitted samples with $\chi^2_{reduced} > 5$, the redshift and stellar mass generally agreed well with the values from the COSMOS2020 catalog.

We estimated the rest-frame absolute magnitudes of the fitted galaxies as given below. We first corrected for the effects of redshift on the wavelength and flux of the best-fit model and then performed synthetic photometry using the SDSS *r*-band filter curve. This calculation method includes the concept of the conventional K-correction.

While the hCOSMOS catalog is valuable for providing redshift information for faint galaxies, it lacks completeness for bright galaxies. SDSS DR12 is useful because it offers spectroscopic redshifts for bright galaxies (Alam et al. 2015). We selected SDSS galaxies residing in the COSMOS field and collected their *ugriz* photometric

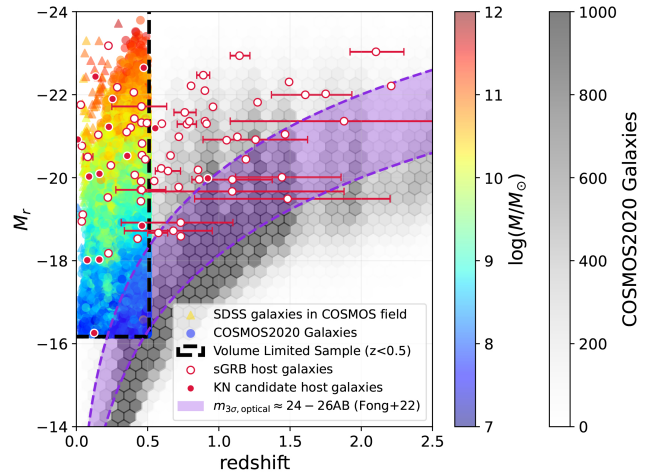


Figure 3. Redshift versus rest-frame absolute *r*-magnitude distribution of COSMOS field galaxies. The dotted-line box represents the volume-limited sample based on $z < 0.5$ and $M_r < -16.22$ mag. The magnitudes of galaxies represented by colored markers were calculated according to the method described in Section 4. The gray hexagon bins indicate the `1pzBEST` and `1pRMAG` parameters in the COSMOS2020 THE FARMER catalog

- The purple-shaded region represents the typical sGRB host survey limiting magnitude (Fong et al. 2022).

data and spectroscopic redshifts when available. We identified 151 galaxies occupying $r < 17.7$ mag and included their spectroscopic redshifts to increase the spectroscopic redshift completeness at the bright end of the COSMOS2020 sample. The absolute magnitude distributions of COSMOS2020 and SDSS DR12 galaxies can be seen in Figure 3.

4.3.2. Volume-limited Sample

Figure 3 shows the absolute magnitudes versus redshifts of host galaxies. At low redshifts ($z \lesssim 0.5$), the majority of host galaxies lie well above the detection limit of the follow-up imaging observations to find GRB host galaxies, but at higher redshifts, the host galaxy magnitudes cut off near the detection limit. This suggests that the higher redshift ($z \gtrsim 0.5$) host galaxy sample could be incomplete due to the imaging depths. Furthermore, the classification of GRBs and assessing their association with host galaxies become more ambiguous at higher redshifts Bromberg et al. (2013). In the near future, the NS-involved GW events are expected to be observed at low redshift, where the properties of their host galaxies would be of interest (Abbott et al. 2018).

Therefore, we decided to construct a volume-limited sample for $z < 0.5$ for the analysis of the host galaxy properties. A volume-limited sample refers to a group that is not biased towards nearby and brighter galaxies

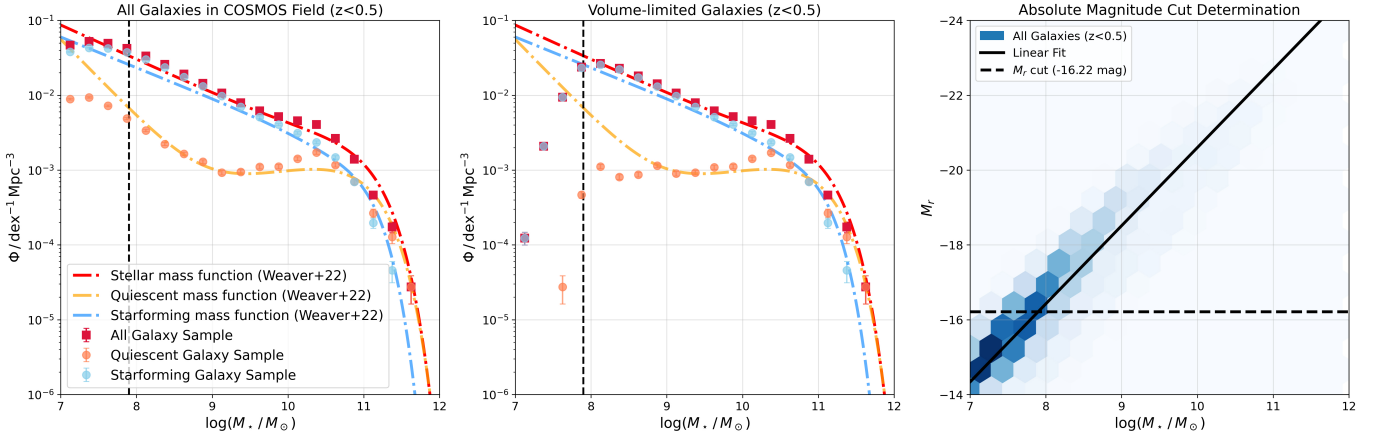


Figure 4. The galaxy stellar mass function for the COSMOS field galaxies at $z < 0.5$, with errors represented solely by Poisson noise (**Left**). The same figure but with a volume-limited COSMOS sample defined by an absolute magnitude cut-off at $M_r < -16.22$ mag (**Middle**). The relationship between stellar mass and r -band absolute magnitude, with a solid line depicting the linear fit for all galaxies at $z < 0.5$. The dotted line represents the absolute magnitude cut corresponding to a stellar mass of $\log(M_*/M_\odot) = 7.9$ (**Right**). In the first two panels, the orange and sky-blue data points refer to the passive galaxies and star-forming galaxies, respectively, which are classified by Equation 1.

by giving an absolute magnitude cut within a given redshift range. Although there could be a certain amount of evolution in galaxies between $z = 0 - 0.5$, limiting the sample to a lower redshift (i.e., smaller volume), for example, $z < 0.3$, would leave only 22 host galaxies available, and hence we opted to set the redshift limit at 0.5 where 39 host galaxies will be available for the analysis.

To define the volume-limited sample, we must set an absolute magnitude cut in the $z - M_r$ plane (Figure 3). This magnitude cut determines the stellar mass completeness, and to determine the cut, we plotted the galaxy stellar mass function (GSMF). In the left panel of Figure 4, the number density of the $z < 0.5$ COSMOS2020 sample as a function of a mass bin is also presented. By comparing this with the result from Weaver et al. (2023), we could confirm that the data set is not fully complete down to $10^7 M_\odot$. Therefore, we chose the lower absolute magnitude limit corresponding to $10^{7.9} M_\odot$ to cover the minimum stellar mass of sGRB host galaxy while maintaining the completeness of the data. In the right panel of Figure 4, we demonstrate that selecting COSMOS field galaxies with $M_r < -16.22$ mag results in a volume-limited COSMOS sample of 35,122 galaxies that adheres to the GSMF down to $\log(M_*/M_\odot) \simeq 8$. This selection criterion excludes about 1.3% of galaxies within the stellar mass range of $8 < \log(M_*/M_\odot) < 9$.

Applying such an absolute magnitude cut to our host galaxies ensures that the entire sample of 39 host galaxies with $z < 0.5$ is included. This allows us to compare the short and hybrid GRB host galaxies and the control sample under the same density conditions. If we

had set a brighter magnitude cut that does not include the mass of faint galaxies like the host galaxy of GRB 060614, we would have compared a smaller number of samples. However, the impact of a single object on the overall results is not significant. The differences in results due to the absolute magnitude cut will be discussed later.

4.3.3. Passive Galaxy Definition

During the SED fitting process, we calculated each galaxy’s star formation rate (SFR). However, we note that some galaxies have $\log(\text{SFR})$ values that tend towards negative infinity, indicating minimal star formation activity. In reality, it is challenging to discern differences between galaxies with low SFRs using broad-band SED due to their negligible variations. Therefore, taking these small values at face value would be unphysical. Moreover, setting SFR to zero complicates the derivation of an analytical solution. To address this issue, we introduce a lower limit and propose using Equation 1 as a suitable criterion.

$$\text{sSFR} < \frac{1}{10 \times t(z)} \quad (1)$$

In the above equation, $t(z)$ represents the universe age at redshift z . Setting such a lower limit of specific SFR (SFR per unit stellar mass) implies that it would take more than 10 times the age of the universe to build the mass of that galaxy assuming current SFR. This makes it a suitable criterion to evaluate galaxies where the SFR has been quenched. While COSMOS2020 used color cut to define passive galaxies sample, both criteria return similar passive galaxies of $\log(\text{sSFR}/\text{yr}) < 10^{-11}$. On

the other hand, some other studies try to define passive galaxies as ones with $sSFR < 1/[3 \times t(z)]$ or higher values. Using such criteria assigns higher $sSFR$ values to passive galaxies, which would influence the assessment of $sSFR$ contribution to the BNS merger rate. We will address this effect in the discussion section.

5. RESULT

In this section, we present the properties of host galaxies estimated from the SED fitting processes in the previous section. From the distributions of stellar masses and star formation activities of the host galaxies, we can determine how they deviate from those of general galaxies. By constructing a weight function that compensates for the deviation, we would be able to evaluate the contributions of host galaxy properties that reflect the effects of binary neutron star merger rate.

5.1. The Stellar Mass Distribution of Short and Hybrid GRB Host Galaxies

Stellar mass is one of the major parameters expected to closely relate to the BNS merger rate. The stellar mass is the outcome of a galaxy's star formation history (SFH), which influences the formation rate of the progenitor system and the delay in its merging. In this context, comparing and analyzing the distributions of sGRB host galaxies and general field galaxies regarding their stellar mass is essential. By doing so, we can evaluate the differences as the contribution of the BNS merger rate.

If the binary neutron star (BNS) merger rate is directly proportional to the stellar mass of the host galaxy, as suggested by some theoretical studies (Mapelli et al. 2018), then the mass distribution of the host galaxies would follow a mass-weighted distribution. Under such a model, a $10^{10} M_{\odot}$ galaxy would exhibit a relative likelihood a hundred times greater of being identified as a sGRB host than a $10^8 M_{\odot}$ galaxy. Consequently, this would skew the frequency in the cumulative distribution towards more massive galaxies, deviating from the intrinsic distribution that typically follows the galaxy stellar mass function.

Figure 5 shows the following results. Compared to the volume-limited COSMOS field galaxies, which almost follow galaxy stellar mass function with the lower limit of $10^{7.9} M_{\odot}$, short and hybrid GRB host galaxies obviously lean toward a massive part of the distribution. However, they are not as massive as the mass-weighted distribution of the control sample, where the contribution of each galaxy is weighted by its stellar mass. This implies that the expected BNS merger rate in each galaxy is not directly proportional to its stellar mass.

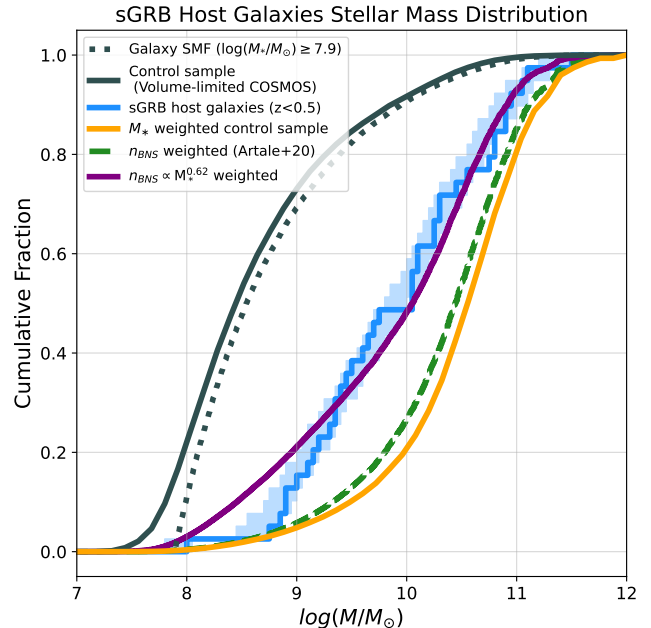


Figure 5. The cumulative distributions of stellar mass for short and hybrid GRB host galaxies compared with a volume-limited sample of galaxies in COSMOS field, applying various weighting schemes. The dotted gray line indicates the theoretical cumulative distribution of galaxies adhering to the stellar mass function for redshifts less than 0.5, with a stellar mass lower limit of $10^{7.9} M_{\odot}$ (Weaver et al. 2023). The continuous gray line tracks the cumulative distribution of a control sample galaxies. The blue stepped line represents the cumulative distribution for 39 GRB host galaxies with redshifts below 0.5, while the blue shaded region indicates the uncertainty range in stellar mass estimates. The orange line shows the cumulative distribution of the control sample, with each galaxy's contribution weighted by its stellar mass. The green long-dashed line illustrates the predicted host mass distribution based on the local BNS merger rate suggested by Artale et al. (2020). The purple line represents the control sample weighted by $M_*^{0.62}$, aimed at replicating the distribution pattern of the host galaxies.

Instead, if a weight of $M_*^{0.62}$ is applied to the control sample, it then appears similar to the observed mass distribution of the host galaxies. This is the result of finding the highest p-value returned when the exponent of the mass in the weight function was varied in 0.01 increments from 0 to 1 when the Kolmogorov-Smirnov (K-S) test was conducted with the host galaxies. As seen in these results, the environment of short and hybrid GRB occurrence has a weaker correlation with host stellar mass than a prediction of a linear relationship would suggest. Consequently, this implies the need to pay attention to low mass galaxies in BNS merger follow-up observations.

5.2. BNS Merger Rate Proxy

Given that host galaxy properties can potentially affect the BNS merger rate, it is plausible to consider an alternative form of the weight function. [Artale et al. \(2020\)](#) utilized hydrodynamic simulations and synthetic binary models to investigate the properties and cosmic evolution of BNS merger host galaxies. Their results suggest that host galaxies at $z > 1$ have active star formation activities, evolving through galaxy mergers during the long delay times of BNSs. In the local universe ($z = 0.1$), they predict that BNS merger host galaxies should be quiescent and massive. They propose a predictive formula for the local BNS merger rates as $\log(n_{\text{BNS}}/\text{Gyr}) = 0.800 \times \log(M_*/M_\odot) + 0.323 \times \log(\text{SFR}/M_\odot\text{yr}^{-1}) - 3.555$, emphasizing the importance of stellar mass for predicting BNS merger rates for a galaxy. To directly compare with their prediction and the observed properties of short and hybrid GRB host galaxies, we include the star formation rate as a parameter in our weight function.

One thing to consider is that those parameters are not mutually independent; for example, the relationship between stellar mass and SFR for star-forming galaxies is well established (e.g., [Davé 2008](#); [Mannucci et al. 2010](#)), a correlation also apparent in the left panel of Figure 6. Thus, to minimize the interdependencies between variables and clearly outline each term’s contribution, we have chosen to employ the specific SFR as the second parameter. Therefore, we aim to use Equation 2 as the predictive formula for the BNS merger rate and apply it as a weight function for the mass distribution.

$$\log(n_{\text{BNS}}/\text{Gyr}) = a \times \log(M_*) + b \times \log(\text{sSFR}/\text{yr}) + C \quad (2)$$

Assuming a certain set of coefficients (a, b) of this equation, we can weight the number count of each galaxy in control sample with its stellar mass and sSFR. The resulting weighted distribution can be compared to short and hybrid GRB host galaxy distribution using Kolmogorov-Smirnov (K-S) test (Figure 7).

To find the optimal set of (a, b), we can conduct a grid-searching method. Specifically, we perform the K-S test iteratively by varying the value of a from 0.2 to 1.4 and b from -0.2 to 1.0, with the step size of 0.01. The chosen parameter space encompasses the mass-prioritized prediction and includes generous variations to account for the contribution of the star formation rate. We confirmed that this range adequately covers the region around the maximum points and that there are no other local maxima beyond these bounds. This approach allows for a thorough investigation of the p-value for each

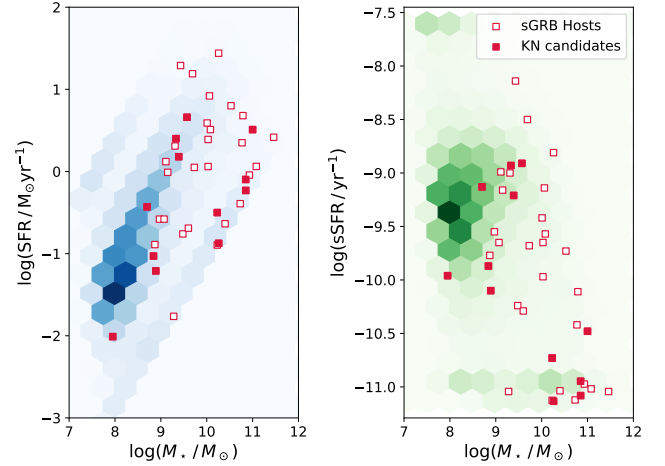


Figure 6. The host galaxies and field galaxies distribution in the M_* -SFR plane (**Left**) and M_* -sSFR plane (**Right**). In both diagrams, the hexagon bins in the background represent the distribution of volume-limited sample of galaxies in the COSMOS field. The lower limit of sSFR is set by Equation 1.

pair of (a, b). The result, shown in Figure 8, indicates the highest p-value at $(a, b) = (0.86^{+0.18}_{-0.18}, 0.44^{+0.34}_{-0.27})$. To estimate the error of the coefficients, we marginalized the p-value distribution to the a and b axes and measured the 1σ standard deviation. This suggests that $0.86 \times \log(M_*/M_\odot) + 0.44 \times \log(\text{sSFR}/\text{yr})$ can be a proxy for the BNS merger rate that reproduces the observed characteristics of short and hybrid GRB host galaxies.

To account for the effect of uncertainty in the stellar mass estimated from SED fitting, we performed random sampling 1,000 times using a skew-normal distribution estimated from the median and 1σ upper and lower limits represented in Table 2. The stellar mass distribution accounting for uncertainty is shown as the shaded region in Figure 7, representing the range from the 10th to the 90th percentile. After 1,000 Monte Carlo simulations, the median and standard deviation of the optimally estimated (a, b) were found to be $(0.83 \pm 0.07, 0.42 \pm 0.12)$. This result is well within the error range of the optimal coefficients estimated without considering the uncertainty.

5.3. Short and Hybrid GRB Host Galaxy Distribution on a Mass-sSFR Plane

In the previous section, we performed K-S tests on the one-dimensional stellar mass distribution. Since we consider the stellar mass and specific star formation rate (sSFR) as primary indicators for predicting the BNS merger rate, a more robust approach involves comparing host galaxies with the volume-limited COSMOS galaxies in a two-dimensional $M_* - \text{sSFR}$ plane.

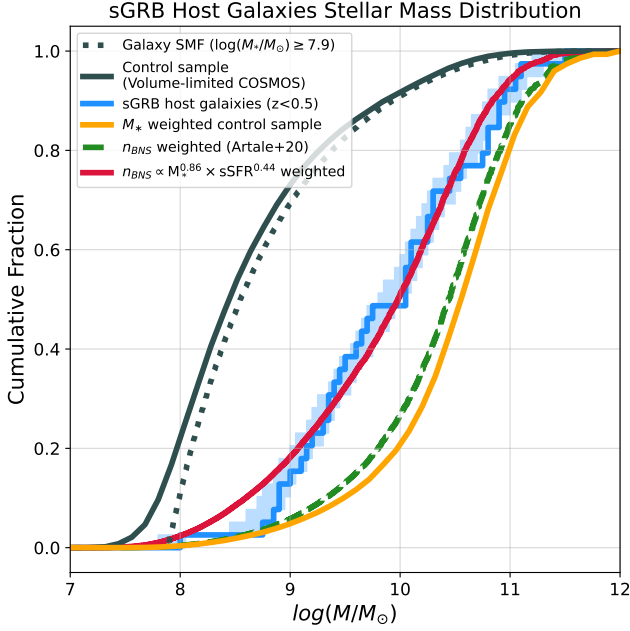


Figure 7. This figure presents the cumulative stellar mass distribution of short and hybrid GRB host galaxies akin to Figure 5. It highlights the weighted distribution (red line) that accounts for both stellar mass and sSFR (Equation 2), which optimally reproduces the observed distribution of short and hybrid GRB host galaxy stellar masses.

The K-S test is not suitable for comparing the two distributions in this case. Instead, we define a weight function corresponding to the form presented in Equation 2 to the distribution of control sample. To this end, we normalize both the weighted distribution and the distribution of short and hybrid GRB host galaxies. We then employ a χ^2 minimization technique to minimize a cost function, which is defined as the sum of the squares of the frequency differences in each bin. For this optimization, we utilize the `minimize` function from the `scipy.optimize` package.

A significant challenge in determining the optimized weight function on a two-dimensional plane arises from the limited number of short and hybrid GRB host galaxy samples. While the volume-limited COSMOS sample includes 35,122 objects for $z < 0.5$, there are only 39 identified short and hybrid GRB host galaxies. Consequently, the control samples exhibit an almost continuous distribution, whereas the host galaxies are sparsely distributed. This disparity complicates the direct comparison of the two distributions, as it is difficult to reproduce a distribution similar to that of short and hybrid GRBs with any assumed weight function. To mitigate this, we have used a sufficiently large bin size. By setting the bin size to 0.5 dex within the ranges of

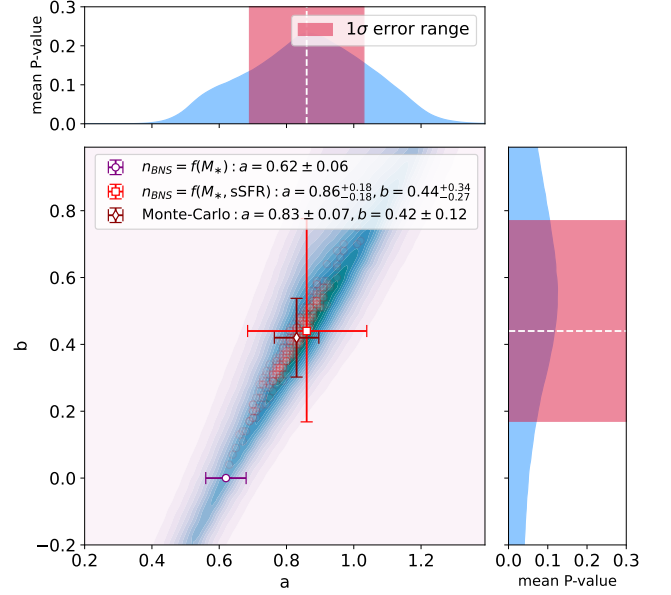


Figure 8. This figure displays the p-value distribution resulting from the K-S test comparing 39 short and hybrid GRB host galaxies to a volume-limited COSMOS galaxies at $z < 0.5$. The distribution is Gaussian smoothed at the 1σ level to explicate the trend. The purple circle marks the maximum p-value when the analysis is restricted solely to the stellar mass as the variable, while the red square represents the maximum p-value achieved when both stellar mass and sSFR are incorporated into the weighting function. The error bar for the red square delineate the standard deviations of the marginalized distributions along each axis. The semi-transparent red dots represent best-fit values of Monte-Carlo simulations, where each simulation accounts for the stellar mass errors of short and hybrid GRB host galaxies. The brown diamond indicates the median value of these best-fit values from the repetitions.

$7 < \log(M_*/M_\odot) < 12$, $-12 < \log(\text{sSFR}/\text{yr}) < -7$, we ensure that most bins containing main sequence galaxies have at least more than one count, demonstrating a nearly continuous distribution (Figure 9).

The use of a large bin size reduces the resolution of the distribution. If one assumes that such a coarse distribution accurately represents the true underlying distribution, χ^2 minimization could yield a weight function that closely aligns the two distributions with minimal errors. However, given the small sample size of the host galaxies, there is no assurance that a smoothed distribution based on this sample accurately reflects the broader population. This necessitates incorporating this uncertainty into our estimation of errors.

A practical method to address this is employing a statistical analysis of result variability via bootstrapping. We conducted 10,000 bootstrapping iterations, each randomly selecting 20-39 host galaxies to derive

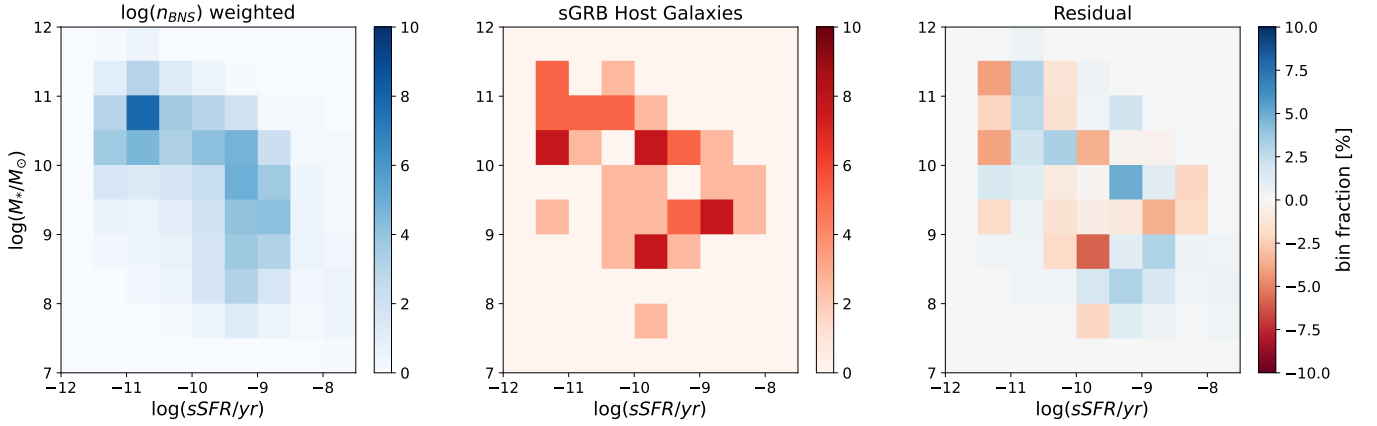


Figure 9. The normalized distributions of control sample and short and hybrid GRB host galaxies within the $\log(\text{sSFR}/\text{yr}) - \log(M_*/M_\odot)$ plane. The left panel illustrates the number density of volume-limited COSMOS sample, adjusted by the weight function of $\log(n_{\text{BNS}}/\text{Gyr}) = 0.67 \times \log(M_*/M_\odot) + 0.14 \times \log(\text{sSFR}/\text{yr}) + C$, which is determined to minimize the sum of squared residuals. The central panel depicts the distribution of short and hybrid GRB host galaxies, and the right panel shows the residual distribution after the optimization. The color scales have been normalized to represent the fraction of counts in each bin relative to the total sample size, allowing bin fractions to be interpreted as percentages.

the best-fit weight function. This sampling method allows for potential repetitions of the same galaxy within individual samples. The median and standard deviations from these iterations provided us with the optimal coefficients and their associated uncertainties, yielding $(a, b) = (0.67 \pm 0.14, 0.14 \pm 0.17)$. The robustness of our findings persisted even when the iteration count varied between 100 and 1000 or when the sample size was consistently set at 39. Consequently, these outcomes align with the previously estimated BNS merger rates, as shown in Figure 10. Although the orange and red points are marginally outside the 1σ error range, the background p-value distribution suggests that they lie on similar trends.

5.4. BNS Merger Rate Constant

Until now, we compared the short and hybrid GRB host distribution with the volume-limited COSMOS sample and determined the coefficients in the weight function (Equation 2). However, without considering the actual occurrence rate of binary neutron star mergers, we cannot determine the normalization constant C value.

There are previous works on the actual rate of BNS mergers. Among them, Rouco Escorial et al. (2023) corrected for the effect of the sGRB’s opening angle to estimate a beaming-corrected event rate of $R_{\text{true}} \approx 362 - 1789 \text{ Gpc}^{-3} \text{ yr}^{-1}$. The higher end of this range is based on the naturally narrow jet opening angles observed in sGRBs, while the lower end accounts for the potential of wider opening angles. This estimate falls within the range predicted for the BNS merger rate from the gravitational waves (Abbott et al. 2020a).

In the volume-limited COSMOS sample, if we assume that faint galaxies have a negligible contribution to the BNS merger rate, the sum of the expected $\log(n_{\text{BNS}}/\text{Gyr})$ for each galaxy should match the number of BNS mergers expected in the cosmic volume. After rejecting areas contaminated by bright stars, the effective area of the COSMOS field is 1.27 deg^2 , and the corresponding comoving volume is $8.747 \times 10^{-4} \text{ Gpc}^3$ ($z < 0.5$). Multiplying this by R_{true} gives us the expected BNS mergers in this volume per year.

By incorporating the optimal coefficients obtained in Section 5.2 (as shown in Figure 8), along with the values of $\log(M_*/M_\odot)$ and $\log(\text{sSFR}/\text{yr})$ for each galaxy in the volume-limited COSMOS sample, we can define the expected $\log(n_{\text{BNS}}/\text{Gyr})$ as a function of constant C :

$$\sum_i^k 10^{a \times \log(M_*)_i + b \times \log(\text{sSFR})_i + C} = R_{\text{true}} \times V_{z < 0.5} \quad (3)$$

Here, k denotes the total number of galaxies in the volume-limited sample, and $V_{z < 0.5}$ represents the comoving volume within $z = 0.5$ over the COSMOS survey field of view. We applied the `fsolve` function from the `scipy.optimize` library to solve Equation 3. The result is presented in the 4. Given our method of calculating R_{true} , the value of -0.177 can feasibly be interpreted as reflecting the BNS merger rate.

$$\begin{aligned} \log(n_{\text{BNS}}/\text{Gyr}) &= 0.86 \times \log(M_*/M_\odot) \\ &+ 0.44 \times \log(\text{sSFR}/\text{yr}) \\ &+ [0.163, 0.857] \end{aligned} \quad (4)$$

To validate this approach to estimate the C , we substituted the BNS merger rate coefficients at $z = 0.1$ from [Artale et al. \(2020\)](#) into the equation, yielding $\log(n_{\text{BNS}}/\text{Gyr}) = 0.800 \times \log(M_*/M_\odot) + 0.323 \times \log(\text{SFR}/M_\odot\text{yr}^{-1}) + [-3.625, -2.931]$. This range encompasses the constant value of -3.555 calculated in the original paper, thereby corroborating the efficacy of our methodology in determining the unit of the BNS merger rate.

6. DISCUSSION

In this section, we will discuss the results we have drawn in the previous section. In the subsection 6.1, we will discuss the stellar mass contribution for the merger rate expectation regarding the delay time distribution. In the subsections 6.2 and 6.3, the behaviors of host galaxies of KNe candidates subgroups and potential biases that could affect the sample and analyses will be discussed. Finally, we will mention other properties of galaxies that could be considered in future works 6.4.

6.1. Merger Rate Dependence on the Stellar Mass

From the mass distribution of short and hybrid GRB host galaxies, we have deduced that the BNS merger rate deviates from a scenario linearly proportional to stellar masses. Instead, our findings suggest that a combined weight function of stellar mass and sSFR more accurately replicates the observed mass distribution of short and hybrid GRB host galaxies.

Figure 8 displays the distribution of K-S test p-values for the comparison between the weighted distribution of galaxies and that of the host galaxies. The optimal coefficients were determined to be $(a, b) = (0.86^{+0.18}_{-0.18}, 0.44^{+0.34}_{-0.27})$. In contrast, the simulation results from [Artale et al. \(2020\)](#) estimated the local universe BNS merger rate (at $z = 0.1$) as $\log(n_{\text{BNS}}/\text{Gyr}) = 0.800 \times \log(M_*/M_\odot) + 0.323 \times \log(\text{SFR}/M_\odot\text{yr}^{-1}) - 3.555$. This equates to $(a, b) = (1.123, 0.323)$, significantly diverging from the error range of our results. This discrepancy highlights the pivotal role of star-forming galaxies, suggesting that stellar mass alone may be less influential in the context of predicting the BNS merger rate.

The significant contribution of star-forming galaxies to BNS merger host galaxies aligns with more recent simulation studies. [Mandhai et al. \(2022\)](#) predicted, using synthetic binary models and hydrodynamic simulations, that local BNS merger host galaxies will exhibit blue color and high star-forming activity. Similarly, [Chu et al. \(2022\)](#) emphasized the importance of stellar mass, SFR, and metallicity of host galaxies in determining the BNS merger rate, predicting that local host galaxies will be dominated by late-type galaxies. Studies such as [McCarthy et al. \(2020\)](#) and [Adhikari et al. \(2020\)](#), which

predict the characteristics of hosts based on various delay time models, also suggest that local host galaxies could be dominated by star-forming galaxies with BNS mergers with short delay times. However, for nearby host galaxies like NGC 4993, it is necessary to consider scenarios where the effects of galaxy evolution and progenitors with long delay times result in mergers occurring in massive galaxies.

If we disregard the sSFR component and fix the b coefficient to 0, the best-fit value of a becomes 0.62 ± 0.06 . This implies assuming $\log(n_{\text{BNS}}/\text{Gyr}) = 0.62 \times \log(M_*/M_\odot) + C$, and aligns with the conclusion that the significance of stellar mass should be considered to a lesser extent than 1. Compared to utilizing the merger rate function that incorporates both stellar mass and sSFR, considering only the stellar mass component diminishes the similarity to the short and hybrid GRB host galaxy distribution. Correspondingly, the p-value of the K-S test declines from 0.82 to 0.49, thereby reinforcing the necessity of including the sSFR in the second term of the analysis.

As the tendency between a and b depicted in Figure 10 implies, the more contribution we attribute to stellar mass, the more significant sSFR component should be in predicting the BNS merger rate. Therefore, compared to a merger rate prediction dominated by mass, incorporating sSFR regulates larger population of passive and massive galaxies, which typically exhibit negligible sSFR.

In actual follow-up observation scenarios, assigning linear weight to stellar mass could reduce observational

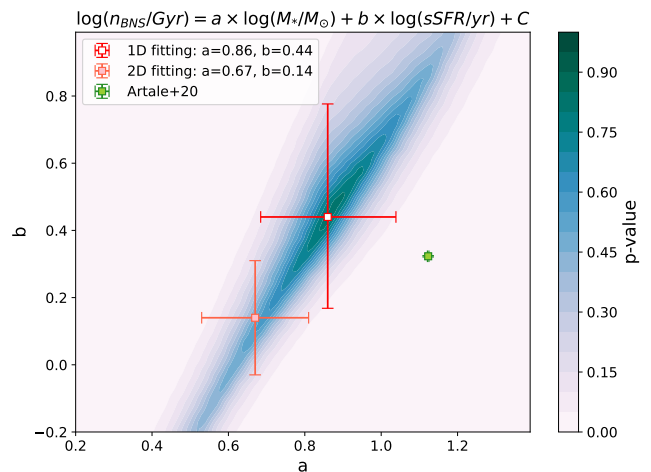


Figure 10. The comparisons of the BNS merger rate coefficients by overlaying the outcomes of Figure 9 and [Artale et al. \(2020\)](#) on the merger rate coefficient parameter space. Here, the optimized parameters a and b are defined in the relationship of $\log(n_{\text{BNS}}/\text{Gyr}) = a \times \log(M_*/M_\odot) + b \times \log(\text{sSFR}/\text{yr}) + C$.

efficiency. For example, if a $10^{11} M_{\odot}$ galaxy is located in a peripheral region with a lower volume probability, it might be assigned a higher priority because it can easily outweigh the combined mass of galaxies in other pointings. In contrast, using $M_*^{0.62}$ as a weight would likely yield results that more appropriately reflect the overall distribution of galaxies.

6.2. Host Galaxies of the Kilonova Candidates

One compelling piece of evidence in probing BNS mergers involves examining sGRBs that display a kilonova (KN) component. Their late-time infrared emission excess has been suggested as a sign of KNe. This phenomenon is attributed to the decay of opaque heavier elements that persist until late times (Kasen & Barnes 2019).

As detailed in Section 2.3, several GRBs have been observed to exhibit KN emissions in their afterglows. Referring to previous studies, we have identified the host galaxies of 12 KN candidates at $z < 0.5$. Analyzing the properties of these host galaxies enables a more direct assessment of the BNS merger environment.

Figure 11 presents the stellar mass distribution of the host galaxies of KN candidates. The distribution for the 12 KN candidates does not show a remarkable difference from that of other sGRB host galaxies. This similarity may suggest that short and hybrid GRB host galaxies are a representative sample of the BNS merger environment. The KN host galaxy’s mass distribution also underscores the importance of not overlooking low mass galaxies when studying BNS merger host galaxies.

However, it is important to note that the KN candidates mentioned here include not only typical sGRB afterglows but also hybrid GRBs (kilonova with long GRBs) like GRB 060614, GRB 060505, GRB 211211A, and GRB 211227A. These instances are hypothesized to be binary systems with neutron stars, but there is a possibility that they represent a unique group, such as binary mergers involving neutron stars and white dwarfs (Zhong et al. 2023).

When we exclude the hybrid GRBs and analyze the stellar mass distributions of the nine host galaxies where KNe were securely associated with sGRBs, the host galaxies appear marginally more massive, as shown in Figure 11. To address this effect, we assumed that the KN rate can be estimated as a function of stellar mass. We found that the optimal weight function is $M_*^{0.52}$ for KN candidates and hybrid GRB host galaxies, and $M_*^{0.70}$ when limited to the 8 KN candidate host galaxies. However, this difference is not statistically significant enough to support the null hypothesis that hybrid

GRBs and the rest of KNe are distinct populations, as evidenced by the K-S test result ($P_{KS} = 0.25$).

6.3. Potential Biases from Samples and Analyses

We explored the BNS merger environment by comparing 39 short and hybrid GRB host galaxies at $z < 0.5$ with a volume-limited sample from the COSMOS field galaxies. However, among the 39 host galaxies used, some have uncertain associations, raising the need to assess their impact on our results. Most samples with $P_{CC} > 0.10$ were excluded by selecting local samples, but four cases without afterglow detection (GRB 050906, GRB 070810B, GRB 080121, GRB 100216A) remain highly uncertain. These occurred near bright galaxies, and the bright galaxies were chosen as host candidates based on the low probability of random spatial overlap with the burst positions (Dichiara et al. 2020). If these cases are biased towards a certain part of the massive distribution, it might influence in our analysis.

Nonetheless, as illustrated in the upper panel of Figure 12, the stellar masses of host galaxies without afterglow detection are not biased towards a particular mass range. Upon excluding the afterglow non-detection cases and reapplying our grid searching method, the results (a, b)=(0.82, 0.39) remained similar. This indicates that the potential sample bias due to uncertain host associations is minimal for $z < 0.5$ short and hybrid GRB host galaxies.

A challenging aspect of sample bias in the local universe relates to hostless galaxies. Simulations by Mandhai et al. (2022) indicate that progenitors from low mass galaxies, due to weaker gravitational potentials, may more readily escape and produce fainter afterglows. This makes such galaxies less likely to be observed as sGRB host galaxies. Predictions suggest that hostless events might comprise approximately 16-35% of BNS mergers.

Recently, Nugent et al. (2023) posits that a significant portion of high-redshift sGRB host galaxies belong to a dwarf host population. This finding may imply that our observed host properties could be biased towards brighter galaxies, differing from the actual BNS merger environments. However, to fully trust this argument, one must also consider that sGRB events connected to faint galaxies are very rare in the local universe. In our sample, the only confirmed faint host galaxy is that of GRB 060614, identified as a hybrid LGRB event. Given this, we conclude that current evidence is insufficient to ascertain the contribution of hostless or faint galaxies to the true BNS merger environment.

On the other hand, the range of parameters we used in the equation may have caused differences in the form

KN Candidate Host Galaxies Stellar Mass Distribution

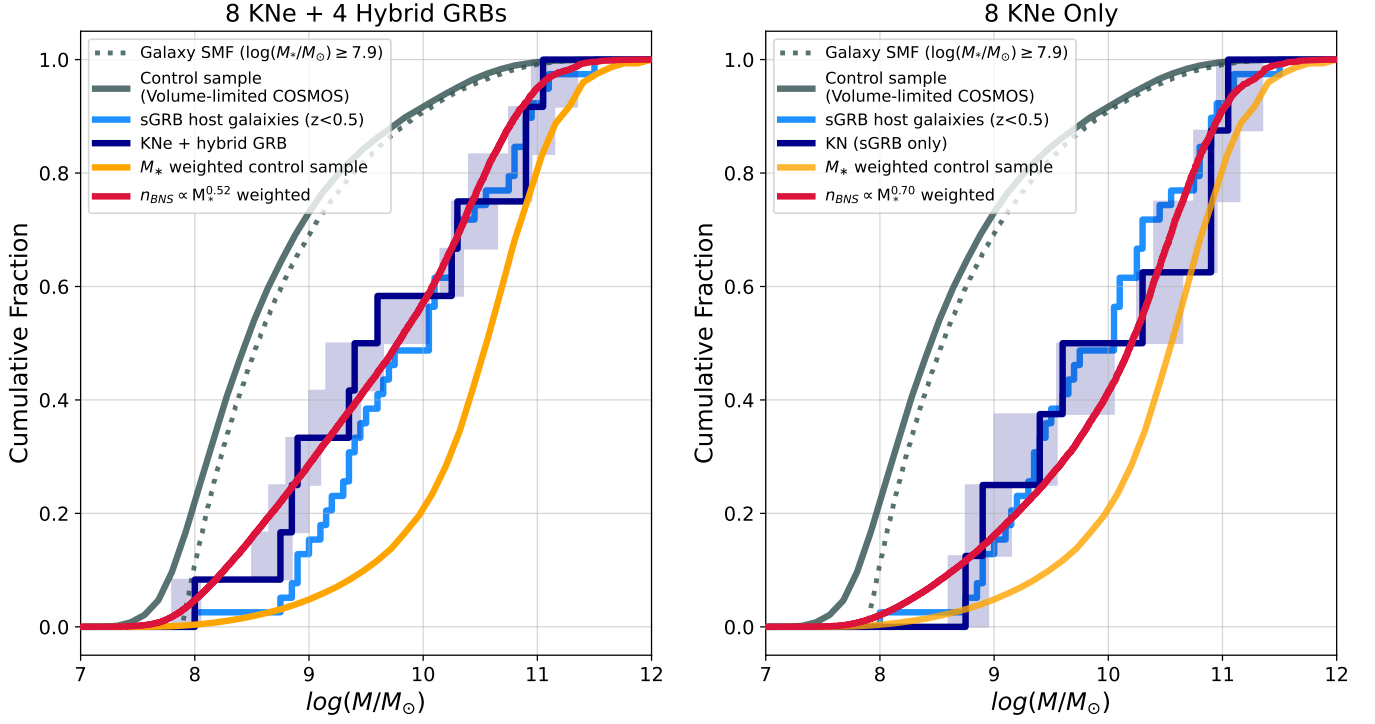


Figure 11. (Left) The stellar mass cumulative distribution, similar to Figure 7 but specifically limited to kilonova candidates host galaxies. The navy line represents the mass distribution of 12 kilonova host galaxies, and the shaded region indicates the uncertainty range in stellar mass estimates. The red line indicates the distribution of control sample weighted by $\log(n_{\text{BNS}}/\text{Gyr}) = 0.52 \times \log(M_*/M_\odot) + C$, optimally reproducing the observed kilonova host distribution. (Right) The solid navy line illustrates the mass distribution when excluding four additional events associated with long GRBs, and the corresponding optimally reproduced weighted distribution is denoted by the red line. For this case, the optimal weight function is determined as $\log(n_{\text{BNS}}/\text{Gyr}) = 0.70 \times \log(M_*/M_\odot) + C$, suggesting more massive distribution compared to the rest of sGRB host galaxies.

of the equation. We set a lower limit for sSFR estimated from SED fitting because it is not physically meaningful to analyze the SFR of quiescent galaxies with values close to 0. Among various criteria for classifying quiescent galaxies, we used Equation 1. This is similar to setting a lower limit of sSFR to about 10^{-11}yr^{-1} , and it is also similar to the *NUVrJ* color-color selection used by Weaver et al. (2023).

However, the definition of a passive galaxy can sometimes vary, being set as $\text{sSFR} > 1/[3 \times t(z)]$ or $> 1/t(z)$, similar to establishing a lower sSFR limit of $10^{-10.5}\text{yr}^{-1}$ or 10^{-10}yr^{-1} , respectively. When the sSFR lower limit is defined as $1/[3 \times t(z)]$, the best-fit coefficients are calculated to be $(a, b) = (0.92^{+0.09}_{-0.24}, 0.62^{+0.19}_{-0.44})$. This shift suggests that as the sSFR cut for quiescent galaxies is assumed to be higher, the value of the coefficient b also shifts upwards. Consequently, this highlights the importance of retaining the definition of passive galaxies and their parameters to appropriately apply the resulting equation.

Finally, the definition of the control sample can also influence the results. To ensure completeness down to $\log(M_*/M_\odot) = 7.9$, we set the absolute magnitude cut at $M_r < -16.22$ mag. If we lower this threshold to $M_r < -14$ mag to include fainter galaxies, the control sample would expand from 35,122 to 77,434 galaxies. In this scenario, the best-fit coefficients change to approximately $(a, b) = (0.95^{+0.15}_{-0.16}, 0.56^{+0.33}_{-0.24})$. This change reflects the inclusion of more galaxies with lower mass and sSFR values, thus assigning a higher weight to them. However, the ratio between a and b remains nearly constant while varying M_r cut, suggesting that from a prioritization perspective, the outcome is maintained.

6.4. Other Host Galaxy Parameters

Our analysis primarily focuses on host galaxies' stellar mass and sSFR to inspect the BNS merger environment. However, we should acknowledge that other properties could also affect the predicted merger rate.

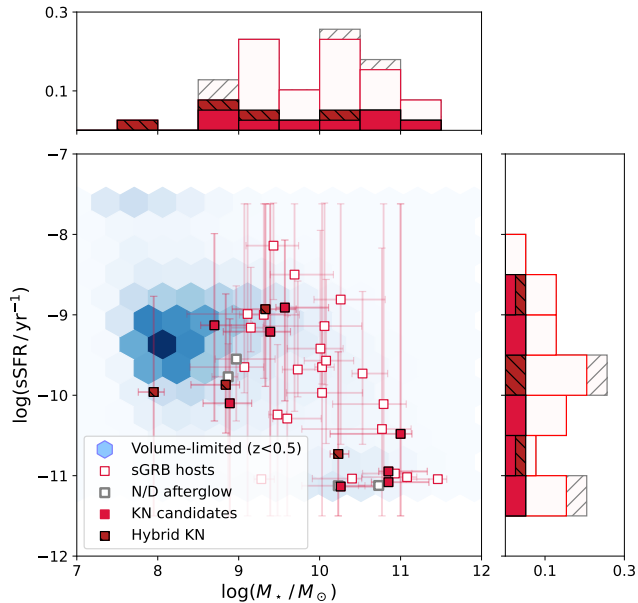


Figure 12. The distribution of 39 short and hybrid GRB host galaxies in the $\log(M_*/M_\odot) - \log(\text{sSFR}/\text{yr}^{-1})$ plane. The blue hexagon bin in the background represents the distribution of volume-limited COSMOS sample with $z < 0.5$. Red-filled points denote instances where kilonova emission features were observed, with hybrid GRBs that occurred alongside LGRBs distinctly marked with hatching. The samples outlined in gray are 4 samples suggested by [Dichiara et al. \(2020\)](#), without detection of afterglow emissions, thus marking them as highly uncertain. The histograms along each axis represent the distributions of stellar mass and sSFR for the sample without afterglow detections or the one that is only specifically limited to cases showing kilonova features. Each of the distributions shows no statistically significant difference from the overall sample.

One such factor is the age of the stellar population. Galaxies harboring older stars are anticipated to exhibit a reduced merger rate, a trend influenced by the delay time distribution (DTD) effect. However, as we presented in Figure 2, stellar population age is not a well-constrained parameter.

Simulation studies, such as those conducted by [Mapelli et al. \(2018\)](#), [Artale et al. \(2020\)](#) and [Chu et al. \(2022\)](#), have underscored the role of host metallicity in progenitor formation, indicating a likely positive correlation with the BNS merger rate. This correlation arises because the metallicity influences the initial mass of the compact binary progenitor systems.

Estimating galaxy parameters through the SED fitting is challenging with the currently limited broad-band photometry information for some of our datasets and the SED fitting model. The metallicity resolution is constrained to just four distinct levels in the stellar pop-

ulation library by [Bruzual & Charlot \(2003\)](#) employed for the SED fitting. Furthermore, there is a degeneracy among the stellar age, the metallicity, and the reddening. For example, the impact of aging is approximately 1.5 times the effect induced by metal abundance ([Worthey 1994](#)).

Future investigations, with additional photometry datasets and spectroscopic data containing emission and absorption line measurements, should facilitate the estimation of galaxy parameters.

6.5. Application of Our Results to Studies of GW Events and Other Transients

Our findings offer practical guidelines for follow-up observations of gravitational wave events. Our result suggests that GW event follow-up observation can be efficiently prioritized if both mass and star formation are considered. Assuming the BNS merger rate follows $M_*^{0.62}$ instead of being directly proportional to stellar mass, the effects are as follows. We would need to observe a larger number of galaxies to cover the same amount of probability, and we would be more strongly affected by bias due to the incompleteness of the reference catalog. Nevertheless, we need to take into account the observational evidence that significant fraction of sGRBs and KN-like emissions is found in star-forming galaxies. Our results provide quantitative guidelines for tiling or targeting observations for gravitational wave follow-up, and are practical for developing observation strategies and systematically utilizing facilities. For example, our BNS merger rate prescription can be applied each galaxy in the GW localization area. Then, the galaxies can be sorted in order of decreasing merger rate for more efficient galaxy-target observation (e.g., [Paek et al. \(2024\)](#)). Future observations of the EM-producing GW events should tell whether our BNS merger rate estimator is superior to BNS merger rate estimators based on stellar mass only.

The methodology employed in this study to assess host galaxy candidates within the GW probable volume can be applied retroactively. For instance, by weighting the probabilities of galaxies within the localization volumes using our BNS merger rate prescription, we can estimate host galaxy distance distributions for these gravitational wave events. Accumulated data from such cases could lead to statistical analyses of cosmological parameters in future research.

This approach is also applicable to predicting other types of transients. Studies that estimate transient rates by measuring how host galaxy properties deviate from those of general galaxies have been actively conducted for supernovae. Recently, [Liang et al. \(2024\)](#) analyzed

the stellar mass function of host galaxies and found that for core-collapse supernovae, weighting by SFR is crucial, while for type Ia supernovae, both SFR and stellar mass need to be considered. When studying recently discovered transients (e.g., GRBs, tidal disruption events and fast radio bursts), our approach of comparing galaxy properties within volume-limited samples will be effective for probing their uncertain progenitor systems and defining the characteristics of their host galaxies.

7. CONCLUSION

In this study, we studied the galactic environment where BNS mergers occur, focusing on the host galaxies of short and hybrid GRBs. We compiled a dataset of the GRB host galaxies, gathering multi-wavelength broadband photometry and spectroscopic redshift data from previous studies and archival images. This data set was utilized for the SED fitting to deduce the properties of the host galaxies.

Our analysis was confined to 39 host galaxies at $z < 0.5$. We compared these with a volume-limited sample from galaxies in the COSMOS field, achieving a complete dataset down to $10^{7.9}M_{\odot}$ at $z < 0.5$. Figure 7 reveals that the stellar mass distribution of short and hybrid GRB host galaxies deviates from the volume-limited COSMOS sample, where the number count is weighted by each galaxy’s stellar mass. This would not be true if the BNS merger rate were proportional to the host galaxy stellar mass. Instead, we found that the BNS merger rates, which successfully reproduce the observed distribution of host galaxies, can be

expressed by the following equation: $\log(n_{\text{BNS}}/\text{Gyr}) = 0.86 \times \log(M_*/M_{\odot}) + 0.44 \times \log(\text{sSFR}/\text{yr}) + 0.857$.

Dividing the short and hybrid GRB sample into several subsamples does not affect the conclusion. The stellar mass distributions of sGRBs with ambiguous host associations are consistent with those of sGRBs with clearer host identifications. Additionally, events exhibiting kilonova signatures show host characteristics similar to those of other sGRB host galaxies. Excluding hybrid GRB events from the kilonova signature sample resulted in a marginally more massive host distribution, but not enough to draw definitive conclusions.

With the expected improvements in GW detection technologies, more GW events will be discovered in future that would be accompanied by KNe. Our results on the BNS merger rate estimator can serve as an important element for designing efficient search methods to find optical counterparts of GW events from BNS mergers and eventually help promote multi-messenger astronomy involving GW. Our methodology of estimating the merger rate can be applied to host galaxies of other types of transients such as FRBs to understand the environment of such transients.

- 1 We express our gratitude to the anonymous referee
- 2 for their valuable comments and suggestions that sig-
- 3 nificantly improved the manuscript. We also thank
- 4 Donggeun Tak for proofreading our paper and provid-
- 5 ing insightful feedback. This work was supported by the
- 6 National Research Foundation of Korea (NRF) grants,
- 7 No. 2020R1A2C3011091 and No. 2021M3F7A1084525,
- 8 funded by the Korean government (MSIT).

APPENDIX

Table A1. Photometric data for short and hybrid GRB host galaxies

Target	RA	Dec	redshift	Instrument	Filter	ABmag	Reference ^a
GRB050509B	12:36:12.87	28:58:58.84	0.225	SDSS	u	20.32±0.13	Leibler & Berger (2010)
				PS1	g	18.41±0.07	Chambers et al. (2016)*
				PS1	r	17.30±0.07	Chambers et al. (2016)*
				PS1	i	16.80±0.08	Chambers et al. (2016)*
				PS1	z	16.53±0.06	Chambers et al. (2016)*
				PS1	y	16.41±0.16	Chambers et al. (2016)*
				2MASS	J	16.16±0.14	Leibler & Berger (2010)
				2MASS	H	15.84±0.18	Leibler & Berger (2010)
				2MASS	K	15.98±0.16	Leibler & Berger (2010)

Continued on next page

Target	RA	Dec	redshift	Instrument	Filter	ABmag	Reference ^a
GRB050709	23:01:26.76	-38:58:40.42	0.161	HST/WFPC2	F450W	22.44±0.05	Fong et al. (2010)*
				DECaLS	g	22.10±0.10	Dey et al. (2019)*
				ACS/WFC	F814W	21.25±0.09	Fox et al. (2005)*
				DECaLS	z	21.22±0.12	Dey et al. (2019)*
				Magellan/PANIC	J	20.76±0.08	Leibler & Berger (2010)
				Magellan/PANIC	K	21.04±0.16	Leibler & Berger (2010)
GRB050724	16:24:44.41	-27:32:26.39	0.254	PS1	g	19.62±0.12	Chambers et al. (2016)*
				PS1	r	18.81±0.05	Chambers et al. (2016)*
				PS1	i	18.36±0.05	Chambers et al. (2016)*
				PS1	z	18.09±0.06	Chambers et al. (2016)*
				PS1	y	17.95±0.08	Chambers et al. (2016)*
				3.6TNG/NICS	J	17.28±0.04	Gorosabel et al. (2006)
				3.6TNG/NICS	H	16.89±0.05	Gorosabel et al. (2006)
				3.6TNG/NICS	K	16.59±0.05	Gorosabel et al. (2006)
				WISE	W1	18.05±0.05	Klose et al. (2019)
				WISE	W2	18.75±0.13	Klose et al. (2019)
GRB050813	16:07:57.20	11:14:53.09	0.719	DECaLS	g	25.02±0.59	Dey et al. (2019)*
				DECaLS	r	22.96±0.14	Dey et al. (2019)*
				PS1	i	22.36±0.16	Chambers et al. (2016)*
				DECaLS	z	21.89±0.13	Dey et al. (2019)*
GRB050906	03:31:11.16	-14:38:18.76	0.0308	GMOS-N	R	23.45±0.07	Prochaska et al. (2006)
				DECam	g	14.18±0.03	Abbott et al. (2021c)*
				DECam	r	13.78±0.03	Abbott et al. (2021c)*
				DECam	i	13.65±0.03	Abbott et al. (2021c)*
				DECam	z	13.47±0.03	Abbott et al. (2021c)*
				DECam	Y	13.36±0.03	Abbott et al. (2021c)*
				2MASS	J	13.39±0.02	Levan et al. (2008)
				2MASS	H	13.03±0.05	Levan et al. (2008)
GRB051210	22:00:40.94	-57:36:47.06	0.681 ^{+0.27} _{-0.34}	Magellan/LDSS	g	24.29±0.34	Leibler & Berger (2010)
				Magellan/LDSS	r	24.04±0.15	Leibler & Berger (2010)
				DECam	i	23.74±0.19	Abbott et al. (2021c)*
				Magellan/LDSS	z	24.06±0.21	Leibler & Berger (2010)
				Magellan/PANIC	K	>20.91	Leibler & Berger (2010)
				HST/WFPC2	F675W	23.70±0.05	Fong et al. (2010)
GRB051221A	21:54:48.65	16:53:27.34	0.546	DECaLS	g	23.42±0.12	Dey et al. (2019)*
				DECaLS	r	22.67±0.09	Dey et al. (2019)*
				PS1	i	22.39±0.18	Chambers et al. (2016)*
				ACS/WFPC2	F814W	22.29±0.02	HST 10917 (PI: D. Fox)*
				DECaLS	z	22.02±0.11	Dey et al. (2019)*
				Magellan/PANIC	J	22.01±0.20	Leibler & Berger (2010)
GRB060502B	18:35:45.75	52:37:36.25	0.287	Magellan/PANIC	K	22.30±0.15	Leibler & Berger (2010)
				PS1	g	20.19±0.06	Chambers et al. (2016)*
				PS1	r	18.95±0.04	Chambers et al. (2016)*
				PS1	i	18.51±0.05	Chambers et al. (2016)*
				PS1	z	18.23±0.06	Chambers et al. (2016)*
				PS1	y	17.91±0.08	Chambers et al. (2016)*

Continued on next page

Target	RA	Dec	redshift	Instrument	Filter	ABmag	Reference ^a
GRB060505	22:07:03.47	-27:48:55.47	0.0894	UKIRT/WFCAM	J	17.65±0.06	Dye et al. (2018)
				WISE	W1	17.99±0.03	Klose et al. (2019)
				WISE	W2	18.28±0.04	Klose et al. (2019)
				GALEX	FUV	19.74±0.13	Martin et al. (2005)
				GALEX	NUV	19.48±0.09	Martin et al. (2005)
				PS1	g	18.33±0.04	Chambers et al. (2016)*
				PS1	r	18.05±0.04	Chambers et al. (2016)*
				PS1	i	17.82±0.04	Chambers et al. (2016)*
				PS1	z	17.92±0.05	Chambers et al. (2016)*
				PS1	y	17.58±0.07	Chambers et al. (2016)*
GRB060614	21:23:32.10	-53:01:36.44	0.125	WISE	W1	18.42±0.05	Wright et al. (2010)
				WISE	W2	18.83±0.11	Wright et al. (2010)
				Swift/UVOT	u	24.57±0.31	Savaglio et al. (2009)
				DECam	g	23.07±0.05	Abbott et al. (2021c)*
				DECam	r	22.60±0.05	Abbott et al. (2021c)*
				DECam	i	22.40±0.07	Abbott et al. (2021c)*
GRB060801	14:12:01.26	16:58:55.97	1.13	HST/ACS	F814W	22.45±0.01	Kenno et al. (2006)*
				DECam	z	22.11±0.09	Abbott et al. (2021c)*
				GMOS-N	g	23.44±0.09	Leibler & Berger (2010)
				GMOS-N	r	23.20±0.11	Leibler & Berger (2010)
GRB061006	07:24:07.80	-79:11:55.19	0.461	GMOS-N	i	23.05±0.19	Leibler & Berger (2010)
				GMOS-N	z	22.88±0.10	Leibler & Berger (2010)
				Magellan/PANIC	J	>21.52	Leibler & Berger (2010)
				Magellan/PANIC	K	>19.91	Leibler & Berger (2010)
				VLT/FORS2	B	25.75±0.12	D'Avanzo et al. (2009)
				VLT/FORS1	V	24.56±0.07	D'Avanzo et al. (2009)
				Magellan/LDSS	r	24.15±0.09	Leibler & Berger (2010)
				HST/ACS	F814W	23.02±0.03	Gal-Yam et al. (2006)*
				Magellan/LDSS	z	23.28±0.25	Leibler & Berger (2010)
				VLT/ISAAC	J	22.91±0.20	D'Avanzo et al. (2009)
GRB061210	09:38:05.36	15:37:18.88	0.41	Magellan/PANIC	K	22.60±0.25	Leibler & Berger (2010)
				Magellan/LDSS	g	23.28±0.10	Leibler & Berger (2010)
				PS1	r	21.71±0.13	Chambers et al. (2016)*
				PS1	i	21.48±0.14	Chambers et al. (2016)*
				Magellan/LDSS	z	21.32±0.14	Leibler & Berger (2010)
GRB070429B	21:52:03.69	-38:49:42.82	0.902	Magellan/PANIC	J	21.32±0.15	Leibler & Berger (2010)
				Magellan/PANIC	K	20.33±0.10	Leibler & Berger (2010)
				Magellan/LDSS	g	24.40±0.20	Leibler & Berger (2010)
				Magellan/LDSS	r	23.28±0.04	Leibler & Berger (2010)
				Magellan/LDSS	i	21.89±0.09	Leibler & Berger (2010)
				Magellan/LDSS	z	21.76±0.12	Leibler & Berger (2010)
				WFC3/IR	F160W	20.59±0.03	Fong & Berger (2013)
				WISE	W1	20.08±0.15	Klose et al. (2019)
GRB070714B	03:51:22.27	28:17:50.94	0.923	WISE	W2	>20.02	Klose et al. (2019)
				WFC3/UVIS	F475W	25.36±0.06	Fong & Berger (2013)
				GMOS-N	r	24.89±0.22	Graham et al. (2009)
				GMOS-N	i	23.97±0.13	Graham et al. (2009)

Continued on next page

Target	RA	Dec	redshift	Instrument	Filter	ABmag	Reference ^a
GRB070724	01:51:14.06	-18:35:38.47	0.457	GMOS-N	z	23.98±0.13	Graham et al. (2009)
				Gemini/NIRI	J	23.18±0.12	Graham et al. (2009)
				Gemini/NIRI	K	23.02±0.13	Graham et al. (2009)
				WFC3/IR	F160W	23.06±0.02	Fong & Berger (2013)
				DECam	g	21.64±0.07	Abbott et al. (2021c)*
				DECam	r	20.72±0.05	Abbott et al. (2021c)*
				DECam	i	20.48±0.05	Abbott et al. (2021c)*
				DECam	z	20.27±0.05	Abbott et al. (2021c)*
				DECam	Y	20.17±0.11	Abbott et al. (2021c)*
				Magellan/PANIC	J	20.02±0.02	Leibler & Berger (2010)
GRB070729	03:45:15.80	-39:19:18.59	0.761 ^{+0.08} _{-0.08}	WFC3/IR	F160W	19.89±0.02	Fong & Berger (2013)
				Magellan/PANIC	H	19.79±0.02	Leibler & Berger (2010)
				Magellan/PANIC	K	19.71±0.04	Leibler & Berger (2010)
				WISE	W1	19.73±0.11	Klose et al. (2019)
				WISE	W2	19.71±0.22	Klose et al. (2019)
				DECam	g	24.23±0.21	Abbott et al. (2021c)*
				DECam	r	22.94±0.09	Abbott et al. (2021c)*
				DECam	i	21.85±0.06	Abbott et al. (2021c)*
				DECam	z	21.60±0.10	Abbott et al. (2021c)*
				Magellan/PANIC	J	22.68±0.18	Fong et al. (2022)
GRB070809	13:35:04.18	-22:08:33.01	0.473	Magellan/PANIC	K	22.77±0.37	Fong et al. (2022)
				WISE	W1	19.24±0.05	Klose et al. (2019)
				WISE	W2	20.03±0.18	Klose et al. (2019)
				Magellan/LDSS3	g	22.15±0.05	Leibler & Berger (2010)
				HST/ACS	F606W	20.47±0.03	Fong & Berger (2013)
				Magellan/LDSS3	r	20.14±0.02	Leibler & Berger (2010)
				Magellan/LDSS3	i	19.46±0.05	Leibler & Berger (2010)
				WFC3/IR	F160W	18.22±0.01	Fong & Berger (2013)
				Magellan/PANIC	K	17.99±0.04	Leibler & Berger (2010)
				GRB070810B	00:35:53.43	08:49:27.49	0.0385
GALEX	NUV	20.53±0.06	Dichiara et al. (2020)				
SDSS	u	17.31±0.02	Alam et al. (2015)				
SDSS	g	15.47±0.01	Alam et al. (2015)				
SDSS	r	14.66±0.01	Alam et al. (2015)				
SDSS	i	14.27±0.01	Alam et al. (2015)				
SDSS	z	13.93±0.01	Alam et al. (2015)				
UKIRT/WFCAM	Y	14.10±0.01	Lawrence et al. (2007)				
UKIRT/WFCAM	H	13.62±0.01	Lawrence et al. (2007)				
UKIRT/WFCAM	K	13.82±0.01	Lawrence et al. (2007)				
GRB071227	03:52:31.03	-55:59:00.89	0.381	WISE	W1	14.78±0.02	Dichiara et al. (2020)
				WISE	W2	15.46±0.03	Dichiara et al. (2020)
				WFC3/UVIS	F438W	22.35±0.05	Fong & Berger (2013)
				DECam	g	22.12±0.04	Abbott et al. (2021c)*
				DECam	r	20.72±0.03	Abbott et al. (2021c)*
				DECam	i	20.18±0.03	Abbott et al. (2021c)*
				DECam	z	19.80±0.04	Abbott et al. (2021c)*
DECam	Y	19.73±0.07	Abbott et al. (2021c)*				

Continued on next page

Target	RA	Dec	redshift	Instrument	Filter	ABmag	Reference ^a
GRB080121	09:08:58.15	41:49:26.50	0.045	Magellan/PANIC	J	19.17±0.06	Leibler & Berger (2010)
				WFC3/IR	F160W	18.73±0.01	Fong & Berger (2013)
				Magellan/PANIC	K	18.16±0.06	Leibler & Berger (2010)
				WISE	W1	18.28±0.03	Klose et al. (2019)
				WISE	W2	18.49±0.05	Klose et al. (2019)
				GALEX	FUV	19.73±0.12	Dichiara et al. (2020)
				GALEX	NUV	19.41±0.06	Dichiara et al. (2020)
				PS1	g	17.94±0.06	Chambers et al. (2016)*
				PS1	r	17.68±0.05	Chambers et al. (2016)*
				PS1	i	17.45±0.06	Chambers et al. (2016)*
				PS1	z	17.31±0.07	Chambers et al. (2016)*
GRB080123	22:35:46.94	-64:53:54.97	0.495	WISE	W1	18.94±0.05	Dichiara et al. (2020)
				WISE	W2	19.43±0.15	Dichiara et al. (2020)
				DECam	g	22.05±0.06	Abbott et al. (2021c)*
				DECam	r	21.04±0.04	Abbott et al. (2021c)*
				DECam	i	20.66±0.05	Abbott et al. (2021c)*
				DECam	z	20.53±0.07	Abbott et al. (2021c)*
GRB090510	22:14:12.62	-26:34:58.55	0.903	DECam	Y	20.26±0.12	Abbott et al. (2021c)*
				Magellan/PANIC	J	20.32±0.05	Leibler & Berger (2010)
				Magellan/PANIC	K	19.59±0.06	Leibler & Berger (2010)
				Magellan/LDSS	g	23.86±0.08	Leibler & Berger (2010)
				Magellan/LDSS	i	22.45±0.14	Leibler & Berger (2010)
				Magellan/LDSS	z	22.69±0.17	Leibler & Berger (2010)
				Magellan/PANIC	J	21.81±0.15	Leibler & Berger (2010)
				WFC3/IR	F160W	21.79±0.01	Fong & Berger (2013)
				Magellan/PANIC	K	21.98±0.35	Leibler & Berger (2010)
				GRB090515	10:56:35.85	14:26:42.84	0.403
GMOS-N	r	20.27±0.05	Leibler & Berger (2010)				
GMOS-N	i	19.49±0.05	Leibler & Berger (2010)				
Magellan/PANIC	J	18.69±0.05	Leibler & Berger (2010)				
Magellan/PANIC	K	18.24±0.05	Leibler & Berger (2010)				
GRB100117A	00:45:04.66	-01:35:42.02	0.914				
				GMOS-N	g	26.17±0.30	Fong et al. (2011)
				Magellan/IMACS	r	24.33±0.10	Fong et al. (2011)
				Magellan/IMACS	i	22.85±0.10	Fong et al. (2011)
				Magellan/IMACS	z	22.33±0.10	Fong et al. (2011)
				Gemini/NIRI	J	21.87±0.25	Fong et al. (2011)
				WFC3/IR	F160W	21.37±0.04	Fong & Berger (2013)
				Gemini/NIRI	H	21.26±0.21	Fong et al. (2011)
				Gemini/NIRI	K	21.24±0.20	Fong et al. (2011)
GRB100206A	03:08:39.14	13:09:29.34	0.407	Keck/LRIS	g	22.33±0.17	Perley et al. (2012)
				Keck/LRIS	R	20.55±0.09	Perley et al. (2012)
				GMOS-N	i	20.09±0.08	Perley et al. (2012)
				GMOS-N	z	19.64±0.05	Perley et al. (2012)
				PAIRITEL	J	19.06±0.12	Perley et al. (2012)
				PAIRITEL	H	18.41±0.09	Perley et al. (2012)
				PAIRITEL	K	18.03±0.11	Perley et al. (2012)

Continued on next page

Target	RA	Dec	redshift	Instrument	Filter	ABmag	Reference ^a				
GRB100216A	10:17:00.26	35:31:18.92	0.038	WISE	W1	18.41±0.05	Klose et al. (2019)				
				WISE	W2	18.49±0.10	Klose et al. (2019)				
				GALEX	FUV	18.82±0.11	Dichiara et al. (2020)				
				GALEX	NUV	18.61±0.08	Dichiara et al. (2020)				
				PS1	g	17.01±0.12	Chambers et al. (2016)*				
				PS1	r	16.71±0.07	Chambers et al. (2016)*				
				PS1	i	16.49±0.05	Chambers et al. (2016)*				
				PS1	z	16.47±0.06	Chambers et al. (2016)*				
				PS1	y	16.32±0.09	Chambers et al. (2016)*				
GRB100625A	01:03:10.92	-39:05:18.44	0.452	UKIRT/WFCAM	J	16.60±0.04	Dye et al. (2018)				
				WISE	W1	18.03±0.04	Dichiara et al. (2020)				
				WISE	W2	18.57±0.09	Dichiara et al. (2020)				
				DECam	g	24.09±0.13	Abbott et al. (2021c)*				
				DECam	r	22.61±0.05	Abbott et al. (2021c)*				
				DECam	i	22.05±0.06	Abbott et al. (2021c)*				
				DECam	z	21.95±0.09	Abbott et al. (2021c)*				
				DECam	Y	21.46±0.16	Abbott et al. (2021c)*				
				Magellan/PANIC	J	21.40±0.06	Fong & Berger (2013)				
GRB100816A	23:26:57.54	26:34:41.34	0.805	Magellan/FourStar	K	20.76±0.10	Fong & Berger (2013)				
				DECaLS	g	23.16±0.11	Dey et al. (2019)				
				DECaLS	r	21.89±0.06	Dey et al. (2019)				
				PS1	i	21.60±0.11	Chambers et al. (2016)				
				DECaLS	z	21.05±0.07	Dey et al. (2019)				
				HST/WFC3	F160W	20.24±0.03	HST 12502 (PI: Fruchter)*				
				WISE	W1	19.78±0.12	Klose et al. (2019)				
				WISE	W2	20.21±0.36	Klose et al. (2019)				
				GRB101219A	04:58:20.50	-02:32:22.45	0.718	Magellan/LDSS3	g	24.57±0.08	Fong & Berger (2013)
GMOS-S	r	23.95±0.05	Fong & Berger (2013)								
GMOS-S	i	23.19±0.08	Fong & Berger (2013)								
Magellan/LDSS3	z	23.22±0.16	Fong & Berger (2013)								
Magellan/FourStar	J	22.11±0.19	Fong & Berger (2013)								
Magellan/FourStar	K	21.55±0.21	Fong & Berger (2013)								
GRB101224A	19:03:41.92	45:42:48.86	0.454					MMT/MMTCam	g	22.66±0.07	Fong et al. (2022)
								LBT/LBC	r	22.07±0.05	Fong et al. (2022)
								LBT/LBC	i	21.61±0.05	Fong et al. (2022)
				LBT/MODS	z	21.72±0.09	Fong et al. (2022)				
				MMT/MMIRS	Y	21.79±0.18	Fong et al. (2022)				
				UKIRT/WFCAM	J	21.72±0.01	Fong et al. (2022)				
				UKIRT/WFCAM	K	21.43±0.18	Fong et al. (2022)				
				GRB110402A	13:09:36.53	61:15:09.90	0.854	GMOS-N	r	24.20±0.20	O'Connor et al. (2022a)
								LDT/LMI	i	23.32±0.09	O'Connor et al. (2022a)
LDT/LMI	z	22.98±0.16	O'Connor et al. (2022a)								
Keck/LRIS	B	24.13±0.11	O'Connor et al. (2022a)								
Keck/LRIS	I	23.32±0.10	O'Connor et al. (2022a)								
GRB111117A	00:50:46.27	23:00:41.41	2.211	VLT/FORS2	g	23.98±0.09	Selsing et al. (2018)				
				GTC/OSIRIS	r	23.86±0.08	Selsing et al. (2018)				
				GTC/OSIRIS	i	23.84±0.23	Selsing et al. (2018)				

Continued on next page

Target	RA	Dec	redshift	Instrument	Filter	ABmag	Reference ^a
GRB120305A	03:10:08.75	28:29:35.87	0.225	VLT/FORS2	z	23.72±0.21	Selsing et al. (2018)
				VLT/HAWK-I	J	23.11±0.18	Selsing et al. (2018)
				VLT/HAWK-I	H	22.93±0.29	Selsing et al. (2018)
				VLT/HAWK-I	K	23.06±0.32	Selsing et al. (2018)
				MMT	g	23.54±0.23	Fong et al. (2022)
				LBT	r	22.40±0.05	Fong et al. (2022)
				GMOS-N	i	21.42±0.02	Fong et al. (2022)
				LBT	z	21.60±0.05	Fong et al. (2022)
GRB120630A	23:29:11.07	42:33:20.30	0.544 ^{+0.13} _{-0.08}	UKIRT	J	21.23±0.17	Fong et al. (2022)
				MMT	H	21.56±0.13	Fong et al. (2022)
				Keck/LRIS	G	22.11±0.03	O'Connor et al. (2022a)
				GMOS-N	r	21.39±0.06	O'Connor et al. (2022a)
				GMOS-N	i	21.06±0.07	O'Connor et al. (2022a)
				GMOS-N	z	20.94±0.05	O'Connor et al. (2022a)
				WISE	W1	19.46±0.05	O'Connor et al. (2022a)
				WISE	W2	19.59±0.08	O'Connor et al. (2022a)
GRB120804A	15:35:47.51	-28:46:56.11	1.258 ^{+0.36} _{-0.37}	GMOS-N	r	26.41±0.20	Berger et al. (2013)
				GMOS-N	i	25.18±0.15	Berger et al. (2013)
				VLT/HAWK-I	Y	23.93±0.30	Berger et al. (2013)
				Magellan/FourStar	J	23.16±0.20	Berger et al. (2013)
GRB121226A	11:14:34.12	-30:24:22.84	2.103 ^{+0.20} _{-0.18}	VLT/HAWK-I	K	22.07±0.10	Berger et al. (2013)
				Magellan/LDSS	g	24.82±0.10	Fong et al. (2022)
				Magellan/LDSS	r	24.31±0.06	Fong et al. (2022)
				Magellan/LDSS	i	24.00±0.10	Fong et al. (2022)
				Magellan/LDSS	z	23.82±0.15	Fong et al. (2022)
				Magellan/FourStar	J	22.82±0.10	Fong et al. (2022)
				Magellan/FourStar	H	22.45±0.11	Fong et al. (2022)
				Magellan/FourStar	K	21.37±0.10	Fong et al. (2022)
GRB130515A	18:53:45.02	-54:16:50.72	0.891 ^{+0.05} _{-0.05}	Magellan/IMACS	g	22.46±0.06	Fong et al. (2022)
				Magellan/LDSS	r	22.65±0.04	Fong et al. (2022)
				Magellan/LDSS	i	20.90±0.02	Fong et al. (2022)
				Magellan/IMACS	z	20.89±0.10	Fong et al. (2022)
				LCO/Fourstar	J	20.56±0.21	Fong et al. (2022)
				LCO/Fourstar	H	20.56±0.09	Fong et al. (2022)
				LCO/Fourstar	K	20.29±0.04	Fong et al. (2022)
				GRB130603B	11:28:48.23	17:04:18.61	0.357
HST/ACS	F606W	21.08±0.04	Fong & Berger (2013)				
DECaLS	r	20.82±0.04	Dey et al. (2019)*				
PS1	i	20.78±0.11	Chambers et al. (2016)*				
DECaLS	z	20.27±0.04	Dey et al. (2019)*				
WFC3/IR	F160W	19.83±0.02	Fong & Berger (2013)				
WISE	W1	19.75±0.11	Klose et al. (2019)				
WISE	W2	20.29±0.37	Klose et al. (2019)				
GRB130822A	01:51:42.71	-03:12:25.45	0.154	MMT/Binospec	g	18.86±0.07	Fong et al. (2022)
				MMT/MMTCam	r	18.25±0.06	Fong et al. (2022)
				Magellan/LDSS	i	17.91±0.03	Fong et al. (2022)
				MMT/Binospec	z	17.55±0.08	Fong et al. (2022)

Continued on next page

Target	RA	Dec	redshift	Instrument	Filter	ABmag	Reference ^a
GRB140129B	21:47:01.65	26:12:23.27	0.43	Magellan/FourStar	J	17.29±0.05	Fong et al. (2022)
				Magellan/LDSS	g	24.18±0.10	Fong et al. (2022)
				Magellan/LDSS	r	23.55±0.07	Fong et al. (2022)
				Magellan/LDSS	i	22.68±0.07	Fong et al. (2022)
				Magellan/LDSS	z	22.95±0.14	Fong et al. (2022)
				MMT/MMIRS	Y	22.68±0.21	Fong et al. (2022)
				LCO/Fourstar	J	22.78±0.19	Fong et al. (2022)
				HST/WFCAM	H	22.21±0.33	Fong et al. (2022)
GRB140622A	21:08:41.74	-14:25:06.17	0.959	HST/WFCAM	K	21.99±0.34	Fong et al. (2022)
				Magellan/LDSS	g	23.35±0.06	Fong et al. (2022)
				Magellan/LDSS	r	22.70±0.04	Fong et al. (2022)
				Magellan/LDSS	i	22.09±0.03	Fong et al. (2022)
				Magellan/LDSS	z	21.72±0.06	Fong et al. (2022)
				Magellan/FourStar	J	21.54±0.10	Fong et al. (2022)
				Magellan/FourStar	H	21.19±0.10	Fong et al. (2022)
				Magellan/FourStar	K	20.41±0.08	Fong et al. (2022)
GRB140903A	15:52:03.27	27:36:10.71	0.353	DCT/LMI	g	21.87±0.16	Troja et al. (2016)
				DCT/LMI	r	20.51±0.09	Troja et al. (2016)
				DCT/LMI	i	20.07±0.05	Troja et al. (2016)
				DCT/LMI	z	19.62±0.08	Troja et al. (2016)
				CAHA/Omega2000	J	18.90±0.05	Troja et al. (2016)
				CAHA/Omega2000	H	18.56±0.07	Troja et al. (2016)
				CAHA/Omega2000	K	18.24±0.05	Troja et al. (2016)
				GRB140930B	00:25:23.47	24:17:37.93	1.465
MMT/MMTCam	r	24.21±0.25	Fong et al. (2022)				
LBT/MODS	i	24.09±0.21	Fong et al. (2022)				
LBT/MODS	z	>23.20	Fong et al. (2022)				
MMT/MMIRS	Y	23.59±0.17	Fong et al. (2022)				
MMT/MMIRS	J	23.65±0.33	Fong et al. (2022)				
MMT/MMIRS	H	23.16±0.17	Fong et al. (2022)				
MMT/MMIRS	K	22.62±0.16	Fong et al. (2022)				
GRB141212A	02:36:29.96	18:08:47.23	0.596	LBT/LBC	g	24.04±0.10	Fong et al. (2022)
				LBT/LBC	r	22.95±0.06	Fong et al. (2022)
				LBT/LBC	i	22.29±0.05	Fong et al. (2022)
				LBT/LBC	z	22.06±0.06	Fong et al. (2022)
				UKIRT/WFCAM	Y	21.53±0.30	Fong et al. (2022)
				UKIRT/WFCAM	J	21.95±0.24	Fong et al. (2022)
				UKIRT/WFCAM	H	21.44±0.16	Fong et al. (2022)
				UKIRT/WFCAM	K	21.65±0.24	Fong et al. (2022)
GRB150101B	12:32:04.97	-10:56:00.50	0.134	WISE	W1	20.45±0.20	Wright et al. (2010)
				PS1	g	17.43±0.06	Chambers et al. (2016)*
				WFC3/UVIS	F606W	16.57±0.01	Fong et al. (2016)
				PS1	r	16.56±0.04	Chambers et al. (2016)*
				PS1	i	16.18±0.04	Chambers et al. (2016)*
				PS1	z	15.89±0.08	Chambers et al. (2016)*
				PS1	y	15.67±0.10	Chambers et al. (2016)*
				UKIRT/WFCAM	J	15.55±0.05	Fong et al. (2016)

Continued on next page

Target	RA	Dec	redshift	Instrument	Filter	ABmag	Reference ^a				
GRB150120A	00:41:16.56	33:59:42.60	0.46	WFC3/IR	F160W	15.09±0.01	Fong et al. (2016)				
				UKIRT/WFCAM	K	15.20±0.06	Fong et al. (2016)				
				WISE	W1	16.13±0.03	Klose et al. (2019)				
				WISE	W2	16.51±0.03	Klose et al. (2019)				
				LBT/LBC	g	23.35±0.06	Fong et al. (2022)				
				LBT/LBC	r	22.05±0.06	Fong et al. (2022)				
				LBT/LBC	i	21.44±0.05	Fong et al. (2022)				
				LBT/LBC	z	21.02±0.06	Fong et al. (2022)				
				MMT/MMIRS	Y	20.63±0.10	Fong et al. (2022)				
				UKIRT/UFTI	J	20.44±0.08	Fong et al. (2022)				
GRB150728A	19:28:54.81	33:54:58.22	0.461	UKIRT/UFTI	H	20.31±0.05	Fong et al. (2022)				
				UKIRT/UFTI	K	19.45±0.06	Fong et al. (2022)				
				LBT/MODS	g	22.45±0.07	Fong et al. (2022)				
				LBT/LBC	r	21.42±0.05	Fong et al. (2022)				
				LBT/LBC	i	20.99±0.05	Fong et al. (2022)				
				LBT/MODS	z	20.97±0.06	Fong et al. (2022)				
				UKIRT/WFCAM	Y	20.84±0.11	Fong et al. (2022)				
				UKIRT/WFCAM	J	20.66±0.07	Fong et al. (2022)				
				UKIRT/WFCAM	H	20.32±0.05	Fong et al. (2022)				
				UKIRT/WFCAM	K	20.26±0.08	Fong et al. (2022)				
GRB150831A	14:44:05.94	-25:38:05.78	1.18	Magellan/LDSS	g	26.00±0.32	Fong et al. (2022)				
				Magellan/IMACS	r	24.43±0.45	Fong et al. (2022)				
				GMOS-S	i	24.67±0.10	Fong et al. (2022)				
				Magellan/LDSS	z	23.74±0.10	Fong et al. (2022)				
				Magellan/FourStar	J	23.59±0.30	Fong et al. (2022)				
				Magellan/FourStar	H	22.87±0.32	Fong et al. (2022)				
				UKIRT/WFCAM	K	22.63±0.30	Fong et al. (2022)				
				GRB151229A	21:57:28.70	-20:43:54.80	1.879 ^{+0.80} _{-0.80}	Magellan	g	>23.89	Fong et al. (2022)
								Magellan	r	>24.49	Fong et al. (2022)
								Magellan	i	24.92±0.13	Fong et al. (2022)
GMOS-S	z	24.46±0.08	Fong et al. (2022)								
Keck	Y	24.41±0.35	Fong et al. (2022)								
LCO/Fourstar	J	24.16±0.39	Fong et al. (2022)								
LCO/Fourstar	K	22.80±0.26	Fong et al. (2022)								
GRB160303A	11:14:48.12	22:44:33.42	1.095 ^{+0.28} _{-0.28}					LBT/MODS	g	>25.75	Fong et al. (2022)
								GTC/OSIRIS	r	25.80±0.30	Cano et al. (2016)
								MMT/MMTCam	i	25.33±0.24	Fong et al. (2022)
				Magellan/IMACS	z	23.67±0.16	Fong et al. (2022)				
				HST/WFC3	F110W	23.77±0.02	Fong et al. (2022)				
				Keck/MOSFIRE	K	22.83±0.39	Fong et al. (2022)				
				GRB160408A	08:10:29.58	71:07:45.03	1.483 ^{+0.72} _{-0.65}	LBT/MODS	g	25.52±0.27	Fong et al. (2022)
								GMOS	r	25.74±0.16	Fong et al. (2022)
								MMT/MMTCam	i	>25.20	Fong et al. (2022)
								LBT/MODS	z	25.23±0.27	Fong et al. (2022)
MMT/MMIRS	J	>22.80	Fong et al. (2022)								
GRB160411A	23:17:25.36	-40:14:30.56	0.732 ^{+0.37} _{-0.42}					Magellan/IMACS	g	25.26±0.35	Fong et al. (2022)
								Magellan/LDSS	r	24.58±0.13	Fong et al. (2022)

Continued on next page

Target	RA	Dec	redshift	Instrument	Filter	ABmag	Reference ^a
GRB160525B	09:57:32.25	51:12:24.60	$0.576^{+0.07}_{-0.08}$	Magellan/LDSS	i	24.18±0.12	Fong et al. (2022)
				Magellan/LDSS	z	24.04±0.21	Fong et al. (2022)
				Magellan/FourStar	J	23.16±0.17	Fong et al. (2022)
				Magellan/FourStar	K	23.19±0.24	Fong et al. (2022)
				LDT/LMI	g	23.27±0.03	O'Connor et al. (2022a)
				LDT/LMI	r	23.27±0.02	O'Connor et al. (2022a)
				LDT/LMI	i	23.27±0.02	O'Connor et al. (2022a)
				LDT/LMI	z	23.39±0.01	O'Connor et al. (2022a)
GRB160624A	22:00:46.15	29:38:39.34	0.484	Keck/LRIS	V	23.84±0.07	Fong et al. (2022)
				Keck/LRIS	RG850	24.27±0.39	Fong et al. (2022)
				LDT/LMI	g	23.09±0.09	O'Connor et al. (2021)
				LDT/LMI	r	22.01±0.08	O'Connor et al. (2021)
				GMOS	r	22.03±0.02	O'Connor et al. (2021)
				LDT/LMI	i	21.55±0.08	O'Connor et al. (2021)
				LDT/LMI	z	21.39±0.08	O'Connor et al. (2021)
				Gemini/NIRI	Y	21.35±0.15	O'Connor et al. (2021)
				HST/WFC3	F125W	20.79±0.01	O'Connor et al. (2021)
				HST/WFC3	F160W	20.54±0.01	O'Connor et al. (2021)
GRB160821B	18:39:53.99	62:23:34.43	0.162	Gemini/NIRI	K	20.30±0.08	O'Connor et al. (2021)
				PS1	g	19.78±0.06	Chambers et al. (2016)*
				HST/WFC3	F606W	19.48±0.04	Jin et al. (2018)*
				PS1	r	19.49±0.07	Chambers et al. (2016)*
				PS1	i	19.31±0.10	Chambers et al. (2016)*
				PS1	z	19.29±0.11	Chambers et al. (2016)*
				PS1	y	19.17±0.17	Chambers et al. (2016)*
				HST/WFC3	F160W	19.08±0.03	Jin et al. (2018)*
GRB161001A	04:47:40.53	-57:15:39.18	$0.776^{+0.07}_{-0.07}$	Magellan/IMACS	g	24.11±0.07	Fong et al. (2022)
				Magellan/IMACS	r	22.97±0.05	Fong et al. (2022)
				Magellan/IMACS	i	22.19±0.04	Fong et al. (2022)
				Magellan/IMACS	z	21.49±0.06	Fong et al. (2022)
				Magellan/FourStar	J	21.84±0.09	Fong et al. (2022)
				Magellan/FourStar	K	21.26±0.08	Fong et al. (2022)
GRB161104A	05:11:34.37	-51:27:36.29	0.793	Magellan/IMACS	g	25.06±0.25	Nugent et al. (2020)*
				Magellan/IMACS	r	23.43±0.10	Nugent et al. (2020)*
				Magellan/IMACS	i	22.34±0.06	Nugent et al. (2020)*
				Magellan/IMACS	z	21.76±0.07	Nugent et al. (2020)*
				Magellan/FourStar	J	21.18±0.04	Nugent et al. (2020)*
GRB170127B	01:19:54.41	-30:21:29.61	$1.443^{+0.42}_{-0.33}$	Keck/LRIS	G	25.26±0.16	Fong et al. (2022)
				Magellan/LDSS3	r	25.32±0.29	Fong et al. (2022)
				Keck/LRIS	I	25.81±0.33	Fong et al. (2022)
				Magellan/IMACS	z	24.27±0.21	Fong et al. (2022)
				Keck/MOSFIRE	J	>23.40	Fong et al. (2022)
				Magellan/FourStar	K	>22.80	Fong et al. (2022)
GRB170428A	22:00:18.71	26:54:56.28	0.453	MMT/MMTCam	g	23.77±0.18	Fong et al. (2022)
				MMT/MMTCam	r	22.35±0.10	Fong et al. (2022)
				MMT/MMTCam	i	22.55±0.07	Fong et al. (2022)
				MMT/MMTCam	z	22.09±0.11	Fong et al. (2022)
				MMT/Binospec	z	22.09±0.11	Fong et al. (2022)

Continued on next page

Target	RA	Dec	redshift	Instrument	Filter	ABmag	Reference ^a
GRB170728A	03:55:33.12	12:10:51.04	1.493	UKIRT/WFCAM	Y	21.08±0.16	Fong et al. (2022)
				UKIRT/WFCAM	J	21.48±0.12	Fong et al. (2022)
				UKIRT/WFCAM	H	21.02±0.15	Fong et al. (2022)
				UKIRT/WFCAM	K	20.93±0.09	Fong et al. (2022)
				LBT/MODS	g	25.51±0.19	Fong et al. (2022)
				Keck/LRIS	r	24.73±0.14	Fong et al. (2022)
				Magellan/IMACS	i	24.31±0.28	Fong et al. (2022)
				MMT/Binospec	z	24.40±0.33	Fong et al. (2022)
GRB170728B	15:51:55.53	70:07:22.04	1.272	MMT/MMIRS	J	22.15±0.09	Fong et al. (2022)
				MMT/MMIRS	K	21.22±0.12	Fong et al. (2022)
				MMT/Binospec	r	23.31±0.10	Fong et al. (2022)
				MMT/MMIRS	J	22.24±0.13	Fong et al. (2022)
GRB170817A	13:09:47.70	-23:23:02.00	0.00979	MMT/MMIRS	K	21.73±0.27	Fong et al. (2022)
				GALEX	FUV	>18.86	Blanchard et al. (2017)
				GALEX	NUV	17.82±0.09	Blanchard et al. (2017)
GRB180418A	11:20:29.21	24:55:58.73	1.094 ^{+0.78} _{-0.63}	PS1	g	12.80±0.02	Blanchard et al. (2017)
				PS1	r	12.16±0.01	Blanchard et al. (2017)
				PS1	i	11.81±0.01	Blanchard et al. (2017)
				PS1	z	11.57±0.01	Blanchard et al. (2017)
				PS1	y	11.36±0.02	Blanchard et al. (2017)
				2MASS	J	10.98±0.02	Blanchard et al. (2017)
				2MASS	H	10.82±0.02	Blanchard et al. (2017)
				2MASS	K	11.02±0.02	Blanchard et al. (2017)
				WISE	W1	11.92±0.01	Blanchard et al. (2017)
				WISE	W2	12.59±0.01	Blanchard et al. (2017)
				GMOS-N	r	25.69±0.21	Rouco Escorial et al. (2021)
				GMOS-N	i	24.82±0.14	Rouco Escorial et al. (2021)
GMOS-N	z	24.62±0.21	Rouco Escorial et al. (2021)				
GRB180618A	11:19:45.80	73:50:15.03	0.643 ^{+0.09} _{-0.09}	MMT/MMIRS	J	22.94±0.36	Rouco Escorial et al. (2021)
				MMT/MMIRS	H	>22.80	Rouco Escorial et al. (2021)
				MMT/MMIRS	K	>22.40	Rouco Escorial et al. (2021)
				DECaLS	g	25.06±0.39	Dey et al. (2019)*
GRB180805B	01:43:07.66	-17:29:33.09	0.661	DECaLS	r	23.47±0.13	Dey et al. (2019)*
				MMT/Binospec	i	22.18±0.08	Fong et al. (2022)
				MMT/MMIRS	J	22.42±0.19	Fong et al. (2022)
				MMT/MMIRS	K	21.91±0.19	Fong et al. (2022)
				Keck/LRIS	G	23.71±0.09	Fong et al. (2022)
				Magellan/IMACS	r	22.15±0.06	Fong et al. (2022)
GRB181123B	12:17:27.91	14:35:52.27	1.75	Keck/LRIS	I	22.22±0.06	Fong et al. (2022)
				Keck/LRIS	RG850	22.21±0.07	Fong et al. (2022)
				Keck/MOSFIRE	J	22.09±0.08	Fong et al. (2022)
				Keck/MOSFIRE	K	21.49±0.14	Fong et al. (2022)
				GMOS-N	g	24.08±0.23	Paterson et al. (2020)
				GMOS-N	r	23.84±0.19	Paterson et al. (2020)
GRB181123B	12:17:27.91	14:35:52.27	1.75	GMOS-N	i	23.79±0.19	Paterson et al. (2020)
				GMOS-N	z	23.84±0.22	Paterson et al. (2020)
				MMT/MMIRS	Y	22.78±0.24	Paterson et al. (2020)
				MMT/MMIRS	Y	22.78±0.24	Paterson et al. (2020)

Continued on next page

Target	RA	Dec	redshift	Instrument	Filter	ABmag	Reference ^a				
GRB191031D	18:53:09.52	47:38:40.13	$1.607^{+0.33}_{-0.24}$	Keck/MOSFIRE	J	22.85±0.23	Paterson et al. (2020)				
				MMT/MMIRS	H	22.61±0.19	Paterson et al. (2020)				
				MMT/MMIRS	K	22.33±0.23	Paterson et al. (2020)				
				MMT/Binospec	r	24.46±0.26	Fong et al. (2022)				
				MMT/Binospec	i	24.83±0.30	Fong et al. (2022)				
				MMT/Binospec	z	24.36±0.38	Fong et al. (2022)				
				MMT/MMIRS	Y	23.78±0.27	Fong et al. (2022)				
				MMT/MMIRS	J	22.87±0.01	Fong et al. (2022)				
GRB200219A	22:50:33.11	-59:07:11.58	$0.457^{+0.18}_{-0.21}$	MMT/MMIRS	K	21.85±0.08	Fong et al. (2022)				
				DECaLS	g	21.96±0.01	Fong et al. (2022)				
				DECaLS	r	20.66±0.05	Fong et al. (2022)				
				DECaLS	z	19.76±0.03	Fong et al. (2022)				
				WISE	W1	18.62±0.02	Fong et al. (2022)				
				WISE	W2	19.62±0.07	Fong et al. (2022)				
GRB200411A	03:10:39.13	-52:18:59.55	$1.145^{+0.07}_{-0.06}$	DECaLS	g	22.51±0.09	Fong et al. (2022)				
				DECaLS	r	22.56±0.04	Fong et al. (2022)				
				DES	i	22.20±0.10	Fong et al. (2022)				
				DECaLS	z	21.12±0.03	Fong et al. (2022)				
				VISTA	J	21.10±0.20	Fong et al. (2022)				
				VISTA	K	20.00±0.20	Fong et al. (2022)				
				WISE	W1	20.00±0.10	Fong et al. (2022)				
				WISE	W2	20.20±0.30	Fong et al. (2022)				
				GRB200522A	00:22:43.72	-00:16:57.47	0.554	SDSS	u	22.43±0.31	Alam et al. (2015)
								DECam	g	22.10±0.06	Abbott et al. (2021c)*
DECam	r	21.28±0.05	Abbott et al. (2021c)*								
DECam	i	21.01±0.05	Abbott et al. (2021c)*								
DECam	z	20.98±0.07	Abbott et al. (2021c)*								
DECam	Y	20.77±0.15	Abbott et al. (2021c)*								
HST/WFC3	F125W	20.84±0.01	Fong et al. (2021)								
HST/WFC3	F160W	20.67±0.01	Fong et al. (2021)								
GRB201221D	11:24:14.06	42:08:40.05	1.055	DECaLS	g	23.96±0.15	Dey et al. (2019)*				
				MMT/Binospec	r	23.42±0.08	Fong et al. (2022)				
				MMT/Binospec	i	23.36±0.13	Fong et al. (2022)				
				MMT/MMIRS	Y	23.01±0.13	Fong et al. (2022)				
				MMT/MMIRS	J	22.33±0.09	Fong et al. (2022)				
				MMT/MMIRS	H	22.88±0.18	Fong et al. (2022)				
				Keck/MOSFIRE	K	22.20±0.13	Fong et al. (2022)				
				GRB210323A	21:11:47.32	25:22:09.99	0.733	Keck/LRIS	B	24.77±0.13	Fong et al. (2022)
Keck/LRIS	R	24.70±0.11	Fong et al. (2022)								
Keck/LRIS	g	24.88±0.11	Fong et al. (2022)								
MMT/Binospec	r	24.97±0.25	Fong et al. (2022)								
MMT/Binospec	i	23.98±0.14	Fong et al. (2022)								
GRB210510A	13:48:49.89	35:32:13.05	0.221	PS1	g	21.36±0.08	Chambers et al. (2016)*				
				PS1	r	21.03±0.09	Chambers et al. (2016)*				
				PS1	i	20.55±0.08	Chambers et al. (2016)*				
				PS1	z	20.19±0.08	Chambers et al. (2016)*				
				PS1	y	19.64±0.13	Chambers et al. (2016)*				

Continued on next page

Target	RA	Dec	redshift	Instrument	Filter	ABmag	Reference ^a
GRB210726A	12:53:09.82	19:11:25.03	0.458 ^{+0.17} _{-0.18}	WISE	W1	18.65±0.05	Wright et al. (2010)
				WISE	W2	18.32±0.06	Wright et al. (2010)
				Keck/LRIS	B	>26.16	Fong et al. (2022)
				Keck/LRIS	R	25.37±0.20	Fong et al. (2022)
				GMOS-N	g	25.78±0.30	Fong et al. (2022)
				GMOS-N	i	25.24±0.28	Fong et al. (2022)
				GMOS-N	z	24.88±0.31	Fong et al. (2022)
GRB210919A	05:21:01.95	01:18:40.02	0.242	MMT/MMIRS	J	>22.91	Fong et al. (2022)
				SDSS	u	25.73±0.98	Fong et al. (2022)
				SDSS	g	21.51±0.07	Fong et al. (2022)
				SDSS	r	20.50±0.05	Fong et al. (2022)
				SDSS	i	19.93±0.05	Fong et al. (2022)
				SDSS	z	19.60±0.14	Fong et al. (2022)
				MMT/MMIRS	J	19.08±0.07	Fong et al. (2022)
GRB211023B	11:21:14.31	39:08:08.36	0.862	MMT/MMIRS	H	18.88±0.06	Fong et al. (2022)
				DECaLS	g	24.32±0.22	Fong et al. (2022)
				DECaLS	r	24.36±0.38	Fong et al. (2022)
				GMOS-N	i	23.35±0.14	Fong et al. (2022)
				DECaLS	z	23.31±0.24	Fong et al. (2022)
GRB211211A	14:09:10.47	27:53:21.05	0.0763	SDSS	u	20.93±0.13	Fong et al. (2022)
				MMT/Binospec	g	19.84±0.06	Rastinejad et al. (2022)
				MMT/Binospec	r	19.46±0.04	Rastinejad et al. (2022)
				GMOS-N	i	19.19±0.05	Rastinejad et al. (2022)
				MMT/Binospec	z	19.20±0.08	Rastinejad et al. (2022)
				MMT/MMIRS	J	19.01±0.01	Rastinejad et al. (2022)
				MMT/MMIRS	K	19.23±0.07	Rastinejad et al. (2022)
				WISE	W1	19.76±0.05	Rastinejad et al. (2022)
				HST/ACS	F606W	19.57±0.01	Rastinejad et al. (2022)
				HST/WFC3	F140W	18.96±0.01	Rastinejad et al. (2022)
GRB211227A	08:48:35.98	-02:44:06.93	0.228	SDSS	u	22.89±0.97	Alam et al. (2015)
				PS1	g	19.90±0.06	Chambers et al. (2016)*
				PS1	r	19.26±0.05	Chambers et al. (2016)*
				PS1	i	18.77±0.07	Chambers et al. (2016)*
				PS1	z	18.70±0.07	Chambers et al. (2016)*
				PS1	y	18.11±0.11	Chambers et al. (2016)*
GRB221120A	02:45:22.00	43:14:47.40	0.08 ^{+0.04} _{-0.03}	GALEX	FUV	20.66±0.45	Martin et al. (2005)
				GALEX	NUV	19.42±0.17	Martin et al. (2005)
				PS1	g	18.04±0.05	Chambers et al. (2016)*
				PS1	r	17.53±0.05	Chambers et al. (2016)*
				PS1	i	16.95±0.08	Chambers et al. (2016)*
				UKIRT/WFCAM	J	15.79±0.07	Dye et al. (2018)
				WISE	W1	14.54±0.03	Wright et al. (2010)
WISE	W2	14.27±0.05	Wright et al. (2010)				

Notes:

^a The original reference provides the image and photometric data. An asterisk next to a reference denotes that we utilized archival images from that source to conduct photometry.

SED of Short GRB Host Galaxies

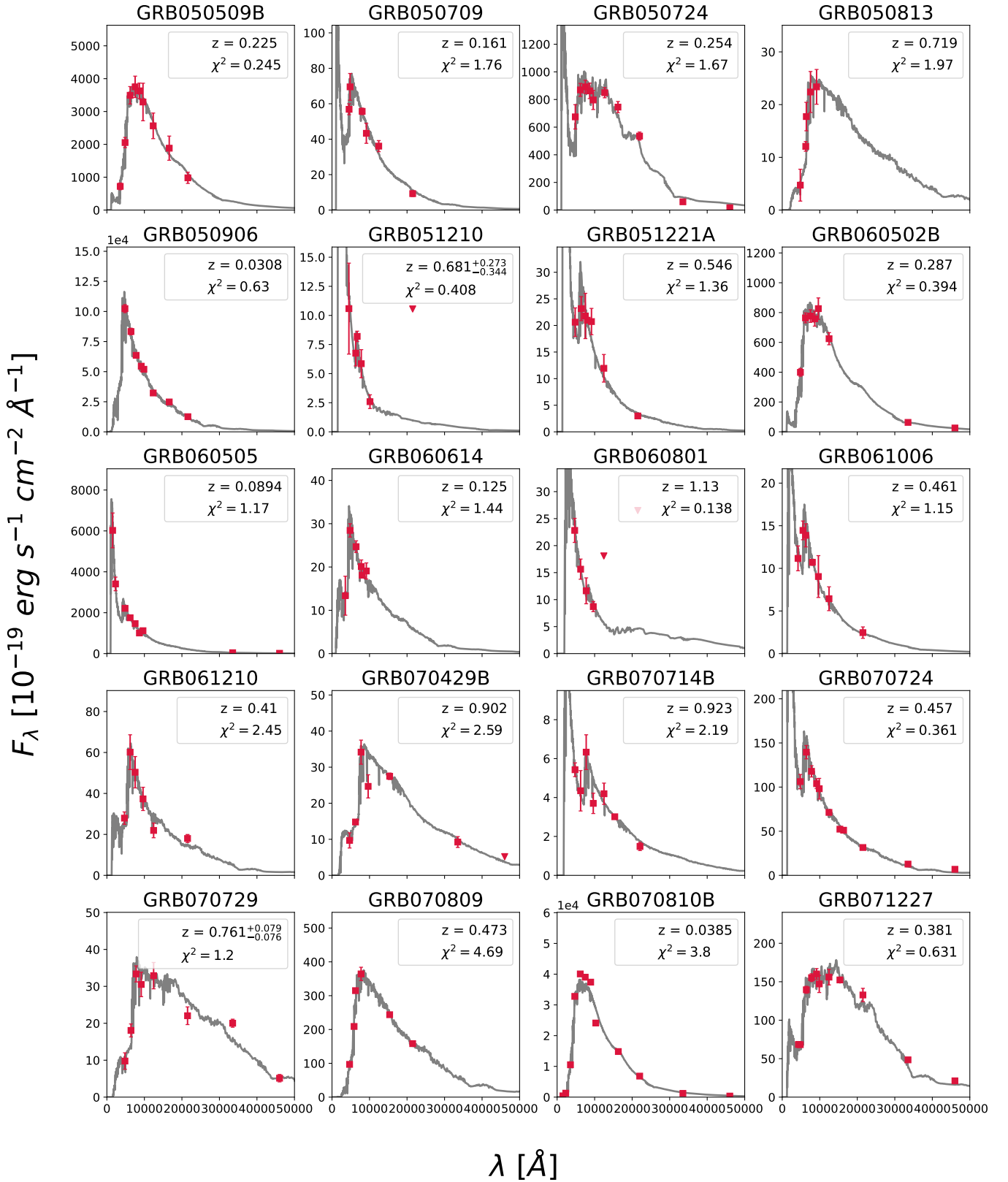


Figure A1. Best fit SED models and photometric data points of short and hybrid GRB host galaxies. (Part 1)

SED of Short GRB Host Galaxies

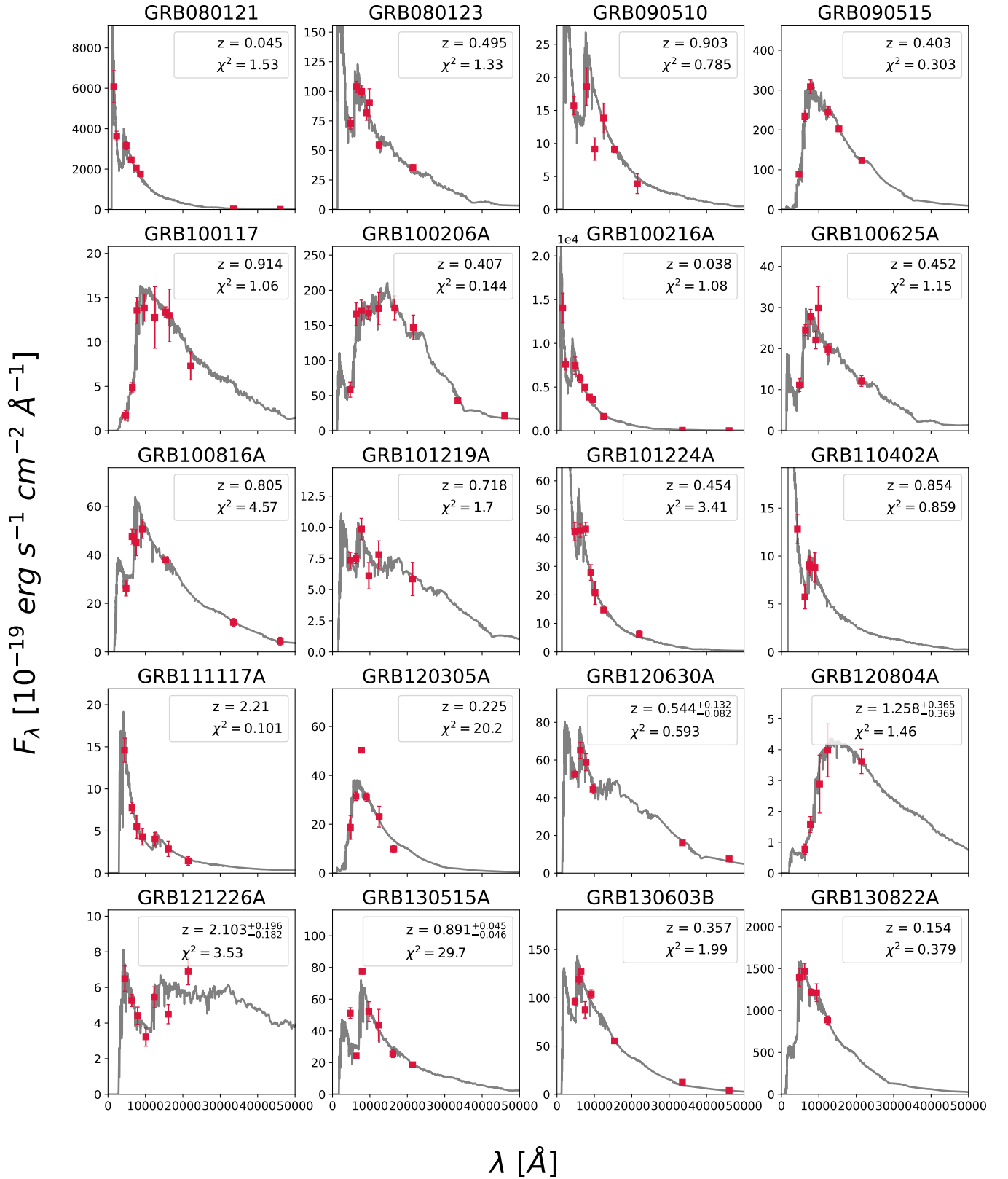


Figure A2. Best fit SED models and photometric data points of short and hybrid GRB host galaxies. (Part 2)

SED of Short GRB Host Galaxies

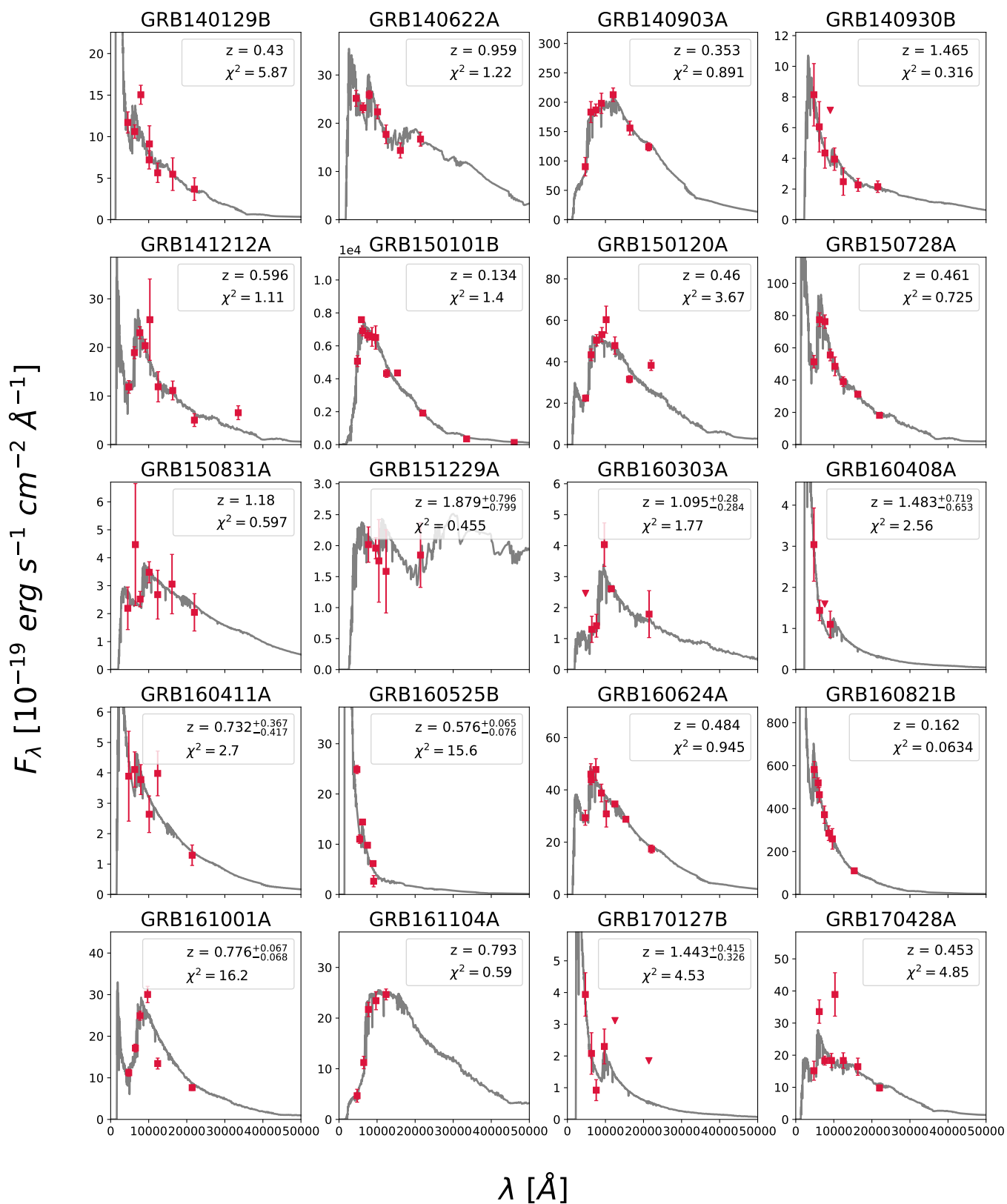


Figure A3. Best fit SED models and photometric data points of short and hybrid GRB host galaxies. (Part 3)

SED of Short GRB Host Galaxies

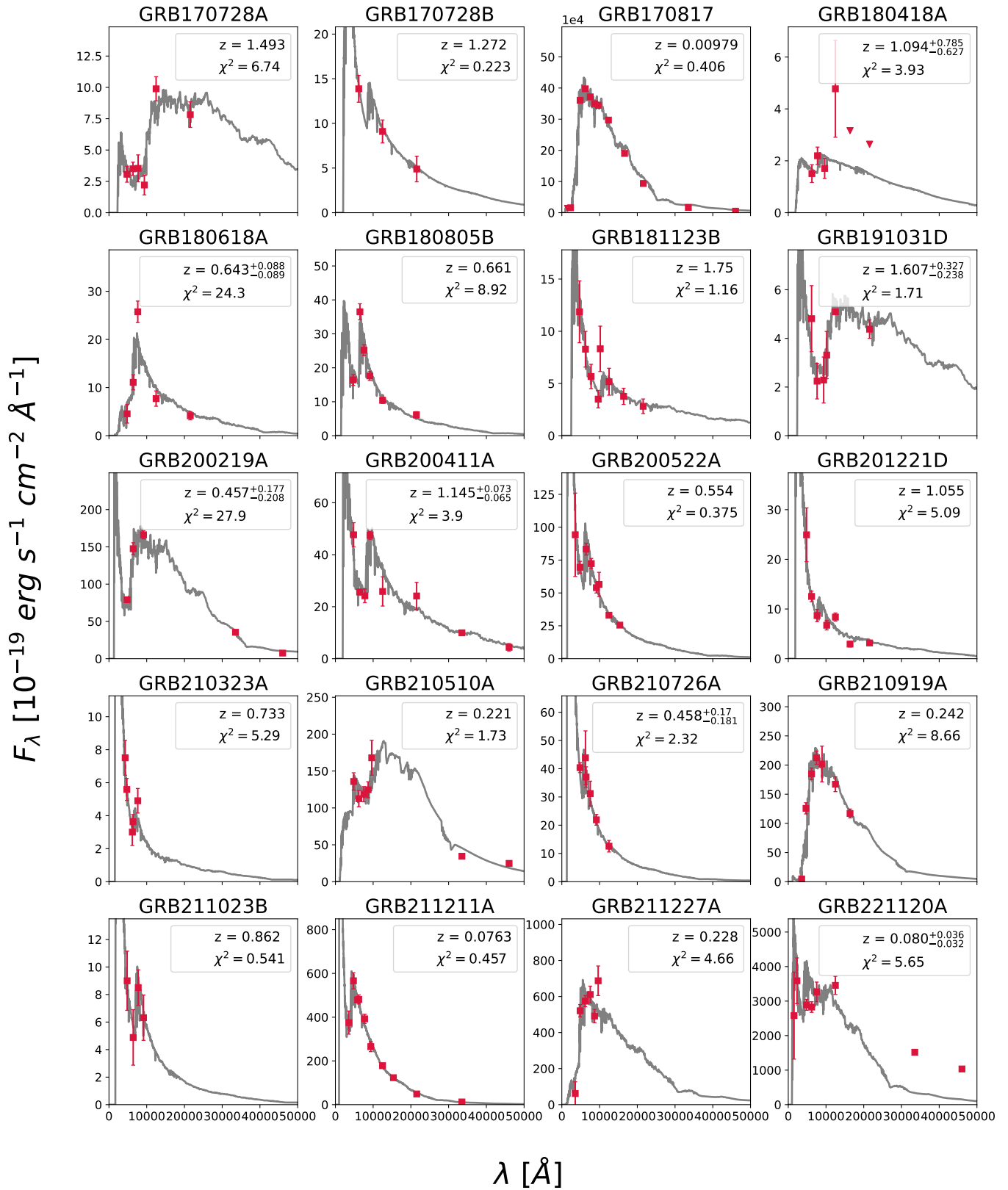


Figure A4. Best fit SED models and photometric data points of short and hybrid GRB host galaxies. (Part 4)

REFERENCES

- Abbott, B. P., Abbott, R., Abbott, T. D., et al. 2016, *PhRvL*, 116, 061102, doi: [10.1103/PhysRevLett.116.061102](https://doi.org/10.1103/PhysRevLett.116.061102)
- . 2017a, *ApJL*, 848, L12, doi: [10.3847/2041-8213/aa91c9](https://doi.org/10.3847/2041-8213/aa91c9)
- . 2017b, *ApJL*, 848, L13, doi: [10.3847/2041-8213/aa920c](https://doi.org/10.3847/2041-8213/aa920c)
- . 2017c, *Nature*, 551, 85, doi: [10.1038/nature24471](https://doi.org/10.1038/nature24471)
- . 2018, *Living Reviews in Relativity*, 21, 3, doi: [10.1007/s41114-018-0012-9](https://doi.org/10.1007/s41114-018-0012-9)
- . 2020a, *Living Reviews in Relativity*, 23, 3, doi: [10.1007/s41114-020-00026-9](https://doi.org/10.1007/s41114-020-00026-9)
- . 2020b, *ApJL*, 892, L3, doi: [10.3847/2041-8213/ab75f5](https://doi.org/10.3847/2041-8213/ab75f5)
- . 2021a, *ApJ*, 909, 218, doi: [10.3847/1538-4357/abdcb7](https://doi.org/10.3847/1538-4357/abdcb7)
- Abbott, R., Abbott, T. D., Abraham, S., et al. 2021b, *ApJL*, 913, L7, doi: [10.3847/2041-8213/abe949](https://doi.org/10.3847/2041-8213/abe949)
- Abbott, T. M. C., Adamów, M., Agüena, M., et al. 2021c, *ApJS*, 255, 20, doi: [10.3847/1538-4365/ac00b3](https://doi.org/10.3847/1538-4365/ac00b3)
- Acernese, F., Agathos, M., Agatsuma, K., et al. 2015, *Classical and Quantum Gravity*, 32, 024001, doi: [10.1088/0264-9381/32/2/024001](https://doi.org/10.1088/0264-9381/32/2/024001)
- Adhikari, S., Fishbach, M., Holz, D. E., Wechsler, R. H., & Fang, Z. 2020, *ApJ*, 905, 21, doi: [10.3847/1538-4357/abfbf7](https://doi.org/10.3847/1538-4357/abfbf7)
- Akutsu, T., Ando, M., Arai, K., et al. 2021, *Progress of Theoretical and Experimental Physics*, 2021, 05A101, doi: [10.1093/ptep/ptaa125](https://doi.org/10.1093/ptep/ptaa125)
- Alam, S., Albareti, F. D., Allende Prieto, C., et al. 2015, *ApJS*, 219, 12, doi: [10.1088/0067-0049/219/1/12](https://doi.org/10.1088/0067-0049/219/1/12)
- Anand, S., Andreoni, I., Ahumada, T., et al. 2021, *GRB Coordinates Network*, 30005, 1
- Antonelli, L. A., D’Avanzo, P., Perna, R., et al. 2009, *A&A*, 507, L45, doi: [10.1051/0004-6361/200913062](https://doi.org/10.1051/0004-6361/200913062)
- Arcavi, I., Hosseinzadeh, G., Howell, D. A., et al. 2017, *Nature*, 551, 64, doi: [10.1038/nature24291](https://doi.org/10.1038/nature24291)
- Artale, M. C., Mapelli, M., Bouffanais, Y., et al. 2020, *MNRAS*, 491, 3419, doi: [10.1093/mnras/stz3190](https://doi.org/10.1093/mnras/stz3190)
- Ascenzi, S., Coughlin, M. W., Dietrich, T., et al. 2019, *MNRAS*, 486, 672, doi: [10.1093/mnras/stz891](https://doi.org/10.1093/mnras/stz891)
- Barthelmy, S. D., Barbier, L. M., Cummings, J. R., et al. 2005, *SSRv*, 120, 143, doi: [10.1007/s11214-005-5096-3](https://doi.org/10.1007/s11214-005-5096-3)
- Belczynski, K., Perna, R., Bulik, T., et al. 2006, *ApJ*, 648, 1110, doi: [10.1086/505169](https://doi.org/10.1086/505169)
- Berger, E. 2010, *ApJ*, 722, 1946, doi: [10.1088/0004-637X/722/2/1946](https://doi.org/10.1088/0004-637X/722/2/1946)
- . 2014, *ARA&A*, 52, 43, doi: [10.1146/annurev-astro-081913-035926](https://doi.org/10.1146/annurev-astro-081913-035926)
- Berger, E., Zauderer, B. A., Levan, A., et al. 2013, *ApJ*, 765, 121, doi: [10.1088/0004-637X/765/2/121](https://doi.org/10.1088/0004-637X/765/2/121)
- Berry, C. P. L., Mandel, I., Middleton, H., et al. 2015, *ApJ*, 804, 114, doi: [10.1088/0004-637X/804/2/114](https://doi.org/10.1088/0004-637X/804/2/114)
- Bertin, E., & Arnouts, S. 1996, *A&AS*, 117, 393, doi: [10.1051/aas:1996164](https://doi.org/10.1051/aas:1996164)
- Blanchard, P. K., Berger, E., Fong, W., et al. 2017, *ApJL*, 848, L22, doi: [10.3847/2041-8213/aa9055](https://doi.org/10.3847/2041-8213/aa9055)
- Bloom, J. S., Kulkarni, S. R., & Djorgovski, S. G. 2002, *AJ*, 123, 1111, doi: [10.1086/338893](https://doi.org/10.1086/338893)
- Bloom, J. S., Sigurdsson, S., & Pols, O. R. 1999, *MNRAS*, 305, 763, doi: [10.1046/j.1365-8711.1999.02437.x](https://doi.org/10.1046/j.1365-8711.1999.02437.x)
- Bloom, J. S., Perley, D. A., Chen, H. W., et al. 2007, *ApJ*, 654, 878, doi: [10.1086/509114](https://doi.org/10.1086/509114)
- Brammer, G. B., van Dokkum, P. G., & Coppi, P. 2008, *ApJ*, 686, 1503, doi: [10.1086/591786](https://doi.org/10.1086/591786)
- Bromberg, O., Nakar, E., Piran, T., & Sari, R. 2013, *ApJ*, 764, 179, doi: [10.1088/0004-637X/764/2/179](https://doi.org/10.1088/0004-637X/764/2/179)
- Bruzual, G., & Charlot, S. 2003, *MNRAS*, 344, 1000, doi: [10.1046/j.1365-8711.2003.06897.x](https://doi.org/10.1046/j.1365-8711.2003.06897.x)
- Burrows, D. N., Hill, J. E., Nousek, J. A., et al. 2005, *SSRv*, 120, 165, doi: [10.1007/s11214-005-5097-2](https://doi.org/10.1007/s11214-005-5097-2)
- Calzetti, D., Armus, L., Bohlin, R. C., et al. 2000, *ApJ*, 533, 682, doi: [10.1086/308692](https://doi.org/10.1086/308692)
- Cano, Z., de Ugarte Postigo, A., Malesani, D., & Thoene, C. C. 2016, *GRB Coordinates Network*, 19160, 1
- Cardelli, J. A., Clayton, G. C., & Mathis, J. S. 1989, *ApJ*, 345, 245, doi: [10.1086/167900](https://doi.org/10.1086/167900)
- Cenko, S. B., Kasliwal, M., Harrison, F. A., et al. 2006, *ApJ*, 652, 490, doi: [10.1086/508149](https://doi.org/10.1086/508149)
- Chabrier, G. 2003, *PASP*, 115, 763, doi: [10.1086/376392](https://doi.org/10.1086/376392)
- Chambers, K. C., Magnier, E. A., Metcalfe, N., et al. 2016, *arXiv e-prints*, arXiv:1612.05560, <https://arxiv.org/abs/1612.05560>
- Chornock, R., Berger, E., Kasen, D., et al. 2017, *ApJL*, 848, L19, doi: [10.3847/2041-8213/aa905c](https://doi.org/10.3847/2041-8213/aa905c)
- Chu, Q., Yu, S., & Lu, Y. 2022, *MNRAS*, 509, 1557, doi: [10.1093/mnras/stab2882](https://doi.org/10.1093/mnras/stab2882)
- Conroy, C., Gunn, J. E., & White, M. 2009, *ApJ*, 699, 486, doi: [10.1088/0004-637X/699/1/486](https://doi.org/10.1088/0004-637X/699/1/486)
- Coughlin, M. W., Ahumada, T., Anand, S., et al. 2019, *ApJL*, 885, L19, doi: [10.3847/2041-8213/ab4ad8](https://doi.org/10.3847/2041-8213/ab4ad8)
- Coughlin, M. W., Dietrich, T., Antier, S., et al. 2020, *MNRAS*, 497, 1181, doi: [10.1093/mnras/staa1925](https://doi.org/10.1093/mnras/staa1925)
- Coulter, D. A., Foley, R. J., Kilpatrick, C. D., et al. 2017, *Science*, 358, 1556, doi: [10.1126/science.aap9811](https://doi.org/10.1126/science.aap9811)
- Cowperthwaite, P. S., Berger, E., Villar, V. A., et al. 2017, *ApJL*, 848, L17, doi: [10.3847/2041-8213/aa8fc7](https://doi.org/10.3847/2041-8213/aa8fc7)
- Dálya, G., Galgóczi, G., Dobos, L., et al. 2018, *MNRAS*, 479, 2374, doi: [10.1093/mnras/sty1703](https://doi.org/10.1093/mnras/sty1703)
- Dálya, G., Díaz, R., Bouchet, F. R., et al. 2021, *arXiv e-prints*, arXiv:2110.06184, <https://arxiv.org/abs/2110.06184>

- Damjanov, I., Zahid, H. J., Geller, M. J., Fabricant, D. G., & Hwang, H. S. 2018, *ApJS*, 234, 21, doi: [10.3847/1538-4365/aaa01c](https://doi.org/10.3847/1538-4365/aaa01c)
- D'Avanzo, P., Malesani, D., Covino, S., et al. 2009, *A&A*, 498, 711, doi: [10.1051/0004-6361/200811294](https://doi.org/10.1051/0004-6361/200811294)
- Davé, R. 2008, *MNRAS*, 385, 147, doi: [10.1111/j.1365-2966.2008.12866.x](https://doi.org/10.1111/j.1365-2966.2008.12866.x)
- Dey, A., Schlegel, D. J., Lang, D., et al. 2019, *AJ*, 157, 168, doi: [10.3847/1538-3881/ab089d](https://doi.org/10.3847/1538-3881/ab089d)
- Dichiara, S., Troja, E., O'Connor, B., et al. 2020, *MNRAS*, 492, 5011, doi: [10.1093/mnras/staa124](https://doi.org/10.1093/mnras/staa124)
- Dichiara, S., Troja, E., Beniamini, P., et al. 2021, *ApJL*, 911, L28, doi: [10.3847/2041-8213/abf562](https://doi.org/10.3847/2041-8213/abf562)
- Dye, S., Lawrence, A., Read, M. A., et al. 2018, *MNRAS*, 473, 5113, doi: [10.1093/mnras/stx2622](https://doi.org/10.1093/mnras/stx2622)
- Evans, P. A., Cenko, S. B., Kennea, J. A., et al. 2017, *Science*, 358, 1565, doi: [10.1126/science.aap9580](https://doi.org/10.1126/science.aap9580)
- Faber, J. A., Baumgarte, T. W., Shapiro, S. L., & Taniguchi, K. 2006, *ApJL*, 641, L93, doi: [10.1086/504111](https://doi.org/10.1086/504111)
- Fitzpatrick, E. L. 1999, *PASP*, 111, 63, doi: [10.1086/316293](https://doi.org/10.1086/316293)
- Fong, W., & Berger, E. 2013, *ApJ*, 776, 18, doi: [10.1088/0004-637X/776/1/18](https://doi.org/10.1088/0004-637X/776/1/18)
- Fong, W., Berger, E., & Fox, D. B. 2010, *ApJ*, 708, 9, doi: [10.1088/0004-637X/708/1/9](https://doi.org/10.1088/0004-637X/708/1/9)
- Fong, W., Berger, E., Chornock, R., et al. 2011, *ApJ*, 730, 26, doi: [10.1088/0004-637X/730/1/26](https://doi.org/10.1088/0004-637X/730/1/26)
- . 2013, *ApJ*, 769, 56, doi: [10.1088/0004-637X/769/1/56](https://doi.org/10.1088/0004-637X/769/1/56)
- Fong, W., Margutti, R., Chornock, R., et al. 2016, *ApJ*, 833, 151, doi: [10.3847/1538-4357/833/2/151](https://doi.org/10.3847/1538-4357/833/2/151)
- Fong, W., Berger, E., Blanchard, P. K., et al. 2017, *ApJL*, 848, L23, doi: [10.3847/2041-8213/aa9018](https://doi.org/10.3847/2041-8213/aa9018)
- Fong, W., Laskar, T., Rastinejad, J., et al. 2021, *ApJ*, 906, 127, doi: [10.3847/1538-4357/abc74a](https://doi.org/10.3847/1538-4357/abc74a)
- Fong, W.-f., Nugent, A. E., Dong, Y., et al. 2022, *ApJ*, 940, 56, doi: [10.3847/1538-4357/ac91d0](https://doi.org/10.3847/1538-4357/ac91d0)
- Fox, D. B., Frail, D. A., Price, P. A., et al. 2005, *Nature*, 437, 845, doi: [10.1038/nature04189](https://doi.org/10.1038/nature04189)
- Gal-Yam, A., Fox, D. B., Price, P. A., et al. 2006, *Nature*, 444, 1053, doi: [10.1038/nature05373](https://doi.org/10.1038/nature05373)
- Gao, H., Zhang, B., Lü, H.-J., & Li, Y. 2017, *ApJ*, 837, 50, doi: [10.3847/1538-4357/aa5be3](https://doi.org/10.3847/1538-4357/aa5be3)
- Gorosabel, J., Castro-Tirado, A. J., Guziy, S., et al. 2006, *A&A*, 450, 87, doi: [10.1051/0004-6361:20054373](https://doi.org/10.1051/0004-6361:20054373)
- Gottlieb, O., Metzger, B. D., Quataert, E., Issa, D., & Foucart, F. 2023, arXiv e-prints, arXiv:2309.00038, doi: [10.48550/arXiv.2309.00038](https://doi.org/10.48550/arXiv.2309.00038)
- Graham, J. F., Fruchter, A. S., Levan, A. J., et al. 2009, *ApJ*, 698, 1620, doi: [10.1088/0004-637X/698/2/1620](https://doi.org/10.1088/0004-637X/698/2/1620)
- Guelbenzu, A. M. N., Klose, S., Schady, P., et al. 2021, *The Astrophysical Journal*, 923, 38, doi: [10.3847/1538-4357/ac2faa](https://doi.org/10.3847/1538-4357/ac2faa)
- Hjorth, J., Levan, A. J., Tanvir, N. R., et al. 2017, *ApJL*, 848, L31, doi: [10.3847/2041-8213/aa9110](https://doi.org/10.3847/2041-8213/aa9110)
- Im, M., Yoon, Y., Lee, S.-K. J., et al. 2017, *ApJL*, 849, L16, doi: [10.3847/2041-8213/aa9367](https://doi.org/10.3847/2041-8213/aa9367)
- Jespersen, C. K., Severin, J. B., Steinhardt, C. L., et al. 2020, *ApJL*, 896, L20, doi: [10.3847/2041-8213/ab964d](https://doi.org/10.3847/2041-8213/ab964d)
- Jin, Z.-P., Covino, S., Liao, N.-H., et al. 2020, *Nature Astronomy*, 4, 77, doi: [10.1038/s41550-019-0892-y](https://doi.org/10.1038/s41550-019-0892-y)
- Jin, Z.-P., Li, X., Wang, H., et al. 2018, *ApJ*, 857, 128, doi: [10.3847/1538-4357/aab76d](https://doi.org/10.3847/1538-4357/aab76d)
- Jin, Z.-P., Zhou, H., Covino, S., et al. 2021, arXiv e-prints, arXiv:2109.07694, doi: [10.48550/arXiv.2109.07694](https://doi.org/10.48550/arXiv.2109.07694)
- Kang, Y., Liu, C., Zhu, J.-P., et al. 2023, Prospects for detecting neutron star-white dwarf mergers with decihertz gravitational-wave observatories. <https://arxiv.org/abs/2309.16991>
- Kasen, D., & Barnes, J. 2019, *ApJ*, 876, 128, doi: [10.3847/1538-4357/ab06c2](https://doi.org/10.3847/1538-4357/ab06c2)
- Kasen, D., Metzger, B., Barnes, J., Quataert, E., & Ramirez-Ruiz, E. 2017, *Nature*, 551, 80, doi: [10.1038/nature24453](https://doi.org/10.1038/nature24453)
- Klose, S., Nicuesa Guelbenzu, A. M., Michałowski, M. J., et al. 2019, *ApJ*, 887, 206, doi: [10.3847/1538-4357/ab528a](https://doi.org/10.3847/1538-4357/ab528a)
- Kouveliotou, C., Meegan, C. A., Fishman, G. J., et al. 1993, *ApJL*, 413, L101, doi: [10.1086/186969](https://doi.org/10.1086/186969)
- Kriek, M., van Dokkum, P. G., Labbé, I., et al. 2009, *ApJ*, 700, 221, doi: [10.1088/0004-637X/700/1/221](https://doi.org/10.1088/0004-637X/700/1/221)
- Lawrence, A., Warren, S. J., Almaini, O., et al. 2007, *MNRAS*, 379, 1599, doi: [10.1111/j.1365-2966.2007.12040.x](https://doi.org/10.1111/j.1365-2966.2007.12040.x)
- . 2012, *VizieR Online Data Catalog*, II/314
- Leibler, C. N., & Berger, E. 2010, *ApJ*, 725, 1202, doi: [10.1088/0004-637X/725/1/1202](https://doi.org/10.1088/0004-637X/725/1/1202)
- Levan, A. J., Tanvir, N. R., Jakobsson, P., et al. 2008, *MNRAS*, 384, 541, doi: [10.1111/j.1365-2966.2007.11953.x](https://doi.org/10.1111/j.1365-2966.2007.11953.x)
- Levan, A. J., Lyman, J. D., Tanvir, N. R., et al. 2017, *ApJL*, 848, L28, doi: [10.3847/2041-8213/aa905f](https://doi.org/10.3847/2041-8213/aa905f)
- Liang, Z., Suzuki, N., Doi, M., Tanaka, M., & Yasuda, N. 2024, Luminosity Functions of the Host Galaxies of Supernova. <https://arxiv.org/abs/2401.14603>
- LIGO Scientific Collaboration, Aasi, J., Abbott, B. P., et al. 2015, *Classical and Quantum Gravity*, 32, 074001, doi: [10.1088/0264-9381/32/7/074001](https://doi.org/10.1088/0264-9381/32/7/074001)
- Lilly, S. J., Le Fèvre, O., Renzini, A., et al. 2007, *ApJS*, 172, 70, doi: [10.1086/516589](https://doi.org/10.1086/516589)

- Lilly, S. J., Le Brun, V., Maier, C., et al. 2009, *ApJS*, 184, 218, doi: [10.1088/0067-0049/184/2/218](https://doi.org/10.1088/0067-0049/184/2/218)
- Liu, Z.-Y., Lin, Z.-Y., Yu, J.-M., et al. 2023, *ApJ*, 947, 59, doi: [10.3847/1538-4357/acc73b](https://doi.org/10.3847/1538-4357/acc73b)
- Lü, H.-J., Yuan, H.-Y., Yi, T.-F., et al. 2022, *ApJL*, 931, L23, doi: [10.3847/2041-8213/ac6e3a](https://doi.org/10.3847/2041-8213/ac6e3a)
- Mandhai, S., Lamb, G. P., Tanvir, N. R., et al. 2022, *MNRAS*, 514, 2716, doi: [10.1093/mnras/stac1473](https://doi.org/10.1093/mnras/stac1473)
- Mannucci, F., Cresci, G., Maiolino, R., Marconi, A., & Gnerucci, A. 2010, *MNRAS*, 408, 2115, doi: [10.1111/j.1365-2966.2010.17291.x](https://doi.org/10.1111/j.1365-2966.2010.17291.x)
- Mapelli, M., Giacobbo, N., Santoliquido, F., & Artale, M. C. 2019, *MNRAS*, 487, 2, doi: [10.1093/mnras/stz1150](https://doi.org/10.1093/mnras/stz1150)
- Mapelli, M., Giacobbo, N., Toffano, M., et al. 2018, *MNRAS*, 481, 5324, doi: [10.1093/mnras/sty2663](https://doi.org/10.1093/mnras/sty2663)
- Martin, D. C., Fanson, J., Schiminovich, D., et al. 2005, *ApJL*, 619, L1, doi: [10.1086/426387](https://doi.org/10.1086/426387)
- McCarthy, K. S., Zheng, Z., & Ramirez-Ruiz, E. 2020, *MNRAS*, 499, 5220, doi: [10.1093/mnras/staa3206](https://doi.org/10.1093/mnras/staa3206)
- Meegan, C., Lichti, G., Bhat, P. N., et al. 2009, *ApJ*, 702, 791, doi: [10.1088/0004-637X/702/1/791](https://doi.org/10.1088/0004-637X/702/1/791)
- Narayan, R., Paczynski, B., & Piran, T. 1992, *ApJL*, 395, L83, doi: [10.1086/186493](https://doi.org/10.1086/186493)
- Norris, J. P., & Bonnell, J. T. 2006, *ApJ*, 643, 266, doi: [10.1086/502796](https://doi.org/10.1086/502796)
- Nugent, A. E., fai Fong, W., Castrejon, C., et al. 2023, A Population of Short-duration Gamma-ray Bursts with Dwarf Host Galaxies. <https://arxiv.org/abs/2310.12202>
- Nugent, A. E., Fong, W., Dong, Y., et al. 2020, *ApJ*, 904, 52, doi: [10.3847/1538-4357/abc24a](https://doi.org/10.3847/1538-4357/abc24a)
- Nugent, A. E., Fong, W.-F., Dong, Y., et al. 2022, *ApJ*, 940, 57, doi: [10.3847/1538-4357/ac91d1](https://doi.org/10.3847/1538-4357/ac91d1)
- O'Connor, B., Troja, E., Dichiara, S., et al. 2021, *MNRAS*, 502, 1279, doi: [10.1093/mnras/stab132](https://doi.org/10.1093/mnras/stab132)
- . 2022a, *MNRAS*, 515, 4890, doi: [10.1093/mnras/stac1982](https://doi.org/10.1093/mnras/stac1982)
- O'Connor, B., Andreoni, I., Cenko, S. B., et al. 2022b, GRB Coordinates Network, 32957, 1
- Ofek, E. O., Cenko, S. B., Gal-Yam, A., et al. 2007, *ApJ*, 662, 1129, doi: [10.1086/518082](https://doi.org/10.1086/518082)
- Paek, G. S. H., Im, M., Kim, J., et al. 2024, *ApJ*, 960, 113, doi: [10.3847/1538-4357/ad0238](https://doi.org/10.3847/1538-4357/ad0238)
- Palmese, A., Bom, C. R., Mucesh, S., & Hartley, W. G. 2021, arXiv e-prints, arXiv:2111.06445. <https://arxiv.org/abs/2111.06445>
- Pan, Y. C., Kilpatrick, C. D., Simon, J. D., et al. 2017, *ApJL*, 848, L30, doi: [10.3847/2041-8213/aa9116](https://doi.org/10.3847/2041-8213/aa9116)
- Paterson, K., Fong, W., Nugent, A., et al. 2020, *ApJL*, 898, L32, doi: [10.3847/2041-8213/aba4b0](https://doi.org/10.3847/2041-8213/aba4b0)
- Perley, D. A., Modjaz, M., Morgan, A. N., et al. 2012, *ApJ*, 758, 122, doi: [10.1088/0004-637X/758/2/122](https://doi.org/10.1088/0004-637X/758/2/122)
- Pian, E., D'Avanzo, P., Benetti, S., et al. 2017, *Nature*, 551, 67, doi: [10.1038/nature24298](https://doi.org/10.1038/nature24298)
- Prochaska, J. X., Bloom, J. S., Chen, H. W., et al. 2006, *ApJ*, 642, 989, doi: [10.1086/501160](https://doi.org/10.1086/501160)
- Rastinejad, J. C., Gompertz, B. P., Levan, A. J., et al. 2022, *Nature*, 612, 223, doi: [10.1038/s41586-022-05390-w](https://doi.org/10.1038/s41586-022-05390-w)
- Rinaldi, S., & Del Pozzo, W. 2022, *MNRAS*, 517, L5, doi: [10.1093/mnrasl/slac101](https://doi.org/10.1093/mnrasl/slac101)
- Rodrigo, C., & Solano, E. 2020, in XIV.0 Scientific Meeting (virtual) of the Spanish Astronomical Society, 182
- Roming, P. W. A., Kennedy, T. E., Mason, K. O., et al. 2005, *SSRv*, 120, 95, doi: [10.1007/s11214-005-5095-4](https://doi.org/10.1007/s11214-005-5095-4)
- Rossi, A., Stratta, G., Maiorano, E., et al. 2020, *MNRAS*, 493, 3379, doi: [10.1093/mnras/staa479](https://doi.org/10.1093/mnras/staa479)
- Rossi, A., Rothberg, B., Palazzi, E., et al. 2022, *ApJ*, 932, 1, doi: [10.3847/1538-4357/ac60a2](https://doi.org/10.3847/1538-4357/ac60a2)
- Rosswog, S., Ramirez-Ruiz, E., & Davies, M. B. 2003, *MNRAS*, 345, 1077, doi: [10.1046/j.1365-2966.2003.07032.x](https://doi.org/10.1046/j.1365-2966.2003.07032.x)
- Rouco Escorial, A., Fong, W., Veres, P., et al. 2021, *The Astrophysical Journal*, 912, 95, doi: [10.3847/1538-4357/abee85](https://doi.org/10.3847/1538-4357/abee85)
- Rouco Escorial, A., Fong, W., Berger, E., et al. 2023, *ApJ*, 959, 13, doi: [10.3847/1538-4357/acf830](https://doi.org/10.3847/1538-4357/acf830)
- Ruffert, M., & Janka, H. T. 1999, *A&A*, 344, 573, doi: [10.48550/arXiv.astro-ph/9809280](https://doi.org/10.48550/arXiv.astro-ph/9809280)
- Savaglio, S., Glazebrook, K., & Le Borgne, D. 2009, *ApJ*, 691, 182, doi: [10.1088/0004-637X/691/1/182](https://doi.org/10.1088/0004-637X/691/1/182)
- Schlafly, E. F., & Finkbeiner, D. P. 2011, *ApJ*, 737, 103, doi: [10.1088/0004-637X/737/2/103](https://doi.org/10.1088/0004-637X/737/2/103)
- Schlegel, D. J., Finkbeiner, D. P., & Davis, M. 1998, *ApJ*, 500, 525, doi: [10.1086/305772](https://doi.org/10.1086/305772)
- Selsing, J., Krühler, T., Malesani, D., et al. 2018, *A&A*, 616, A48, doi: [10.1051/0004-6361/201731475](https://doi.org/10.1051/0004-6361/201731475)
- Shibata, M., & Taniguchi, K. 2011, *Living Reviews in Relativity*, 14, 6, doi: [10.12942/lrr-2011-6](https://doi.org/10.12942/lrr-2011-6)
- Singer, L. P., Parazin, B., Coughlin, M. W., et al. 2022, *AJ*, 163, 209, doi: [10.3847/1538-3881/ac5ab8](https://doi.org/10.3847/1538-3881/ac5ab8)
- Singer, L. P., Price, L. R., Farr, B., et al. 2014, *ApJ*, 795, 105, doi: [10.1088/0004-637X/795/2/105](https://doi.org/10.1088/0004-637X/795/2/105)
- Singer, L. P., Chen, H.-Y., Holz, D. E., et al. 2016, *ApJL*, 829, L15, doi: [10.3847/2041-8205/829/1/L15](https://doi.org/10.3847/2041-8205/829/1/L15)
- Smartt, S. J., Chen, T. W., Jerkstrand, A., et al. 2017, *Nature*, 551, 75, doi: [10.1038/nature24303](https://doi.org/10.1038/nature24303)
- Song, J.-Y., Wang, L.-F., Li, Y., et al. 2022, arXiv e-prints, arXiv:2212.00531, doi: [10.48550/arXiv.2212.00531](https://doi.org/10.48550/arXiv.2212.00531)
- Tanvir, N. R., Levan, A. J., Fruchter, A. S., et al. 2013, *Nature*, 500, 547, doi: [10.1038/nature12505](https://doi.org/10.1038/nature12505)
- Tanvir, N. R., Vergani, S., Hjorth, J., et al. 2010, GRB Coordinates Network, 11123, 1

- Tanvir, N. R., Levan, A. J., González-Fernández, C., et al. 2017, *ApJL*, 848, L27, doi: [10.3847/2041-8213/aa90b6](https://doi.org/10.3847/2041-8213/aa90b6)
- Tonry, J. L., Stubbs, C. W., Lykke, K. R., et al. 2012, *ApJ*, 750, 99, doi: [10.1088/0004-637X/750/2/99](https://doi.org/10.1088/0004-637X/750/2/99)
- Troja, E., Sakamoto, T., Cenko, S. B., et al. 2016, *ApJ*, 827, 102, doi: [10.3847/0004-637X/827/2/102](https://doi.org/10.3847/0004-637X/827/2/102)
- Troja, E., Piro, L., van Eerten, H., et al. 2017, *Nature*, 551, 71, doi: [10.1038/nature24290](https://doi.org/10.1038/nature24290)
- Troja, E., Ryan, G., Piro, L., et al. 2018, *Nature Communications*, 9, 4089, doi: [10.1038/s41467-018-06558-7](https://doi.org/10.1038/s41467-018-06558-7)
- Troja, E., Castro-Tirado, A. J., Becerra González, J., et al. 2019, *MNRAS*, 489, 2104, doi: [10.1093/mnras/stz2255](https://doi.org/10.1093/mnras/stz2255)
- Troja, E., Fryer, C. L., O'Connor, B., et al. 2022, *Nature*, 612, 228, doi: [10.1038/s41586-022-05327-3](https://doi.org/10.1038/s41586-022-05327-3)
- Tunnicliffe, R. L., Levan, A. J., Tanvir, N. R., et al. 2014, *MNRAS*, 437, 1495, doi: [10.1093/mnras/stt1975](https://doi.org/10.1093/mnras/stt1975)
- Weaver, J. R., Kauffmann, O. B., Ilbert, O., et al. 2022, *ApJS*, 258, 11, doi: [10.3847/1538-4365/ac3078](https://doi.org/10.3847/1538-4365/ac3078)
- Weaver, J. R., Davidzon, I., Toft, S., et al. 2023, *A&A*, 677, A184, doi: [10.1051/0004-6361/202245581](https://doi.org/10.1051/0004-6361/202245581)
- Worthey, G. 1994, *ApJS*, 95, 107, doi: [10.1086/192096](https://doi.org/10.1086/192096)
- Wright, E. L., Eisenhardt, P. R. M., Mainzer, A. K., et al. 2010, *AJ*, 140, 1868, doi: [10.1088/0004-6256/140/6/1868](https://doi.org/10.1088/0004-6256/140/6/1868)
- Yang, B., Jin, Z.-P., Li, X., et al. 2015, *Nature Communications*, 6, 7323, doi: [10.1038/ncomms8323](https://doi.org/10.1038/ncomms8323)
- Yang, J., Ai, S., Zhang, B.-B., et al. 2022, *Nature*, 612, 232, doi: [10.1038/s41586-022-05403-8](https://doi.org/10.1038/s41586-022-05403-8)
- Yang, Y.-H., Troja, E., O'Connor, B., et al. 2024, *Nature*, 626, 742, doi: [10.1038/s41586-023-06979-5](https://doi.org/10.1038/s41586-023-06979-5)
- Zevin, M., Nugent, A. E., Adhikari, S., et al. 2022, *ApJL*, 940, L18, doi: [10.3847/2041-8213/ac91cd](https://doi.org/10.3847/2041-8213/ac91cd)
- Zhong, S.-Q., Li, L., & Dai, Z.-G. 2023, *ApJL*, 947, L21, doi: [10.3847/2041-8213/acca83](https://doi.org/10.3847/2041-8213/acca83)
- Zhu, J.-P., Wang, X. I., Sun, H., et al. 2022, *ApJL*, 936, L10, doi: [10.3847/2041-8213/ac85ad](https://doi.org/10.3847/2041-8213/ac85ad)